An Analysis of Altitude Compensation Systems using Method of Characteristics with CFD Implementations

a project presented to
The Faculty of the Department of Aerospace Engineering
San José State University

in partial fulfillment of the requirements for the degree
Master of Science in Aerospace Engineering

by

Kovin "Kevin" Aghassi Lelham

December 2023

approved by
Dr. Perikilis Papadopoulos
Faculty Advisor

ABSTRACT

An Analysis of Altitude Compensation Systems using Method of Characteristics with CFD Implementations

Kevin Aghassi Lelham

The performance of a rocket nozzle is paramount for space flight missions. The performance, indicated by a few parameters, largely depends on the general geometry of the converging-diverging sections. A rocket engine performs the best when the exit pressure of the propellant matches the ambient pressure of the atmosphere at that altitude, maximizing thrust. Categorized as an adapted nozzle, this project investigates the effect of changing the nozzle geometry to achieve this state throughout the entire ascent and finds a significant increase in performance as expected. As part of the investigation, this report leveraged computational fluid dynamics (CFD) and the method of characteristics to develop and test the rocket nozzle geometry. After developing a method of characteristics algorithm, this report generated nozzle contours for several known engines and recreated their conditions to compare with theoretical calculations. Seeing that CFD simulations produced forces lower than expected, a parametric study on the generated geometry was ran by expanding and contracting the vertical points of the contour. The report concludes with an empirically driven correction factor of 1.025 for the geometry produced by the method of characteristics. This correction factor serves to account for omissions of physical phenomena in the governing equations used to derive the method of characteristics and thus bridge the gap between theory to reality.

ACKNOWLEDGEMENTS

I would like to express my deepest gratitude to the many individuals who have been the source of my motivation to succeed and pursue my education. First and foremost, I thank my mother, Jacqueline, and father, Eshkhan, along with my grandparents for the sacrifices they made in their lives so that I could live mine. Every ounce of my motivation stems from their perseverance and I will always dedicate my achievements directly to them. I appreciate all the guidance provided by the faculty of San José State University, particularly Dr. Papadopoulos for his encouragement and advising in my project. Lastly, I thank my partner Paige M. Peterson for her never-ending encouragement, kindness, and understanding, especially during my studies.

TABLE OF CONTENTS

LIST OF FIGURES

LIST OF TABLES

NOMENCLATURE

Symbol	**Definition**	**Units**
F_T	Force, thrust	N
$\dot{m}$	Mass Flow Rate	kg/s
p	Pressure	Pa
A	Area	m^2
v	Velocity	m/s
R_A	Gas Constant	m^3Pa/K/mol
M_W	Molecular Weight	g/mol
M_F	Molecular Weight of Propellant Fuel	g/mol
M_O	Molecular Weight of Propellant Oxidizer	g/mol
T	Temperature	K
C_F	Coefficient of Thrust	---
I_{sp}	Specific Impulse	s
g_0	Earth's Gravitational Acceleration, 9.81	m/s^2
M	Mach Number	---
K	Method of characteristics constants	rad
r	Propellant Oxidizer to Fuel Ratio	---
Greek Symbols		
θ	Flow Angle	rad
ν	Prandtl-Meyer Angle	rad
μ	Mach Angle	rad
γ	Specific Heat Ratio	---
ρ	Density	kg/m^3
Subscripts		
e	At Nozzle Exit	---
a	Ambient	---
c	At Chamber	---
Superscripts		
*	At Throat	---
Abbreviations		
CFD	Computational Fluid Dynamics	---
LOX	Liquid Oxygen	---
LH2	Liquid Hydrogen	---

Chapter 1 Introduction

1.1 Motivation

In the field of rocket propulsion, performance is key. The indicators typically used to model the performance of a rocket are thrust, specific impulse, and coefficient of thrust. Maximizing these values to optimize the performance of the rocket requires removing any losses in the overall system so that the rocket may generate the greatest amount of thrust and obtain the highest specific impulse.

To maximize these values, one must examine the variables in the calculations. This project aims to address one component in the thrust equation: the difference in ambient pressure and nozzle exit pressure. When the ambient pressure is higher than the exit pressure, the thrust achieved decreases due to the opposing higher pressure at the outside of the nozzle. This occurrence is referred to as overexpanded. If the opposite is true, then it is called underexpanded and isentropic relations show the potential for a higher nozzle exit to throat area ratio, which would ultimately lead to a higher exit velocity and thus higher thrust. The ideal scenario, then, is in the instance when the exit pressure equals the ambient pressure, referred to as ideally expanded or an adapted nozzle. This case ensures that the fuel used produces the highest amount of thrust possible and there is no potential for higher thrust which is not being generated.

Systems which aim to achieve this ideal state are called altitude compensation systems. Because of its dependence on the nozzle geometry, the exit pressure can be controlled by the general contour of nozzle's diverging section. With the many existing tools to develop the nozzle contour, the method of characteristics offers a great starting point as it solves the governing equations to generate a contour suited for the problem parameters. This paper will analyze the theoretical effects of implementing an altitude compensation system and proceed to the application using the method of characteristics.

1.2 Literature Review

1.2.1 General Equations

This study, as its nature focuses on the optimization of thrust and rocket performance, will utilize the governing equations of rocket propulsion. This will ultimately entail the rocket equations for thrust, exit velocity, area and pressure ratios, coefficient of thrust, and specific impulse shown by Mattingly with isentropic relations shown by Anderson for convenience [1][2].

$$F_T = \dot{m}v_e + (p_e - p_a)A_e \tag{1.1.1}$$

$$v_e = \sqrt{\frac{2\gamma}{\gamma-1}\frac{R_A}{M_W T_C}\left[1 - \left(\frac{p_e}{p_c}\right)^{\frac{\gamma-1}{2}}\right]} \tag{1.1.2}$$

$$\frac{A_e}{A^*} = \frac{\Gamma(\gamma)}{\sqrt{\frac{2\gamma}{\gamma-1}\left(\frac{p_e}{p_c}\right)^{\frac{2}{\gamma}}\left[1-\left(\frac{p_e}{p_c}\right)^{\frac{\gamma-1}{2}}\right]}} \tag{1.1.3}$$

$$\Gamma(\gamma) = \sqrt{\gamma(\frac{1+\gamma}{2})^{\frac{1+\gamma}{1-\gamma}}} \quad (1.1.4)$$

$$C_F = \frac{F_T}{p_c A^*} \quad (1.1.5)$$

$$I_{sp} = \frac{F_T}{g_0 \dot{m}} \quad (1.1.6)$$

$$\frac{A_e}{A^*} = (\frac{\gamma+1}{2})^{-\frac{\gamma+1}{2(\gamma-1}} \frac{(1+\frac{\gamma-1}{2}M^2)^{\frac{\gamma+1}{2(\gamma-1)}}}{M} \quad (1.1.7)$$

$$\frac{p}{p_t} = (1 + \frac{\gamma-1}{2}M^2)^{\frac{-\gamma}{\gamma-1}} \quad (1.1.8)$$

Seen in the thrust equation (1.1), the maximum will occur when the exit pressure p_e equals the ambient pressure p_a. The ambient pressure is typically greater than the exit pressure, causing an opposing force for the exiting propellant and thus decreasing the overall generated thrust. In instances when the ambient pressure is less, one may assume that the overall thrust would increase, but the gas expansion occurs outside of the nozzle, causing a loss in thrust as the gas will not exert any force on the nozzle wall [3].

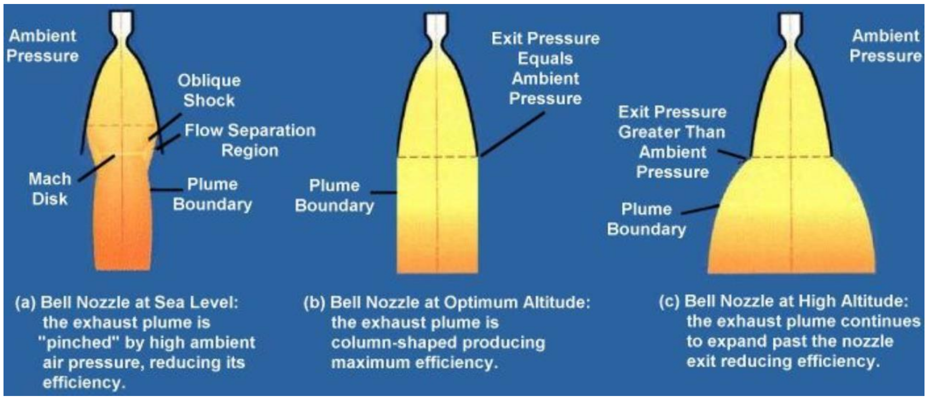

Figure 1.1 – Rocket propellant exit conditions [3].

The specific coefficient of thrust C_F (1.5) and specific impulse I_{sp} (1.6), being functions of thrust, subsequently maximize simultaneously when thrust is maximized. Thus, the attention goes to maximizing thrust, which requires removing any systemic losses.

1.2.2 Studies on Variable Area Nozzles Benefits

There have been numerous studies for altitude compensation systems, where the general characteristics of a jet nozzle will vary to compensate for the changing ambient pressure. Most rockets do not utilize such systems as the integration of this hardware often leads to overwhelming complexity for the nozzle and weight for the system. This complexity may outweigh the benefits in some instances, but when selected appropriately, altitude compensation systems offer significant advantages. These types of systems tend to provide the highest value for rocket powered vehicles experiencing large changes in ambient pressures or in instances of high thrust requirements upon lift off but high efficiency during cruise[4].

In recent years, the demand for altitude compensation systems has increased as the complexity in propulsion systems calls for high efficiency and performance. There are many types of systems which attempt to address the exit to ambient pressure difference, each with its own advantages and disadvantages[5]. Some commons ones discussed in this paper include:

- Dual bell nozzles
- Expansion-deflection nozzles
- Aerospike engines

These applications are wide and not solely for rocket propulsion. Ulf Michel showed the many benefits for general turbofans in “The benefits of variable area fan nozzles on turbofan engines” by analyzing the analytical relations for generated thrust and pressure ratios for the turbofan engine [6]. The study focused on the implementation of a variable area nozzle and the influence on the fan performance which had no frictional losses and ideal fan efficiency. Some of the findings of the report showed:

- Considerably higher propulsive efficiencies at smaller flight Mach numbers
- Shorter climb times to cruise altitude
- A decrease in fuel consumption during climb and
- An increase in fan and propulsive efficiencies during cruise and descent

As a comprehensive study, “Rocket nozzles: 75 years of research and development” establishes a good baseline to compare different types of rocket nozzles with altitude compensation [7]. The study compares conventional nozzles to expansion-deflection nozzles, dual bell, and aerospike nozzles. The study compounds multiple datasets from previous experiments and papers which reported both analytical and experimental values. In each case, the paper showed the higher thrust performance coefficients and specific impulses for the altitude compensation systems than the conventionally static nozzles. The paper concludes by advising of each system’s trade-offs at the expense of their strengths, but also that the dual bell offers considerable advantages due to its simplicity and overall performance.

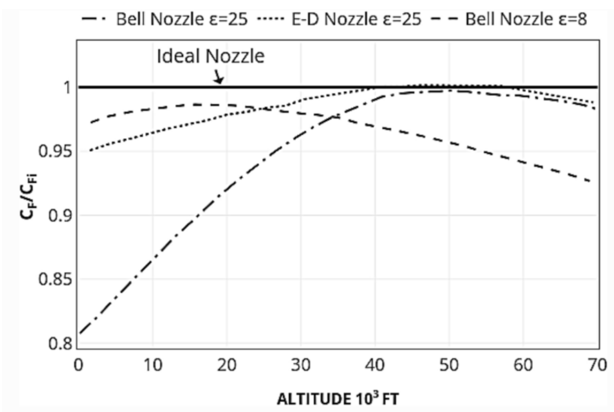

Figure 1.2 – Thrust coefficient ratio comparison between conventional bell nozzles and E-D nozzles [7].

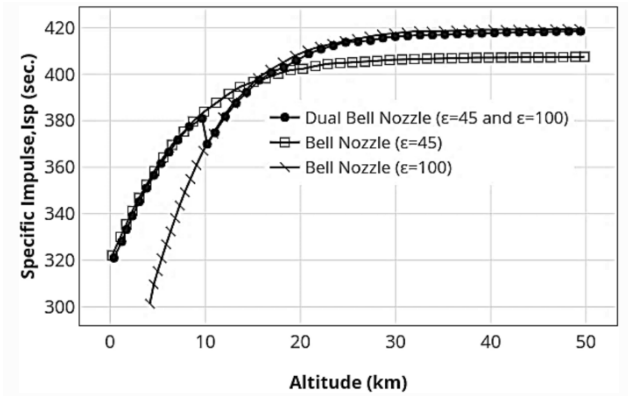

Figure 1.3 – Specific impulse comparison between conventional bell nozzles and dual bell nozzles [7].

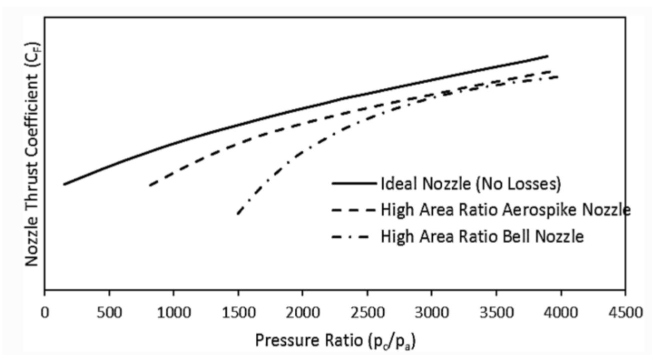

Figure 1.4 – Thrust coefficient comparison between conventional bell, aerospike, and ideal nozzles [7].

Rockwell International's Rocketdyne Division affirms the strengths of dual bell nozzles, which reported a 12.1% increase in payload to low earth orbit because of the use of a dual bell nozzle [8]. In the same study, it showed that a dual bell nozzle can achieve higher nozzle thrust coefficients than fixed nozzles over time for a typical mission. In some cases, the dual bell nozzle may achieve lower thrust coefficients at the start of the mission but gains higher performance as the altitude increases. Similar findings are shown in "Dual-Bell Nozzle Design" which posted results from DFG Collaborative Research Center TRR40, showing the increase in dual bell performance with the increase in altitude after an initial drop [9]. The initial sacrificed of performance is significantly outweighed in the long run as the dual-bell nozzle design allows for higher performance for a larger range.

Similar comparisons can be made for aerospike nozzles, which "Aerospike nozzle contour design and its performance validation" does, reporting higher efficiencies for aerospike nozzles at low pressure ratios due its altitude compensation system [10]. The study reviews previous numerical simulations comparing aerospike and bell nozzles, then conducts hot-firing tests at two ambient pressure conditions. The experiment validated the numerical simulations and reported nozzle efficiencies of 92-93.5% at one pressure ratio and 95-96% at another, where nozzle efficiency is defined the ratio of experimental thrust coefficients to ideal thrust coefficients.

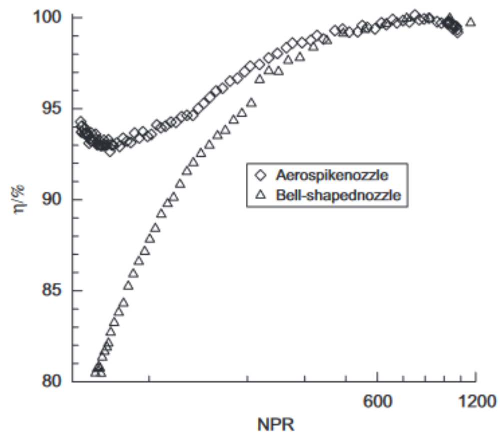

Figure 1.5 – Numerical comparisons of aerospike and conventional bell-shaped nozzles [10].

In terms of physical application of these systems, Johan Steelant compares expansion-deflection and dual bell altitude compensation systems using nozzle efficiency in cold flow testing [11]. Steelant's empirical data shows initially high dual bell nozzle efficiencies which drop with an increase in pressure ratios before rising back up. The study does not compare the compensation systems to conventional nozzles, but it highlights the differences in the two compensation methodologies and how they are better suited to different operating conditions.

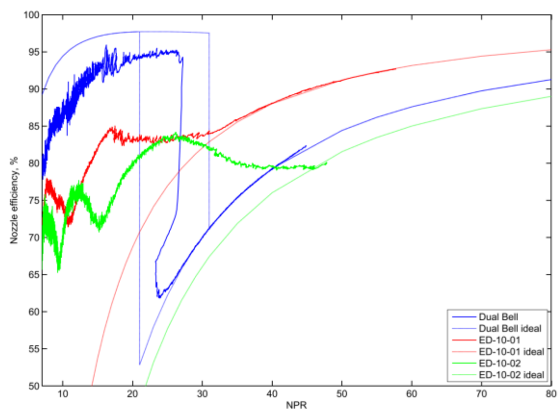

Figure 1.6 – Acquired data for altitude compensation systems [11].

Another cold flow study attempted to show the advantages of integrating dual bell and expansion-deflection nozzles together producing an expansion-deflection dual bell nozzle [12]. The study compared numerical and experimental results of various hybrid nozzles with regular dual bell nozzles, showing that the hybrid model has potential to produce slightly higher specific impulses over a range of nozzle pressure ratios.

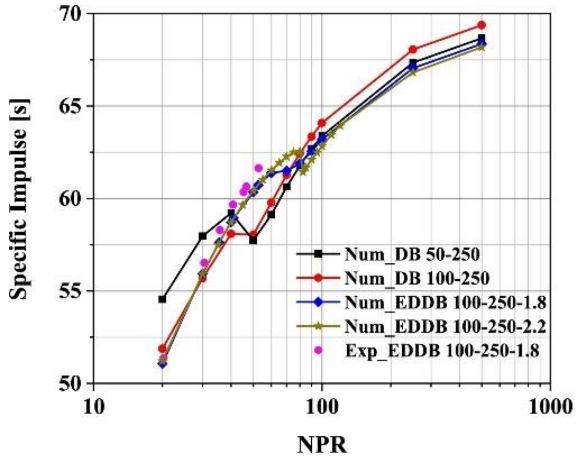

Figure 1.7 – Comparison of altitude compensation systems [12].

1.2.2 Modern Case Studies Variable Area Nozzles

Recent developments of altitude compensation systems showcase the increase in both the demand and feasibility of application. One novel method to implement altitude compensation includes a ringed nozzle arrangement, consisting of a stack of parallel rings which allows for a change in exit area [13]. The study reports CFD results showcasing slightly higher thrust coefficients than a conventional nozzle under similar conditions at low pressure ratios due to its adaptation capability. Although the reported specific impulses between the two nozzles are very similar, the design nonetheless emphasizes the increasing popularity in altitude compensation systems.

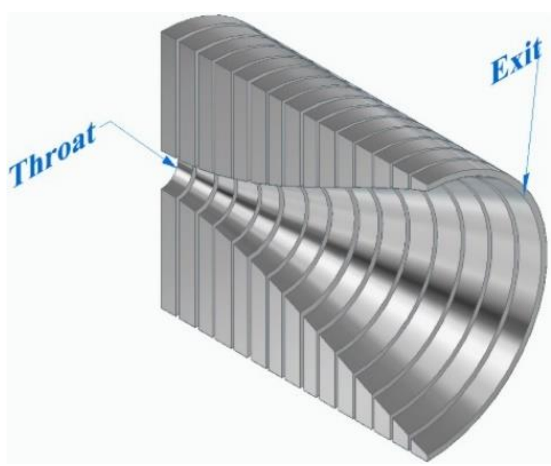

Figure 1.8 – Novel ringed nozzle arrangement concept [13].

Even a capstone project with a budget of $750 at the University of Nevada, Las Vegas showed the feasibility of designing such systems [14]. Although the student reported a few errors throughout the experiment, they still reported being able to design, manufacture, and test a novel concept for a varying nozzle throat area to control the generated thrust at different conditions.

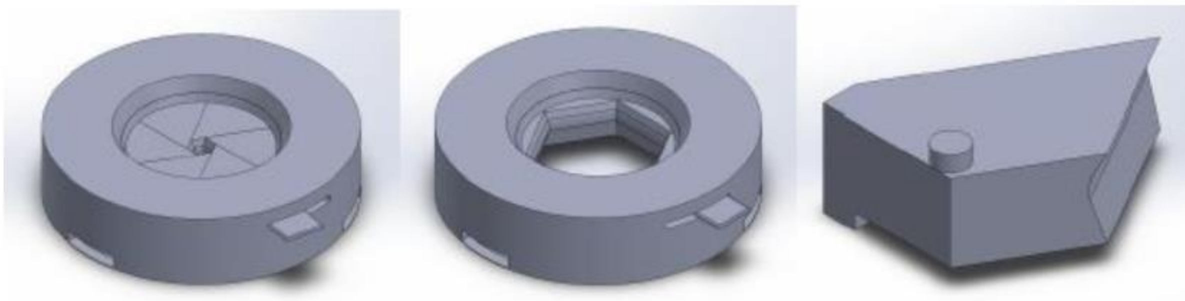

Figure 1.9 – Novel variable nozzle throat area concept [14].

These few novel concepts and the previously shown studies that highlight the benefits of altitude compensation systems signify the increase in their popularity and demand as well as their feasibility in application.

1.2.3 Rocket Nozzle Designs with CFD Applications

Many studies have designed altitude compensation nozzles with evaluations on the results using computational fluid dynamics software like Ansys Fluent. “Designing and Performance Optimization of Dual Bell Nozzle” attempts to integrate an additional bell nozzle for an existing bell contour to increase the exit area for optimal performance [15]. The study utilized analytical models and computational fluid dynamics software (CFD) to optimize the design geometry. The purpose of the iterative modeling was to establish a smooth transition between the two nozzles to achieve high performance without any losses. Starting with geometric design, the paper discusses the general approach and set up in Ansys Fluent and produces results for propellant Mach number throughout the nozzle. Although the paper fails to discuss the specific influence on performance, it does serve as a good example for nozzle design and application to CFD software. Similarly, a less comprehensive CFD example of a basic non-ideal nozzle in “Flow Analysis of Rocket Nozzle Using Computational Fluid Dynamics (Cfd)”is a good reference for comparison of results and general problem setup [16]. Closer to the scope of this project, which aims to address performance optimization, Venkatraman Nagarajan’s master’s thesis sets a detailed example of a CFD model for altitude compensation systems [17]. The paper’s focus is ideal bleed mass flow rate for an aerospike nozzle, with a detailed breakdown of the problem setup in Ansys Fluent providing insight on CFD modeling to this project.

These types of designs typically require some sort of scheme or foundation to base the geometry on. Rao’s method is often a general approach. Outlined in “Handbook of Astronautical Engineering” by G.V.R. Rao in the chapter “Nozzle Contours” alongside his “Recent Developments in Rocket Nozzle Configurations”, Rao discusses how to approach various nozzle geometry design requirements [18][19]. These designs often entail parabolic contours for bell shaped nozzles, with details on the geometric construction of inflection points and angling. Not to be confused with altitude compensation systems, Rao focuses primarily on contour optimization for fixed geometry designs. Most contour optimization techniques utilize approximation concepts from calculus and linear algebra to solve the governing equations. The most common of these is the method of characteristics, which assumes irrotational flow to predict flowfield properties downstream with applications to nozzle design.

Rao's methodology and several other ones are often cited in geometry optimization studies, primarily based on the method of characteristics. "Rocket Engine Nozzle Engine Optimization" starts with Rao's preferred throat geometry before applying Taguchi's method to design different nozzle shapes [20]. The study then goes to evaluate the performance of conical, parabolic, and optimized shapes by comparing fluid velocity throughout the nozzle, reporting that the optimized geometry produces significantly higher velocities at the exit. As a comparison, "Modeling & Simulation of Rocket Nozzle" discusses the nozzle design with greater detail using the method of characteristics and the stream function to develop the geometry before CFD application [21]. This study does expansively discuss the impacts on performance but does serve as a good reference for general rocket nozzle design. The most clear-cut example of an application of the method of characteristics for nozzle design is showcased in Anderson's classic *Modern Compressible Flow*, where he not only derived the formulation but also gave an application of the method with results for the geometry and flow characteristics [2].

In reference to altitude compensation systems and not just contour optimization, a study applied Rao's optimization methodology twice to develop a dual bell nozzle [22]. The study created geometry using SOLIDWORKS and ran CFD simulations in Ansys Fluent to achieve an increase of 5.46% thrust at sea level and 10.5% at vacuum.

These examples will be good references when modeling optimal and ideal nozzle conditions in computational fluid dynamics software. With each studies' scope and goal varying significantly, they provide good insight on the wide range of applications in rocket nozzle contour optimization and integration with altitude compensation systems.

1.2.4 Application to Saturn V

This paper's aim to evaluate the effect of altitude compensation systems will require some nozzle geometry to apply the equations and derive ideal settings for. The nozzle used in the Saturn V missions will serve as a point of analysis for calculations and modeling. NASA archives detail the specifications of the F-1 and J-2 engines, providing the nozzle throat and exit diameters as well as the chamber settings in the original missions [23][24].

Moreover, this paper will also require the ascent data during a Saturn V mission climb to reference the altitude of the rocket as a function of time. The typical altitude during boost, published in the Saturn V flight manual, will be compared to Earth's ambient pressure as a function of altitude [25][26][27]. These pressures will be used in previously shown equations to characterize a single engine's performance as a function of time during Saturn V's ascent.

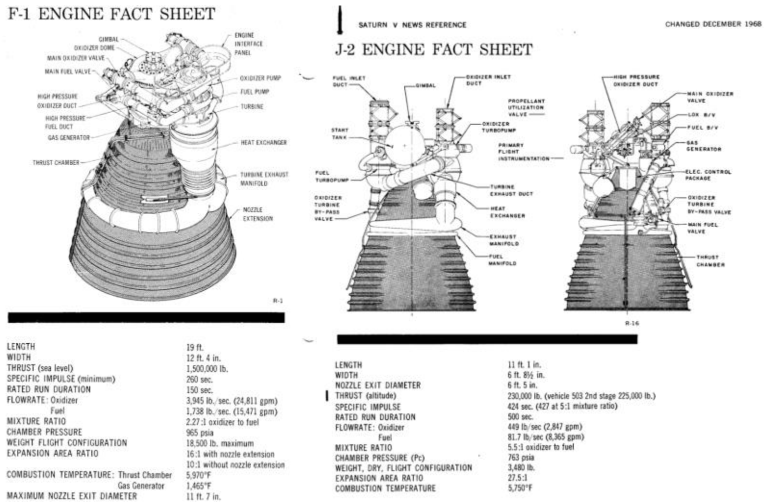

Figure 1.10 – F-1 and J-2 engines fact sheet [23][24].

1.3 Project Objective

Ideally adapted nozzles occur only at a single ambient pressure for static geometry nozzles, but ambient pressure changes with altitude. Due to the decreasing ambient pressure with increasing altitude, this means that the nozzle does not meet its full potential to generate the maximum thrust possible.

Examining the meaning of these variables shows that, of course, the ambient pressure cannot be controlled, but there is flexibility with the exit pressure. The exit pressure is a function of the exit area. This paper aims to examine the effects of altitude compensation on thrust and specific impulse to determine the value a constantly ideally expanded rocket nozzle provides. By assuming optimal exit area and exit pressure, this paper will first show the any potential gains in thrust and specific impulse to compare with the non-ideal conditions under a case study focusing on the Saturn V. The effects of ideal expansion will be considered for both the rocket's F-1 and J-2 rocket engines in this demonstration.

For implementation of an altitude compensation system, this paper will demonstrate the method of characteristics given the Saturn V F-1 engine characteristics. The paper will develop and utilize this differential equations-based methodology to generate nozzle contours given the Mach number from the ideal exit area. This application of the method of characteristics will ultimately lead to an analysis of the method itself. Given that the governing equations for this method assume inviscid flow, a relationship may be formed between theoretical and experimental results by conducting a CFD analysis on the produced contour with viscous flow.

This report will present the governing equations of rocket propulsion which show the relation between exit area and exit pressure and what role these values play in calculating thrust and specific impulse. The mathematical models will be implemented in MATALAB to develop comparisons in results for Saturn V's where the exit pressure does not vary and those where exit pressure remains constant.

1.4 Methodology

The paper will first begin with an overview of the Saturn V F-1 and J-2 engine nozzles and Apollo 10 ascent profile. The initial analysis of the system will cover only the existing architecture, which does not include any altitude compensation systems. To achieve this, this paper will apply the existing nozzles' characteristics and geometry in the governing equations to first calculate the thrust, specific impulse, and exit velocity as a function of time for the ascent profile. This will produce the non-ideal rocket performance characteristics. These calculations, and all subsequent calculations, will be performed using MATLAB computational software.

Moving over to obtaining ideal condition performance, the study will then use typical Saturn V ascent data which documents altitude over time to compare with ambient pressure as a function of altitude. Knowing that the exit pressure should equal ambient pressure in ideal conditions, it can be applied in the same governing equations to obtain the ideal performance of the F-1 and J-2 nozzles.

The study will compare these datasets to determine the benefit of a perfect altitude compensation system. As a means of determining the impact this system may have, the study will compare generated thrust, specific impulse, and exit velocity as functions of time for the ascent of the Saturn V.

As a means of attempting to implement such a system, this paper will then focus on the design of an altitude compensation system to achieve higher thrust, specific impulse, and nozzle exit velocity. The design will entail methods discussed in the literature review, namely the method of characteristics. Starting from the algorithm's theory to its application, this paper will generate the nozzle contour for the F-1 engine which would achieve the ideal Mach number at various points in the ascent profile. Using Ansys Fluent, this paper will then use this geometry to observe differences from generated thrust at the exit in simulated models compared analytical calculations in MATLAB.

The method of characteristics assumes inviscid flow, but real-world conditions entail viscous effects, so this comparison will ultimately lead to an analysis for the method of characteristics itself. The means to run this study will involve a parametric study in computational fluid dynamics (CFD) software like Ansys for multiple rocket engines with differing chamber and nozzle conditions. The parametric study will expand and contract the generated geometry for a given rocket nozzle and calculate the generated thrust as experimental data points. These data points may be compared to the analytical findings to uncover a relationship for the method of characteristics which accounts for viscous effects.

For the modifications in the parametric study, this paper will expand and contract the y-coordinates by constant coefficients and then run the simulation conditions as that rocket's original case. From the produced thrusts in the overall parametric study, this paper will aim to determine whether there is a relationship to account for viscous effects and what it may look like. This relationship will ultimately serve as a correction coefficient to the method of characteristics.

Chapter 2 Saturn V Case Study

2.1 Saturn V Missions Overview and Engine Specifications

Apollo 10 is often described the "Lunar Mission Development", aiming to develop a support system for manned lunar missions as well as evaluate the lunar module's performance. The launch vehicle, as part of Saturn V mission architecture, included three different stages for the rocket, each one's activity logged and later published in NASA's Apollo/Saturn V Postflight Trajectory AS-505 [27].

The first stage, S-IC, utilized a total of 5 Rocketdyne F-1 engines from launch to roughly 66,000 m, lasting a total of 162 seconds. After hitting Mach 1 at 66.8s and a maximum dynamic pressure at 82.6, the F-1 center and outboard engines were cutoff before the separation command for the first stage from the rest was sent at 162.31s. The second stage, S-II, had five Rocketdyne J-2 engines active until the separation command at 553.5s, 187000m with the engine cutoffs happening shortly prior. The third stage, S-IV, consisted of the rocket reaching parking orbit quickly after at 713.76s and 191374m with one J-2 engine active. The activity logs show that the rocket lingers around 190km as part of the coast in Earth's parking orbit. This paper's focus will revolve around the early points in the launch as the ambient pressure changes during lift, causing underexpanded flow.

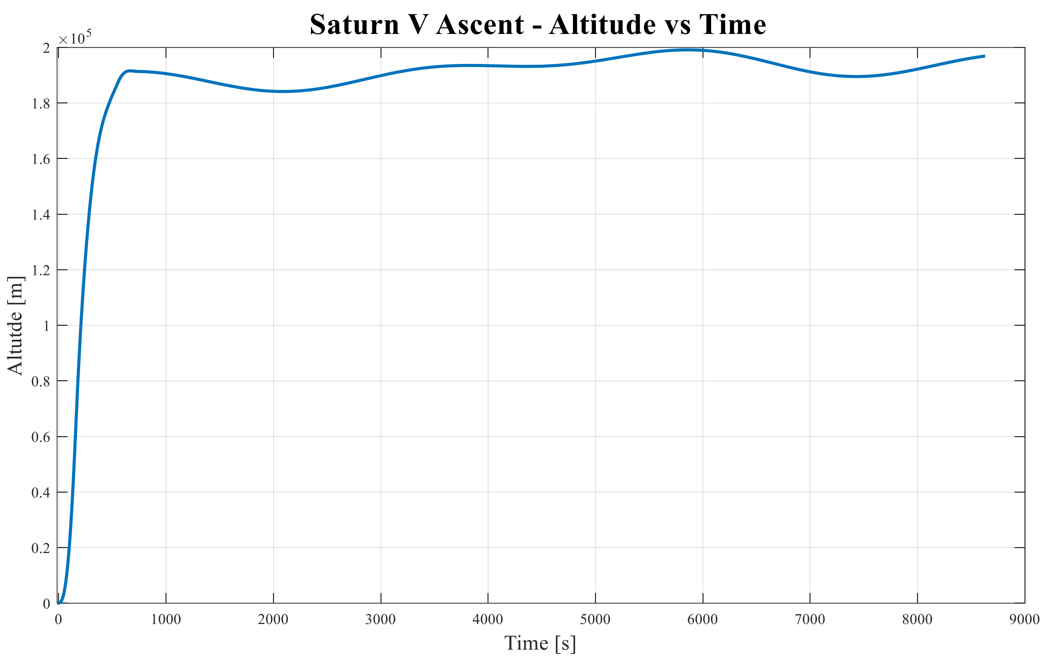

Figure 2.1 – Saturn V ascent

To center the calculations around the Saturn V, this paper will use the given nozzle specifications for the active engine during each stage. From the known altitude at a given point in time, one can determine which stage is active as it is also given in the postflight trajectory logs. With this information, this paper will use the active engine's specifications when calculating comparative metrics.

Table 2.1 – Nozzle specifications [23][24].

	F-1	J-2
Nozzle Exit Diameter [m]	3.5306	1.9558
Nozzle Expansion Ratio	16	27.5
Oxidizer: Fuel Mixture Ratio	2.27	5.5
Chamber Pressure [Pa]	6650000	5261000
Chamber Temperature [K]	3572	3450
Exit Pressure [Pa]	52535	21570

The oxidizer to fuel mixture ratio and the given rocket propellants' molecular weight can be used to determine the molecular weight of the mixture, later used in the calculations for each rocket.

Table 2.2 – Propellant specifications.

	F-1	J-2
Oxidizer	O_2	O_2
Oxidizer Molecular Weight [g/mol]	32	32
Fuel	RP-1	Liquid H_2
Fuel Molecular Weight [g/mol]	175	2.016
Average Molecular Weight [g/mol]	75.73	27.39

2.2 Fixed Geometry Approach

To quantify the performance of the rocket without any modifications, this paper will calculate the produced thrust by a single engine, exit velocity, coefficient of thrust, and specific impulse at each given time step. Performing these calculations will require the mass flow rate, the total molecular weight, and finally the exit pressure. The fluid pressure at the exit will employ isentropic relations, assuming only gradual changes with adiabatic flow, and calculate the Mach number at the exit using the area ratio, which can then be used to calculate the pressure at the exit.

$$\dot{m} = \frac{p_C A^* \gamma}{\sqrt{\frac{R_A}{M_W T_C}}} \tag{2.1}$$

$$M_W = \frac{M_F + M_O * (r)}{1+r} \tag{2.2}$$

$$\frac{A_e}{A^*} = \left(\frac{\gamma+1}{2}\right)^{-\frac{\gamma+1}{2(\gamma-1}} \frac{\left(1+\frac{\gamma-1}{2}M^2\right)^{\frac{\gamma+1}{2(\gamma-1)}}}{M} \tag{2.3}$$

$$\frac{p}{p^*} = \left(1 + \frac{\gamma-1}{2} M^2\right)^{\frac{-\gamma}{\gamma-1}} \tag{2.4}$$

From this point on, the calculations are relatively simple as other than the ambient pressure, which is already known, there are no changing variables. After processing the raw data, the calculations can be performed through a single for loop in MATLAB. Because different engines are active at different points of the ascent, the for loop contains if statements to ensure the calculations are performed for the active nozzles based on the altitude of the ascent.

2.3 Ideal Conditions Approach

In both the ideal and non-ideal conditions, the equations and nozzle specifications are nearly identical. The primary difference in the ideal approach consists of how the exit pressure is treated in all subsequent calculations. In the ideal case, the exit pressure equals the ambient pressure, so it is also a changing variable. The exit nozzle area, a function of the exit pressure, is consequently a function of time and thus a changing variable as well.

With these two changing variables, the generated thrust, exit velocity, coefficient of thrust, and specific impulse change at each time step with them. Once the ambient pressure equals zero as the altitude increases, it of course stops decreasing, making the rest of the variables static as well as the exit pressure stops changing.

2.4 Results and Discussion

Applying the methodology discussed for the two cases at each time step using code written in MATLAB produces the following results throughout the ascent of the Saturn V.

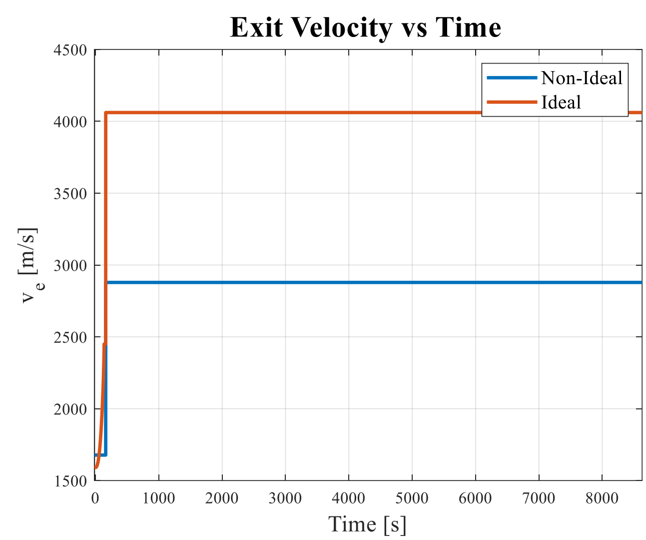

Figure 2.2 – Saturn V exit velocity vs. time.

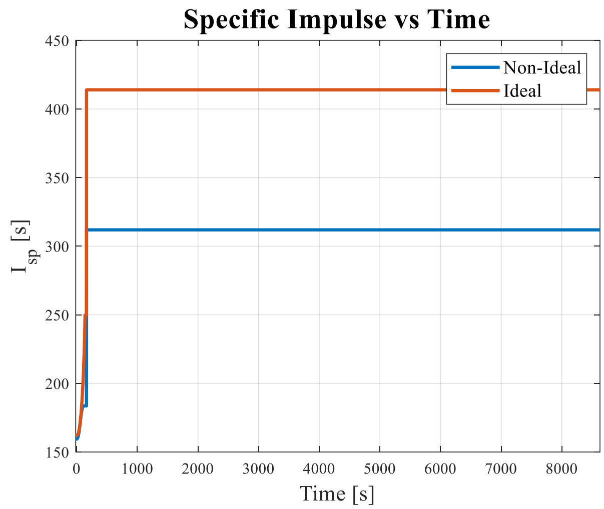

Figure 2.3 – Saturn V specific impulse vs. time.

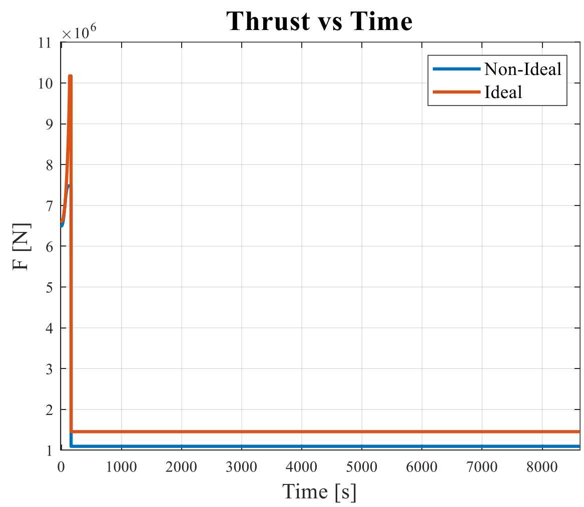

Figure 2.4 – Saturn V thrust vs. time.

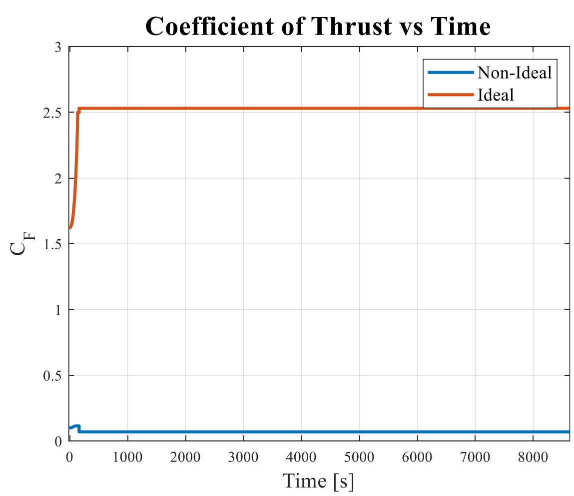

Figure 2.5 – Saturn V coefficient of thrust vs. time.

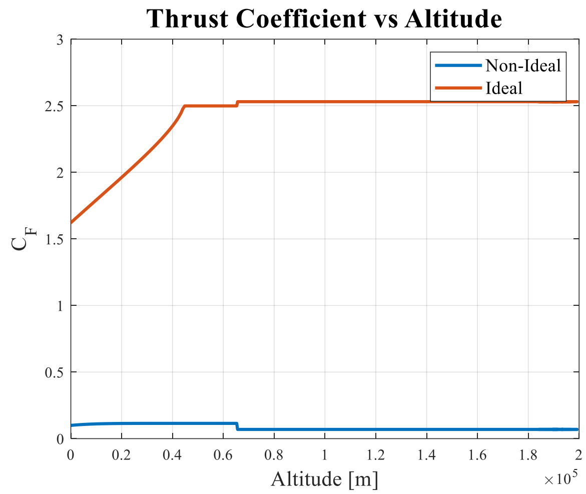

Figure 2.6 – Saturn V coefficient of thrust vs. altitude.

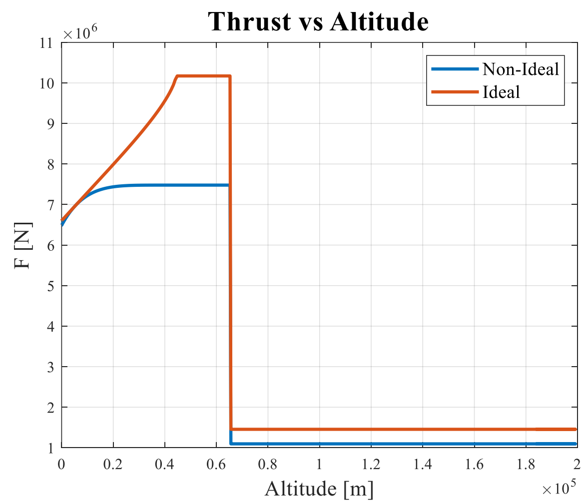

Figure 2.7 – Saturn V thrust vs. altitude.

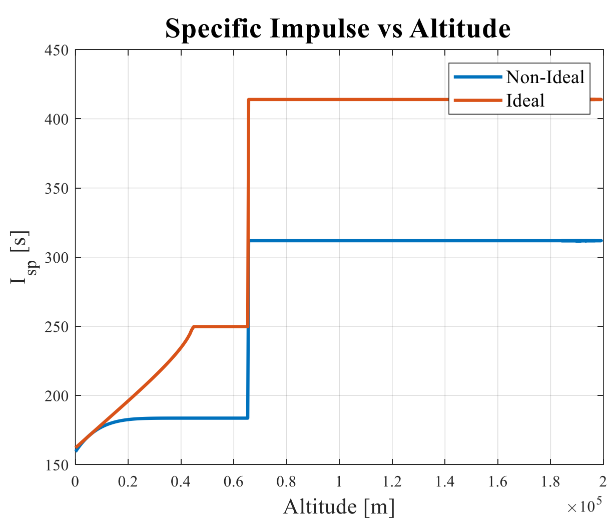

Figure 2.8 – Saturn V specific impulse vs. altitude.

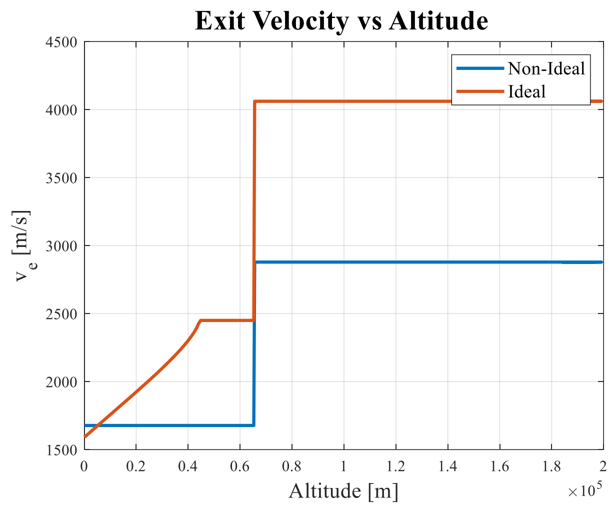

Figure 2.9 – Saturn V exit velocity vs. altitude.

The comparison in characterizing parameters showcases the advantages of an altitude compensation system. With fixed nozzle geometry, the propellant faces a resistive force as it attempts to exit the nozzle due to the discrepancy in the exit and ambient pressure. With a variable nozzle, the area adjusts accordingly to remove this loss, resulting in higher exit velocity, specific impulse, thrust, and coefficient of thrust.

The effectiveness and implementation of the variable nozzle is best shown when the ambient pressure changes. After around 44,000 meters, the ambient pressure is 0, so there is no change and thus the exit pressure also stops changing and produces static results. With changes in ambient pressure at lower altitudes, the exit area adapts to adjust the pressure which maximizes performance.

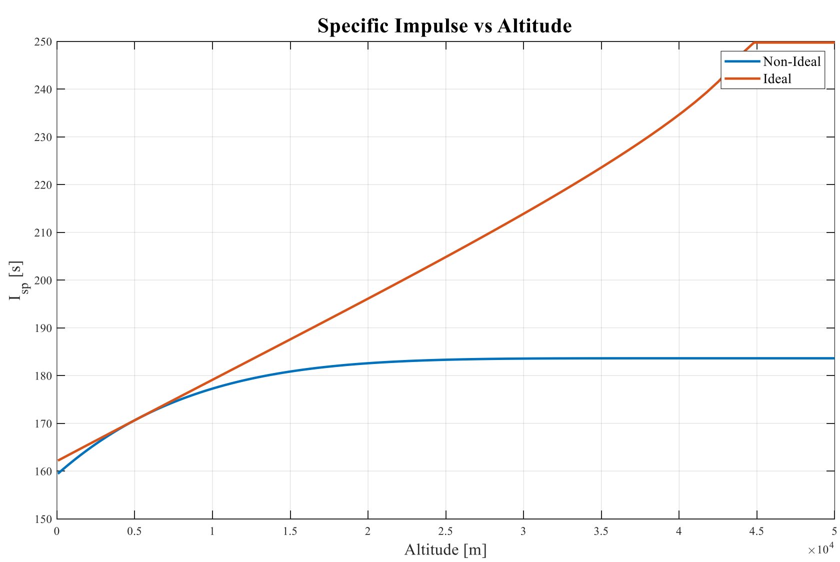

Figure 2.10 – I_{sp} changes with pressure changes.

Although the ideal method significantly increases the rocket performance, it does showcase the issue with a continuous altitude compensation system. As the ambient pressure decreases, the denominator in equation 1.3 continues to decrease as well, increasing the exit area to meet this demand. As the denominator approaches 0 at 44 km, the exit area approaches infinity so that there is no exit pressure. This, of course, cannot be met realistically and ultimately suggests a vacuum as that is what surrounds the nozzle.

This limitation means that a continuously adapted nozzle cannot satisfy the exit area requirements as the rocket reaches a vacuum and so the rocket cannot have ideal performance. The next section will discuss the development of optimal nozzle contours which may change in geometry as the altitude changes over time.

Chapter 3 Design of Ideal Nozzles via the Method of Characteristics

3.1 Theory

The method of characteristics is a system used to solve first order partial differential equations by reducing to ordinary differential equations. The method involves locating lines along the partial differential equation in which they can be reduced to a valid ordinary differential equation. Given the initial values, this reduction simplifies the problem significantly with the solution produced through concepts borrowed from calculus and linear algebra.

In reference to optimal nozzle design, the method of characteristics builds on flow field velocities derived using the Taylor series expansion of the finite-difference technique (3.1) with the irrotational flow conservation equations (3.2). The method of characteristics discovers the particular lines, henceforth referenced as characteristic lines, where the flow variables are continuous, but their derivatives are discontinuous (3.3). The ordinary differential equations obtained are valid only along these characteristic lines can be solved step by step from the given initial conditions[2].

$$u_{i+1,j} = u_{i,j} + (\frac{du}{dx})_{i,j}\Delta x + (\frac{d^2u}{dx^2})_{i,j}\frac{(\Delta x)^2}{2} + \ldots \tag{3.1}$$

$$(1-\frac{u^2}{a^2})\frac{du}{dx} + (1-\frac{v^2}{a^2})\frac{dv}{dy} - \frac{2uv}{a^2}\frac{du}{dy} = 0 \tag{3.2}$$

$$\frac{du}{dx} = \frac{\frac{2uvdu}{a^2\,dy} - (1-\frac{v^2}{a^2})\frac{dv}{dy}}{(1-u^2/a^2)} = 0 \tag{3.3}$$

$$(\frac{dy}{dx})_{char} = \frac{-uv/a^2 \pm \sqrt{[\frac{u^2+v^2}{a^2}]-1}}{(1-u^2/a^2)} \tag{3.4}$$

With algebraic and trigonometric manipulation, the method of characteristics produces a slope of the characteristic lines in terms of the Mach angle and angle between the streamline and x-axis (3.5). An elaboration of this shows that the Mach and flow angle represent the slope of two characteristic lines. The summation and difference of the two represent what are called the left-running and right running characteristics, denoted by C_+ and C_- shown respectively in Figure 3.1.

$$(\frac{dy}{dx})_{char} = tan(\theta \mp \mu) \tag{3.5}$$

$$d\theta = \mp\sqrt{M^2-1}\frac{dV}{V} \tag{3.6}$$

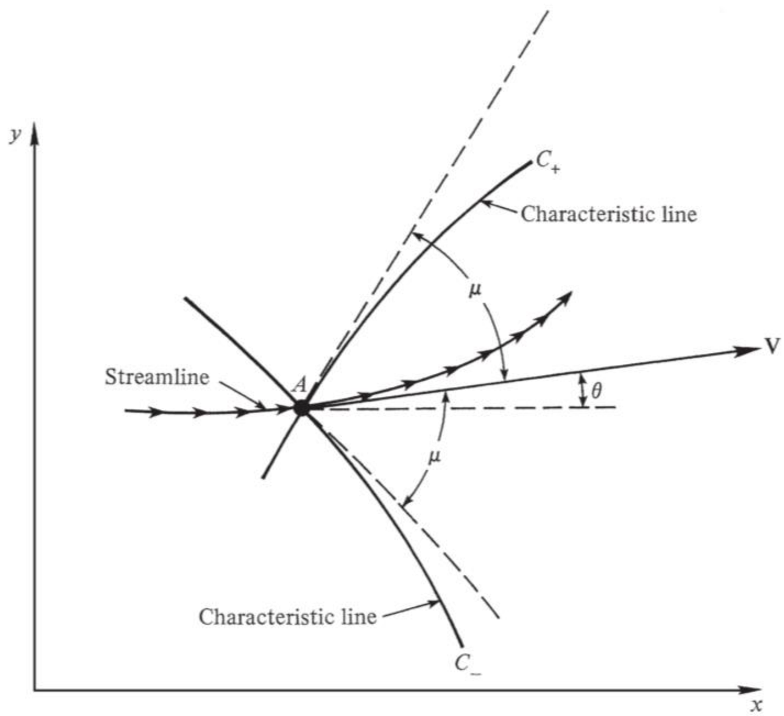

Figure 3.1 – Right and left running characteristics [2].

These characteristics provide the ability to relate the differential equations to flow properties such as the Mach number, eventually reducing the ordinary differential equations to the Prandtl-Meyer flow equation. From this, Anderson denotes a few constants which will resurface during the calculations for simplicity's sake (3.7).

$$\theta \pm \nu(M) = Const \ = \ K_{\mp} \tag{3.7}$$

Implementing the method of characteristics for internal flow requires the intersection of two characteristic lines, one from each of two previous points. The strength of the technique comes from its ability to know the properties of only two points upstream and predict the flow velocity and direction of a third point downstream. To apply this, the method examines the crossing of the summation Prandtl-Meyer function of C_- line and the difference of C_+ line. The properties at this point come from the constants denoted earlier which remain static along their respective characteristic lines. This static behavior at the first two points with straight curves intersecting provides the information at the third point.

$$\theta_3 \pm \nu_3 = (K_{\mp})_3 = (K_{\mp})_{1/2} \tag{3.8}$$

$$\theta_3 = \frac{1}{2}[(K_-)_1 + (K_+)_2] \tag{3.9}$$

$$\nu_3 = \frac{1}{2}[(K_-)_1 \ - \ (K_+)_2] \tag{3.10}$$

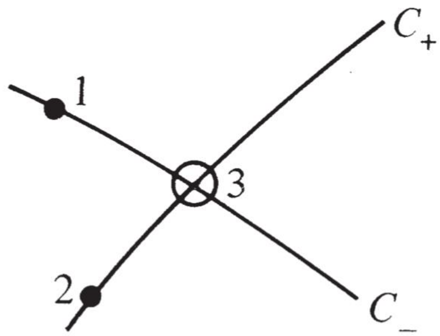

Figure 3.2 – Internal flow method of characteristics unit process [2].

Anderson also goes to derive a crucial step in the method of characteristics. For minimum length nozzles, Anderson shows the beginning flow angle θ at the throat's radius is the maximum and derives the following relation to the exit Mach number's Prandtl-Meyer function:

$$\theta_{w_{max}} = \frac{\nu_M}{2} \tag{3.11}$$

3.2 Application

The application of the method of characteristics requires a starting value with known coordinates and flow properties. At the throat, right before the expanding section of the nozzle, the flow properties and nozzle geometry are given by the engine specification sheets. As the nozzle throat shall remain constant, this provides a good starting point to begin drawing the characteristic lines to the nozzle center line.

For simplicity's sake during the calculations and descriptions, this report will categorize each of the points of interest in the technique into one of three categories:

1. Wall point, if the point is located on the nozzle contour wall.
2. Centerline point, if the point is located on the nozzle centerline where y = 0.
3. Middle point, if the point is neither of the two previous descriptions.

To start the process, characteristics lines are drawn from the starting point at the nozzle throat with a specified angle, $\Delta\theta$, in between each line. They trace out to the centerline, where y = 0 and the flow direction is straight ahead, so theta representing the flow angle also equals zero. Although it is noteworthy to add that one must give a small flow direction angle, e.g. $\theta = 0.3$, for the first centerline point to "kick-off" the technique, otherwise no calculations can be made. The slope of the characteristic lines at the centerlines comes from the calculated Mach number derived by the Prandtl-Meyer function. The Mach number gives the Mach angle, which turns out to be the slope of the left running characteristic at the center lines since $\theta_{center\ line} = 0$. To calculate the next centerline properties, one requires the right running characteristic for point after the previous centerline and the previous centerline point's left running characteristic.

For the middle points, if calculating points before the second centerline, the method uses the slope of the right running characteristic coming from the nozzle throat radius point. This point happens to have a slope of $\tan^{-1}(270°+(\Delta\theta*m)°)$, where m denotes the instances delta angle. For example, the first point after the first centerline point will have $m = 2$. For every other middle point after the first centerline point, the right running characteristic will use the $i\text{-}n\text{+}j\text{-}2^{th}$ point's, where i represents the current point, n the total number of characteristic, and j the current number of centerlines elapsed. In both cases, the left running characteristic will always use the previous points, so the $i\text{-}1^{th}$'s.

Flow calculations will not be performed for the wall points, as they will use the flow properties calculated at the $i\text{-}1^{th}$'s point. To calculate their coordinates with respect to the origin, however, one may use left running characteristic of the $i\text{-}1^{th}$'s point and the right running characteristic from the previous wall point to find the intersection of these two lines.

The end point only requires the exit speed. The exit speed, determined based on the exit pressure setting for optimal conditions, produces the Mach number. This Mach number feeds to what the maximum flow angle at the throat radius point should be by (3.11). which then defines the nozzle contour. Once a point calculated at the centerline meets this exit speed, this suffices the method of characteristics for minimum length nozzles.

3.3 Results

As the ambient pressure changes, the rocket nozzle geometry must change to maintain an ideal propulsive fluid exit pressure to match the surrounding ambient for highest performance. This optimal contour developed to support this geometry comes from the method of characteristics algorithm, which solves the governing equations to define the flow expansion throughout the nozzle to give an optimal contour. The algorithm may be implemented using MATLAB code using the application steps discussed in the previous section.

Knowing the exit conditions and general nozzle specifications, this report will calculate the optimal nozzle contour given the pressure setting at each altitude time step. The x-y coordinate points produced in the MATLAB algorithm define the contour, which SOLIDWORKS can rotate around the origin axis to produce a nozzle contour. This nozzle geometry will later be implemented in Ansys CFD to simulate a transient model of the rocket nozzle changing shape during its ascent and how this will affect the flow behavior with the changing ambient pressure.

Running the code with $n = 50$ characteristic lines with a $\Delta\theta = 0.56985°$ to achieve an exit Mach number of 2.4 produces geometry seen in Figure 3.3 and Figure 3.4. Although note that this is only a single instance of the nozzle geometry, as it will continue to change with each time step as the pressure changes.

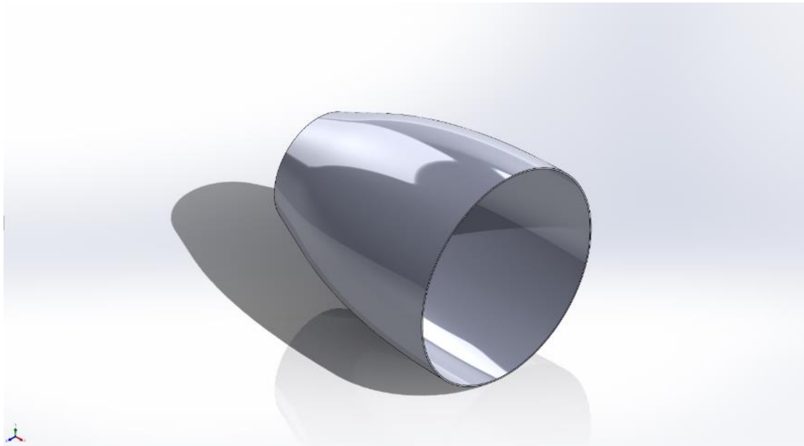

Figure 3.3 – Optimized nozzle using method of characteristics for M_e = 2.4, isometric view.

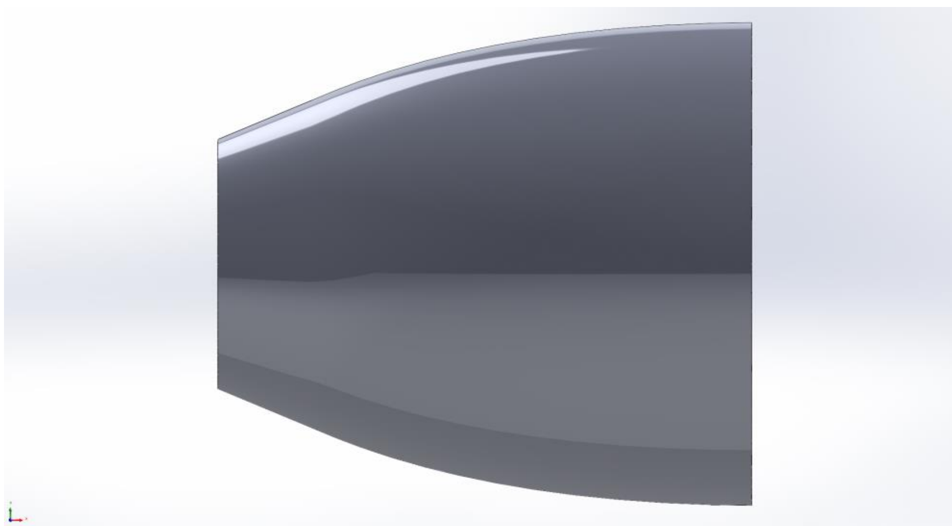

Figure 3.4 – Optimized nozzle using method of characteristics for M_e = 2.4, side view.

Chapter 4 CFD Applications for the Saturn V Case Study

4.1 Introduction

The CFD simulation will provide a good sanity check for the progress made so far by this report. This chapter aims to develop a steady-state, turbulent, viscous axisymmetric model from the geometry developed used in the method of characteristics. This modeling will reflect real-world conditions of the chamber and ambient air with calculations done in Ansys Fluent.

The foundational equations in the method of characteristics assume inviscid flow, which takes away the viscous forces at the nozzle contour boundaries. Ideally, the flow expands perfectly, allowing for an adapted nozzle given the ambient pressure boundary conditions, which may allow for maximum thrust. Ansys Fluent may provide some insight as to how these viscous forces affect the overall flow and what thrust one may expect at the nozzle exit. The method of characteristics predicts a thrust given the area ratio, but due the method's inviscid nature, the actual flow may deviate from reality. This is where CFD will come in.

To account for the viscous effects, this study will parametrize the nozzle dimensions and report the achieved thrust at the nozzle exit as the area ratio ranges from ±1, 2.5, 5, and 10% of the original. This same methodology may be applied at several altitudes to develop a correction factor from inviscid-assumed method of characteristics to viscous-expected CFD. Ideally, this paper may show a relationship so one may use the method of characteristics in tandem with the correction factor to account for viscous flows and develop an ideal nozzle contour.

The parametric study will run a CFD model for a total of 10 different altitudes. Each altitude, as a result of having a different ambient pressure, will have a different outlet pressure to have an ideally adapted flow. As previously discussed in this paper, this entails a different nozzle contour. The 5 different altitudes were selected by starting with the radius at time equals zero and linearly spacing 3 altitudes between the initial radius's associated Mach number and Mach 3.5.

Table 4.1 – Selected altitudes for simulation and their respective conditions.

Study	Ae [m^2]	Radius [m]	Me	Time [s]	Altitude [m]	Ambient Pressure [Pa]
1	7.35	1.530	3.115	0.00	64.00	100558.52
2	8.57	1.651	3.210	73.00	9773.00	27367.98
3	10.07	1.790	3.310	84.00	13769.00	14346.67
4	11.77	1.936	3.406	92.00	17162.00	7729.13
5	13.67	2.086	3.497	98.00	20002.00	4326.25

It is noteworthy to add that as the ambient pressure decreases, idealized exit conditions will predict larger exit areas. This will conclude with a predicted exit area of infinity as the ambient pressure reaches 0 as mentioned earlier. This constraint leads to selecting an exit radius which can be effectively modeled in CFD software but also one that covers a large enough range of exit conditions.

4.2 Geometry

The method of characteristics code generates a .csv file of an ideal nozzle contour's x-y coordinates. These coordinates may be inserted into Ansys' DesignModeler and given parametrized dimensions. Although the coordinates only consist of the half of a nozzle's cross section, they may be used in an axisymmetric flow simulation where the symmetry axis is the nozzle's centerline. This significantly reduces computational costs and simplifies the modeling process from a 3-dimensional simulation of a complete nozzle or 2-dimensional flow of a cross section down to only a 2-dimensional simulation of half of the nozzle's contour. This is done by assuming symmetric flow about the centerline.

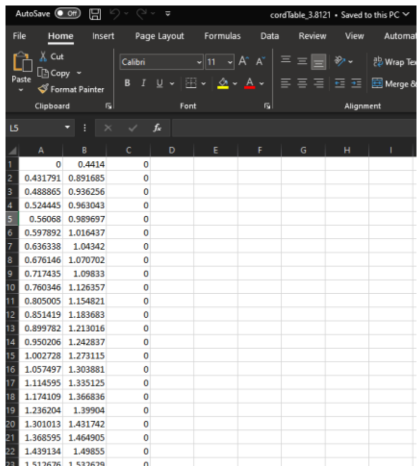

	A	B	C
1	0	0.4414	0
2	0.431791	0.891685	0
3	0.488865	0.936256	0
4	0.524445	0.963043	0
5	0.56068	0.989697	0
6	0.597892	1.016437	0
7	0.636338	1.04342	0
8	0.676146	1.070702	0
9	0.717435	1.09833	0
10	0.760346	1.126357	0
11	0.805005	1.154821	0
12	0.851419	1.183683	0
13	0.899782	1.213016	0
14	0.950206	1.242837	0
15	1.002728	1.273115	0
16	1.057497	1.303881	0
17	1.114595	1.335125	0
18	1.174109	1.366836	0
19	1.236204	1.39904	0
20	1.301013	1.431742	0
21	1.368595	1.464905	0
22	1.439134	1.49855	0

Figure 4.1 – Outputted .csv file by method of characteristics example.

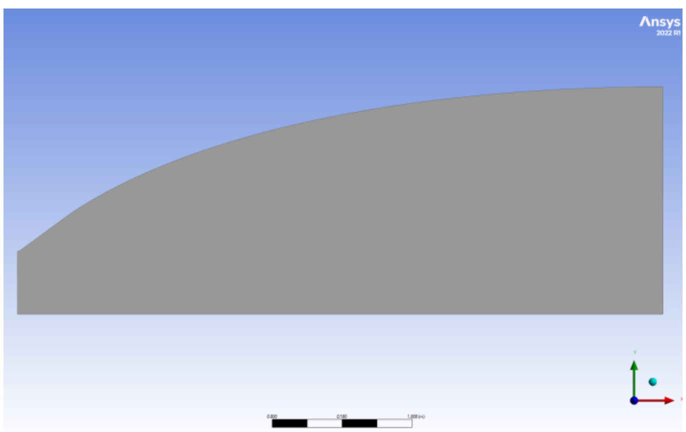

Figure 4.2 – Method of characteristics coordinates translated into DesignModeler.

These coordinates, however, are not enough. The method of characteristics outlines only the diverging section of the converging-diverging nozzle. The diverging section may be created relatively simply using a few line and curve additions which may allow for the flow to choke at the throat. Any converging geometry upstream of diverging section would achieve this as the choked conditions are a function of the area which is fixed at the throat.

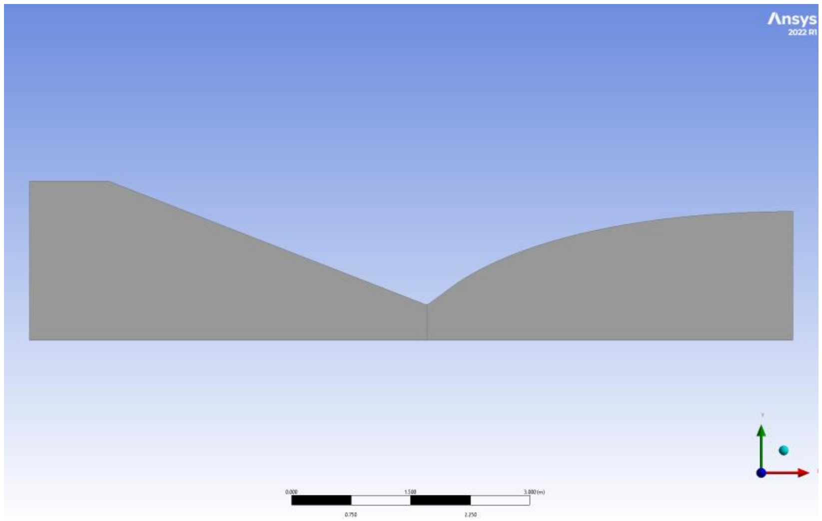

Figure 4.3 – Added arbitrary nozzle converging section.

Due to the nature of CFD requiring a complete simulation domain, the geometry will also require a chamber leading to the diverging section as well as domain downstream of the nozzle. The chamber can simply be a rectangular addition to the diverging section to provide an inlet boundary condition for the flow. For the downstream simulation domain, one may provide ample distance to observe the flow fields resulting from the nozzle.

The meshing section will require different sections to apply the mesh features to. This partitioning will be done in the geometry section. To do this, one draws a line separating the two faces of interest and uses the split tool in DesignModeler. This process can be applied to produce isolated faces for the diverging, converging, and downstream section of the nozzle. Although it will vary for each altitude, the resulting geometry for an example case may look like Figure 4.4.

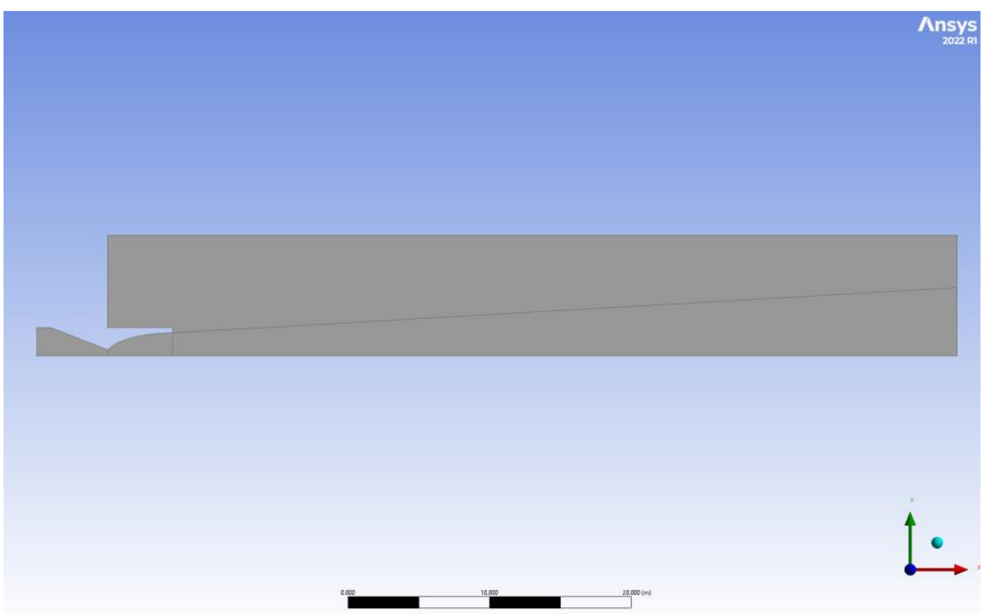

Figure 4.4 – Final geometry example.

4.3 Physics

One of the most important aspects of this chapter will revolve around the physics employed in the simulation. In Ansys Fluent, the selected physics will determine which equations are used by the solver. This report only anticipates heat transfer and momentum, so only the energy equation is enabled with viscous effects assumed under the realizable k-epsilon turbulence model. The realizable k-epsilon model used in this simulation will serve well to capture the expected viscous effects and also to resolve turbulence far from walls and boundary layers.

To solve the steady state equations, this report will use a pressure-based solver with absolute velocity formulation. As mentioned before, the two-dimensional space will assume axisymmetric flow in the calculations. The pressure-velocity solver will employ a coupled scheme with second order discretization for the pressure and second order upwind for the density, momentum, turbulent kinetic energy, turbulent dissipation rate, and energy solvers. This will provide slightly more accurate results and account for compressible flow in the coupled solver.

Although the fluid domain will be air in the simulation, the report will use ideal-gas density with a Sutherland estimation of the viscosity.

4.4 Meshing

A fine mesh is imperative for meaningful results. However, a too fine of a mesh may prove unnecessary and computationally taxing. The important aspect of meshing is balancing this multi-objective system. In this section, this report will outline the features used to develop the mesh used in the CFD model.

To begin, the model applied a triangular mesh for the entire simulation domain. Ansys defaults to a rather coarse mesh, which prompts the user to implement sizing controls. The diverging section’s nozzle has an element size of 0.025m but the converging and chamber remain at 0.0375m as the flow gradient is likely to remain low in these sections. The diverging section’s nozzle contour had an edge sizing of 0.0075m applied. This, with 6 inflation layers over the contour wall, significantly refined the cells to effectively capture viscous effects in the boundary layer.

This level of refinement is only needed in areas of large gradients. Not needing high accuracy in downstream of the nozzle provides an opportunity to save computational costs by reducing cell size. An edge sizing at the nozzle exit of 0.05m with a 1.005 growth rate and an edge sizing of 0.175m at the pressure outlet allows for cell size to continue to increase downstream of the nozzle.

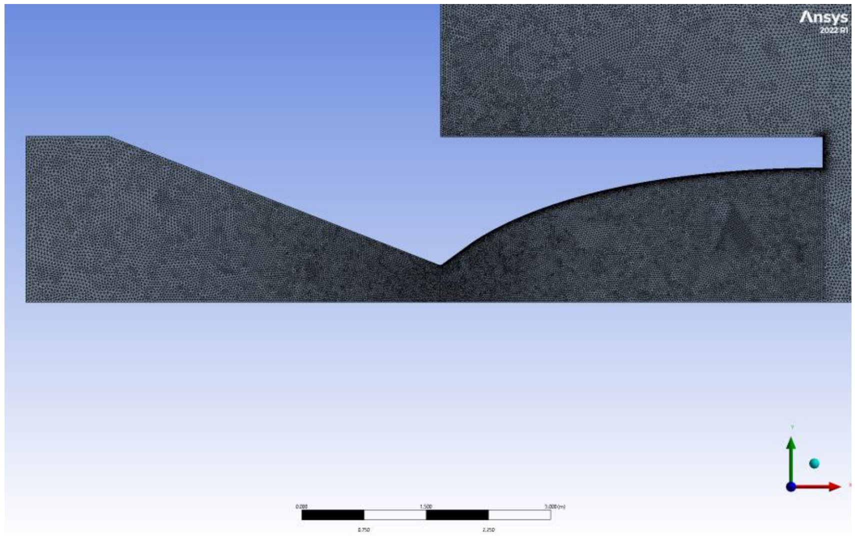

Figure 4.5 – Converging-Diverging section's mesh controls.

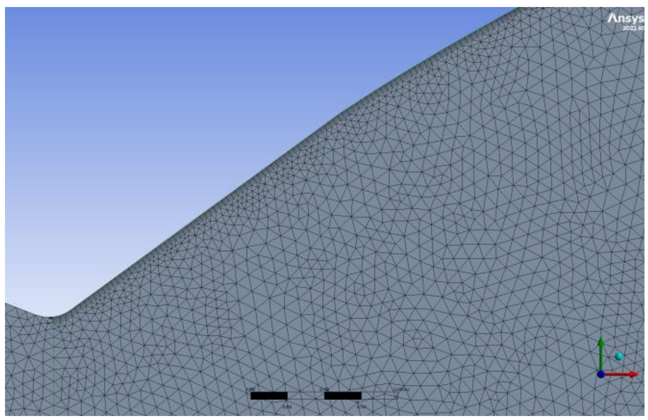

Figure 4.6 – Converging-Diverging section's mesh controls – focus.

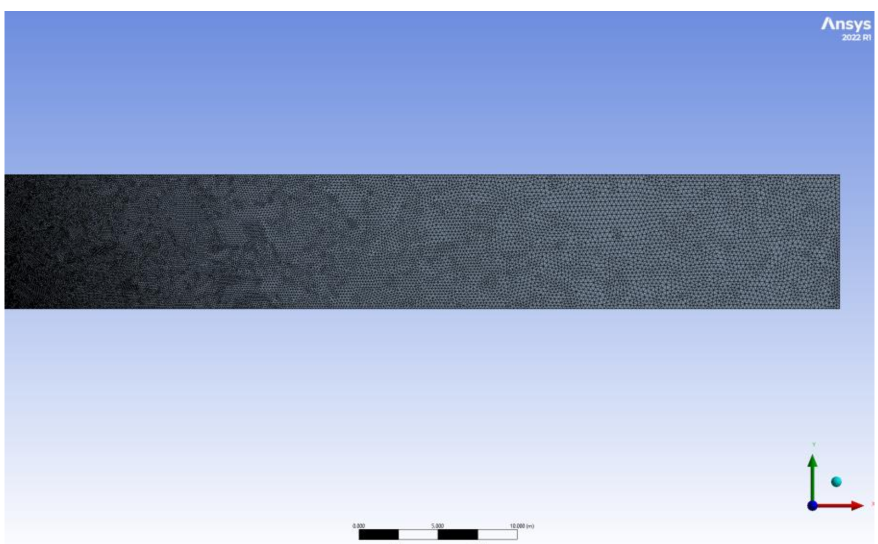

Figure 4.7 – Downstream mesh controls.

Together, these mesh controls produce a mesh refined in areas requiring high precision and relaxed in areas downstream of large gradients.

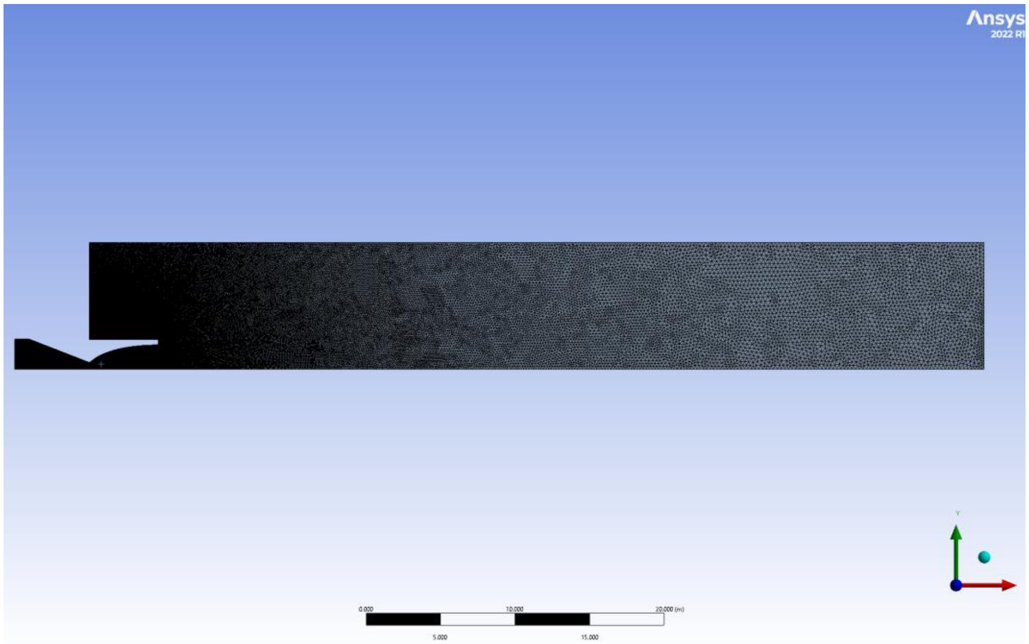

Figure 4.8 – Resulting mesh.

Prior to proceeding with the CFD setup, the mesh developer allows for naming different sections of the mesh. This allows for Ansys to automatically prepare the geometry for the boundary conditions based on the naming scheme. The inlet of the pressure chamber will be named pressureInlet, the farfield boundaries pressureOutlet, and everything else besides the symmetry axis, which will be named axis, shall be a wall. One final named section will involve the edge at the nozzle exit, which may be used for calculating the generated thrust.

4.5 Boundary Conditions

When opening Ansys Fluent's CFD Setup, it will automatically import the developed geometry and mesh. Using the named sections, it will also automatically apply some boundary types to each face and edge. The entire fluid domain, which is just a single face, will be an Internal type of boundary to signify where the fluid flow will take place. The remaining edges will vary depending on their location to simulate the fluid flow of interest.

The farfield edges, which are ultimately the edge of the domain, will act as a pressure outlet with ambient air conditions depending on the case of interest. The chamber wall perpendicular to the axis may complete the fluid flow direction by acting as a pressure inlet with the respective rocket engine's chamber conditions. All the edges of the nozzle as well as the roof of the chamber parallel to the axis will guide the flow with their wall boundary conditions.

To save computation costs as mentioned before, this simulation will only simulate half of a cross section and assume symmetry along the centerline, which will require the bottom edge to act as an axis which the symmetry revolves around. This in turn completes the boundary conditions and produces expected fluid flow as shown in Figure 4.9.

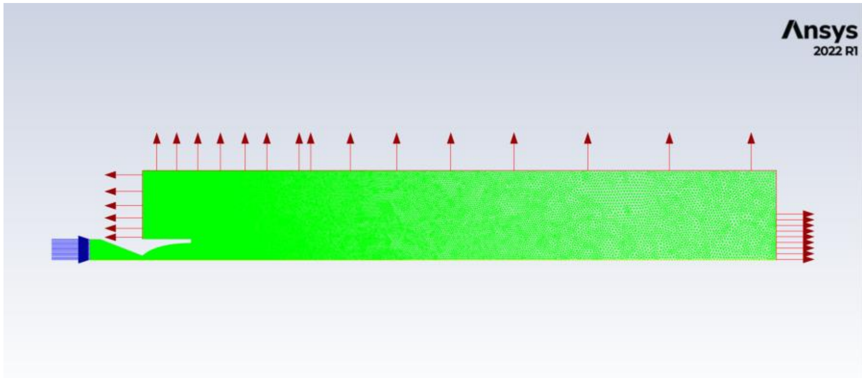

Figure 4.9 – Boundary conditions applied.

4.6 Parametrization

Ansys Workbench offers convenient methods to run parametric studies. This report aims to develop a relation between the ideal contour predicted by the method of characteristics and what may take place under real-world conditions. The discrepancy between the two may occur as a result of the inviscid assumptions in the method of characteristics, so Ansys Fluent may bridge the gap between theory and reality. This bridge will ultimately take shape as a dimensionless correction factor that will offer insight as to how a generic method of characteristics code may be used to develop a nozzle contour fit to account for viscous flow.

Developing this correction factor will require a changing geometry. This may be implemented by simply importing the x-y coordinates developed by the method of characteristics into Ansys's DesignModeler and running a parametric study to expand and contract the nozzle geometry by a factor of 1, 2.5, 5, and 10% of the original geometry. Each changed geometry may be considered as a different case. Assigning dimensions in DesignModeler and then selecting the features for parametrizing will create a parameter set requesting input for each case. Each case, denoted as a "design point" or "DP" for shorthand by Ansys, will intake the respective case's calculated geometry value for each dimension. This completes the required input in the parametric study.

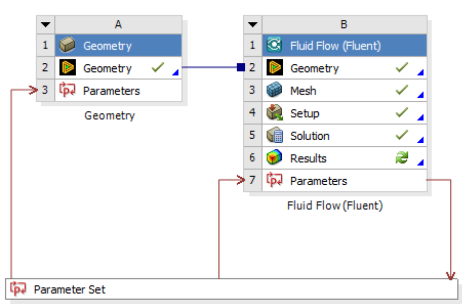

Figure 4.10 – Parametrization design scheme in Ansys Workbench.

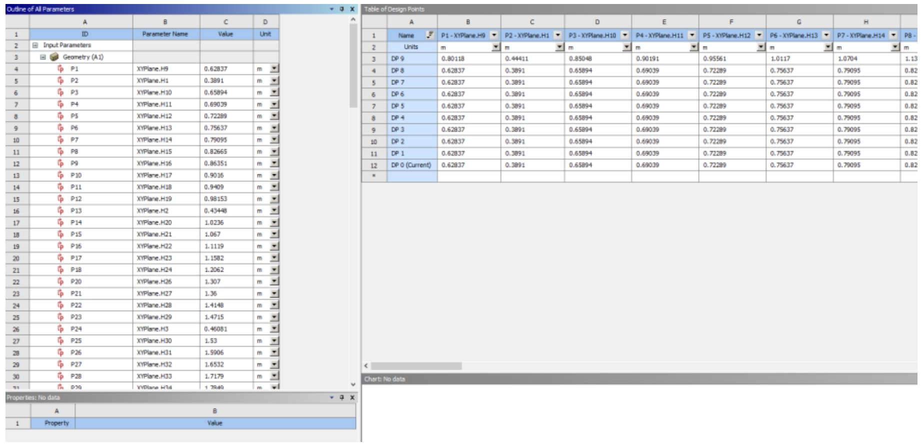

Figure 4.11 – Parametrization design point inputs.

Each parametric study will output a force value to signify the generated thrust. Calculating the thrust involves taking the integral of a custom user-defined field function, denoted by the Equation 4.1. Fluent conveniently outputs this parameter by first creating it as an integral type report definition across the nozzle exit and then enabling the "Create Output Parameter", which will save and display the value at the end of the iteration count in the parametric study for further analysis.

$$F_T = \rho v_e^2 + (p_e - p_a) \tag{4.1}$$

4.7 Results

The total of 9 simulations ran for each of the 5 altitudes results in a total of 45 simulations. Considering each simulation will highlight a few images each, the below results will include the velocity profile shown as the Mach number, static temperature, and the static pressure for only the first parametric study.

Original geometry results:

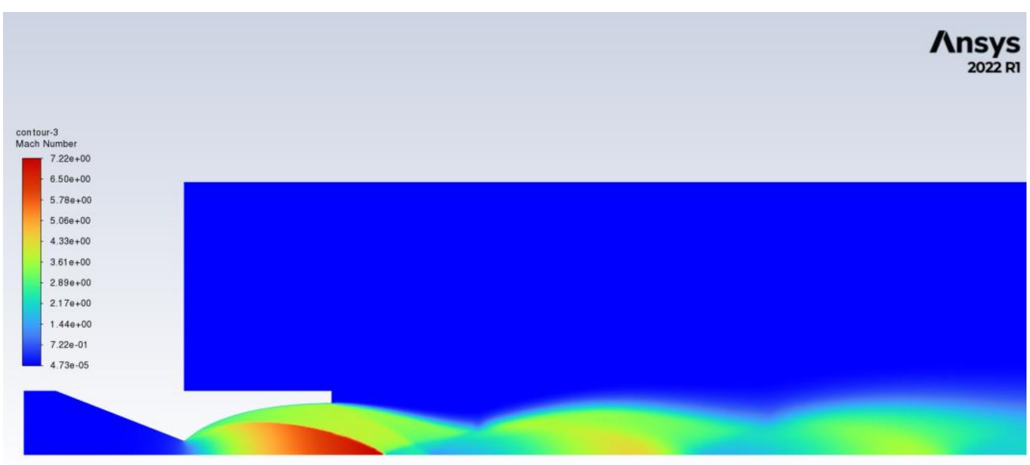

Figure 4.12 – Original geometry Mach number contour.

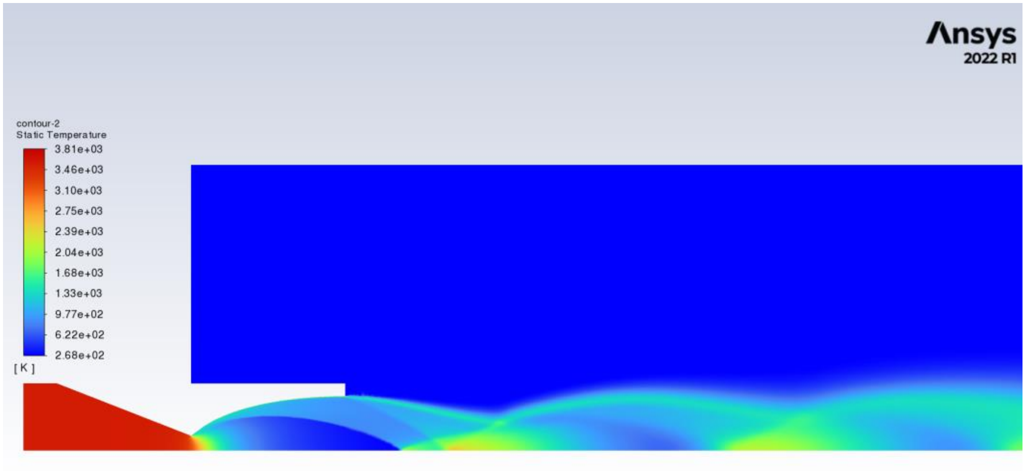

Figure 4.13 – Original geometry static temperature contour.

Figure 4.14 – Original geometry static pressure contour.

1.0% geometry decrease:

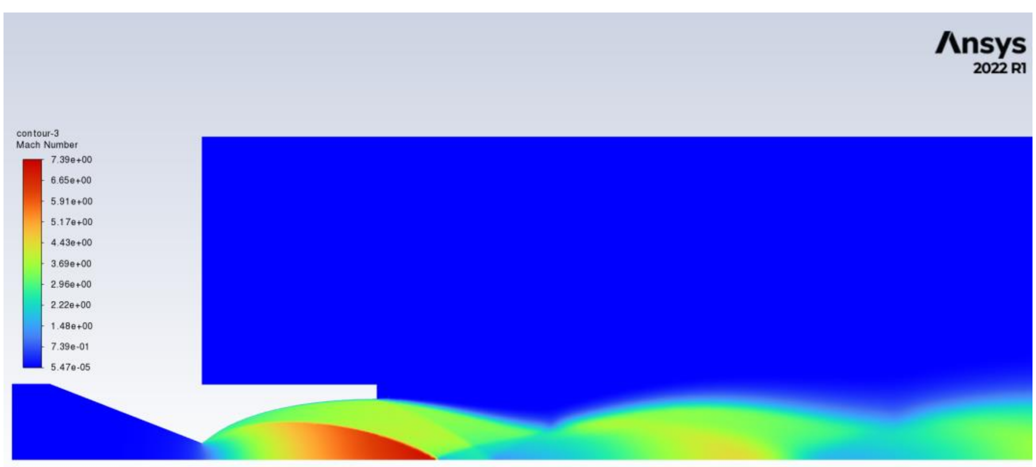

Figure 4.15 – 1.0% geometry decrease Mach number contour.

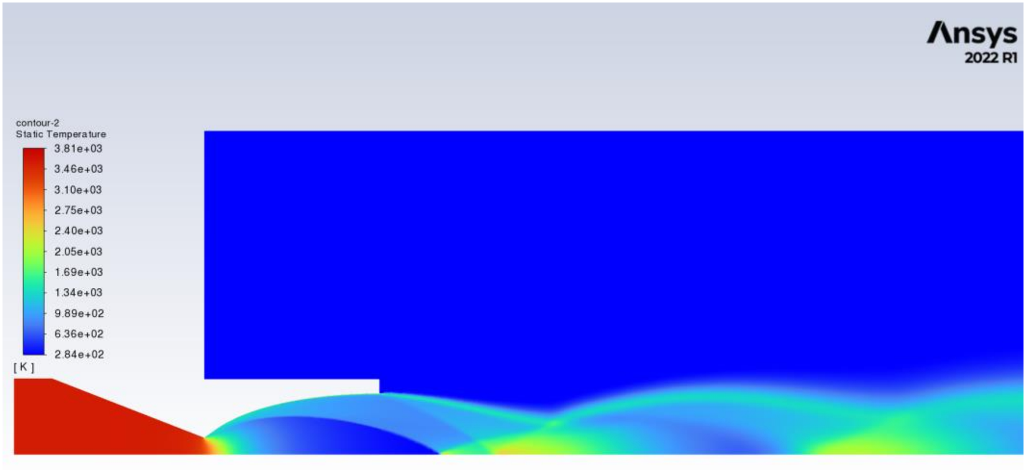

Figure 4.16 – 1.0% geometry decrease static temperature contour.

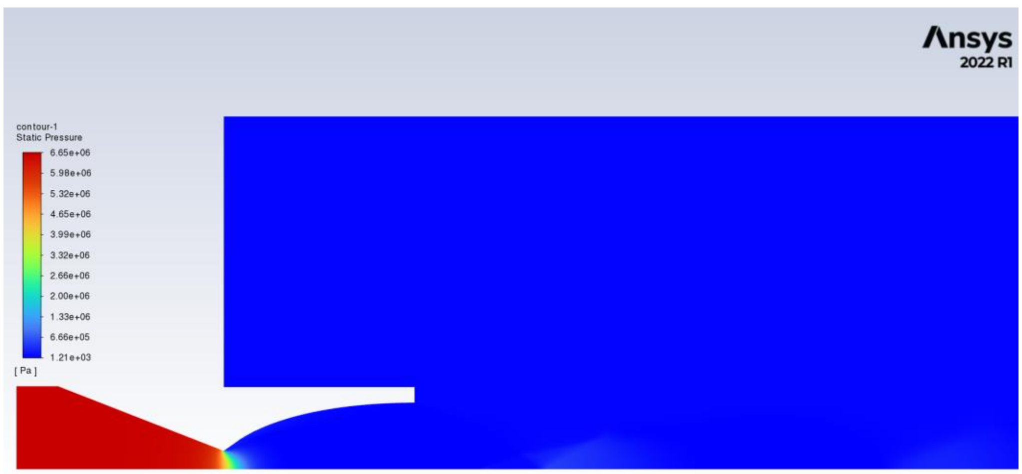

Figure 4.17 – 1.0% geometry decrease static pressure contour.

2.5% geometry decrease:

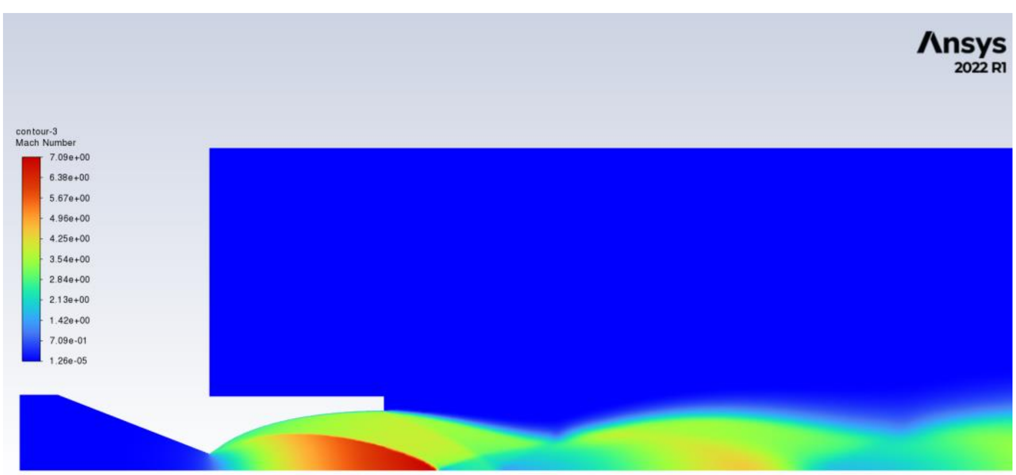

Figure 4.7.1 – 2.5% geometry decrease Mach number contour.

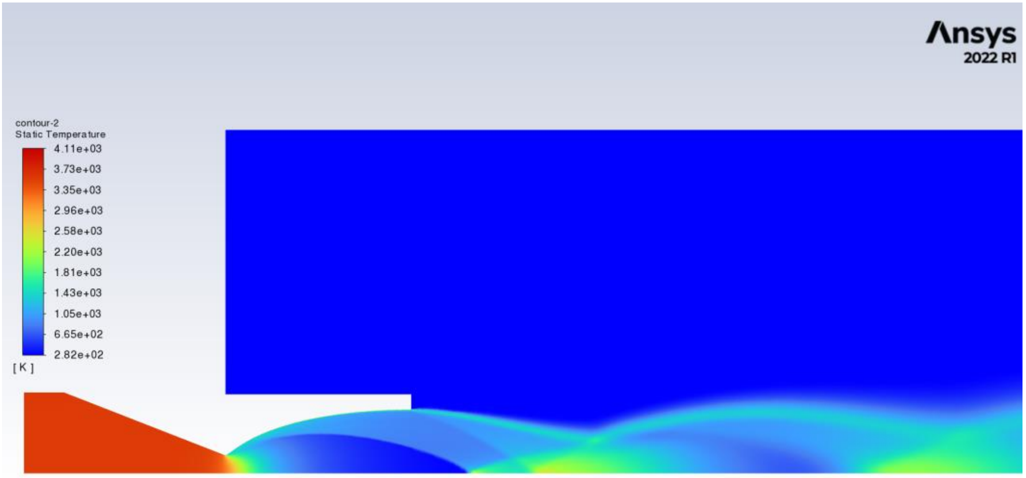

Figure 4.18 – 2.5% geometry decrease static temperature contour.

Figure 4.19 – 2.5% geometry decrease static pressure contour.

5.0% geometry decrease:

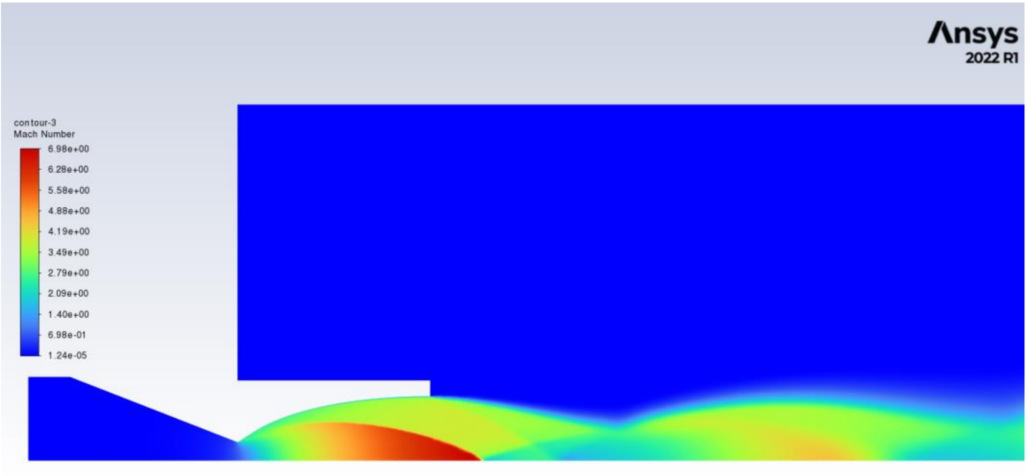

Figure 4.20 – 5% geometry decrease Mach number contour.

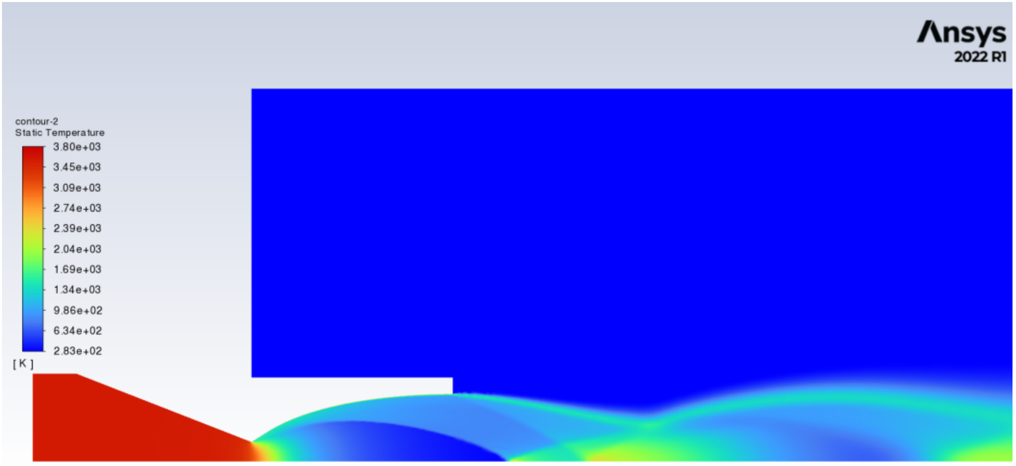

Figure 4.21 – 5% geometry decrease static temperature contour.

Figure 4.22 – 5% geometry decrease static pressure contour.

10% geometry decrease:

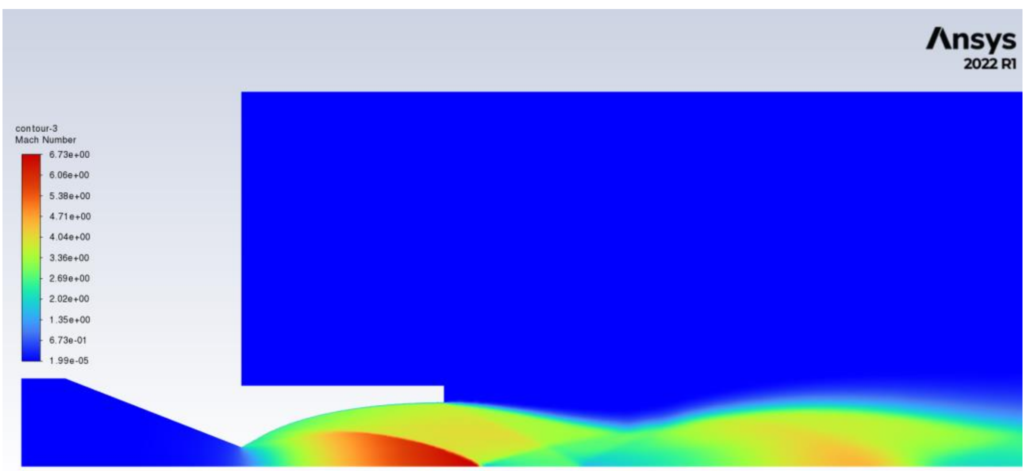

Figure 4.23 – 10% geometry decrease Mach number contour.

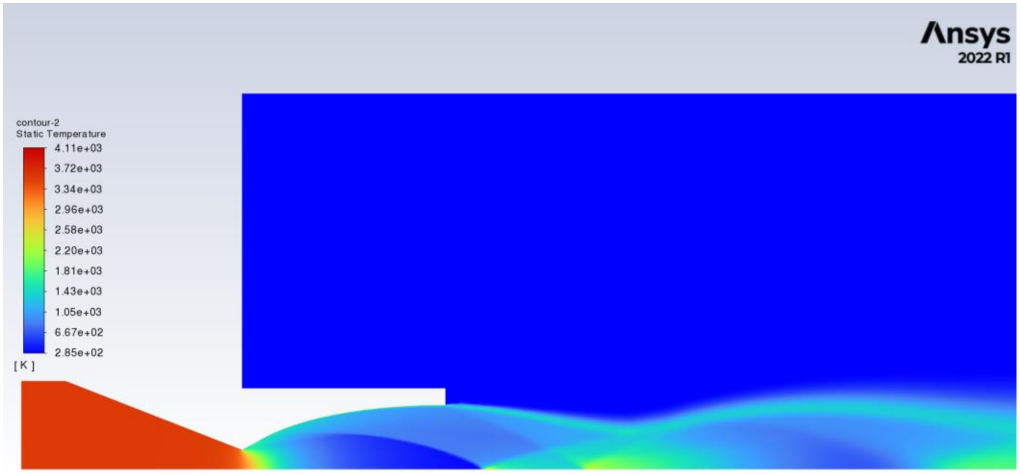

Figure 4.24 – 10% geometry decrease static temperature contour.

Figure 4.25 – 10% geometry decrease static pressure contour.

10% geometry increase:

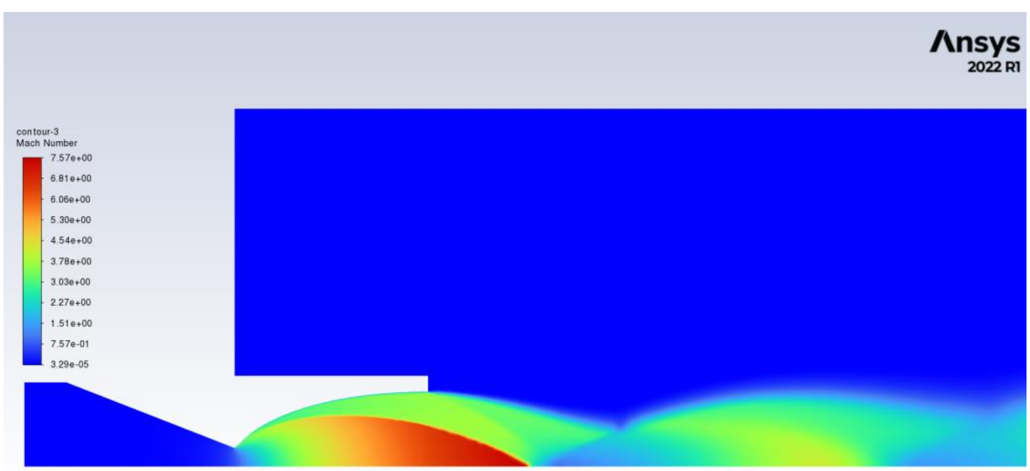

Figure 4.26 – 10% geometry increase Mach number contour.

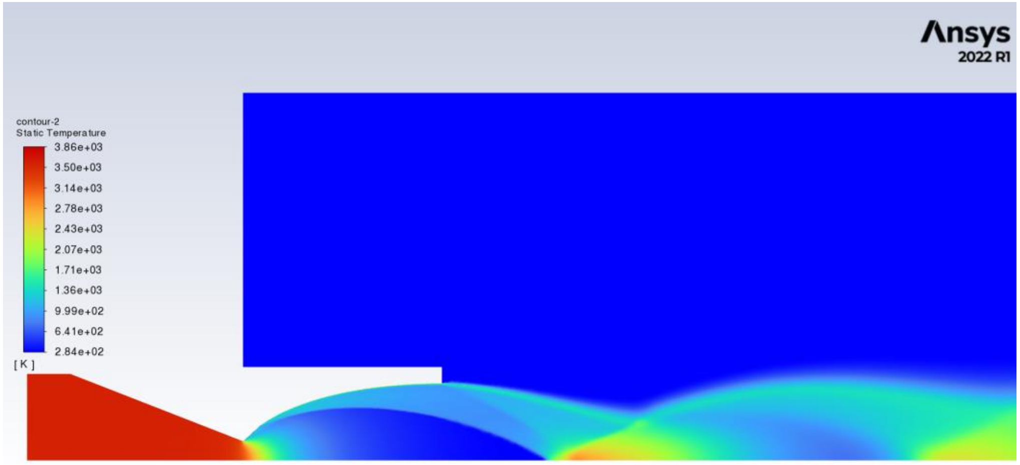

Figure 4.27 – 10% geometry increase static temperature contour.

Figure 4.28 – 10% geometry increase static pressure contour.

5% geometry increase:

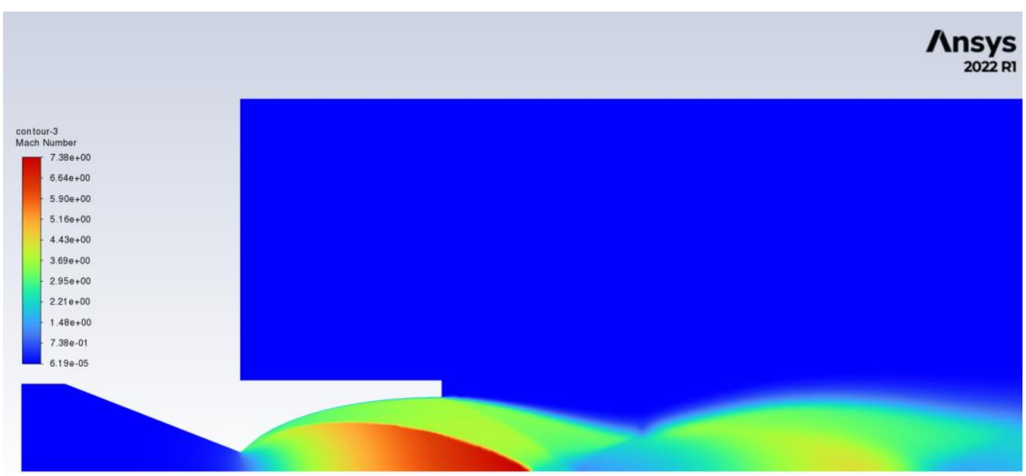

Figure 4.29 – 5% geometry increase Mach number contour.

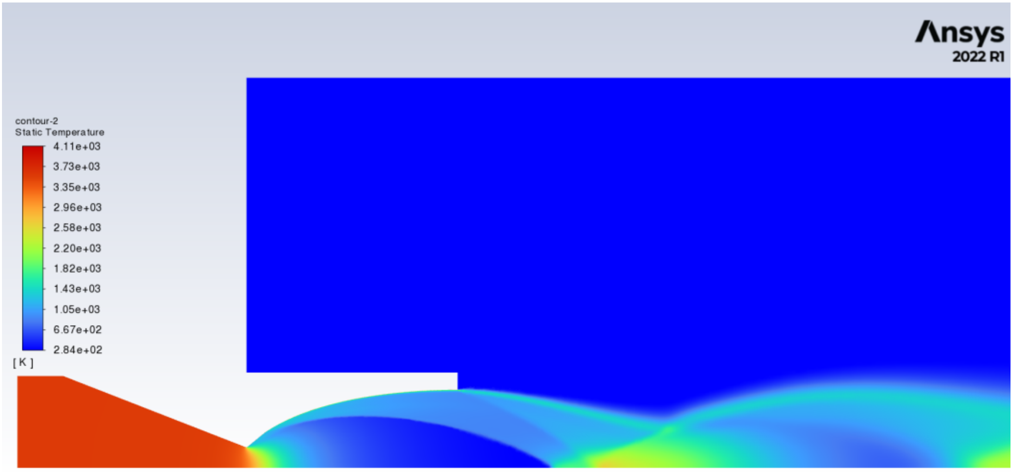

Figure 4.30 – 5% geometry increase static temperature contour.

Figure 4.31 – 5% geometry increase static pressure contour.

2.5% geometry increase:

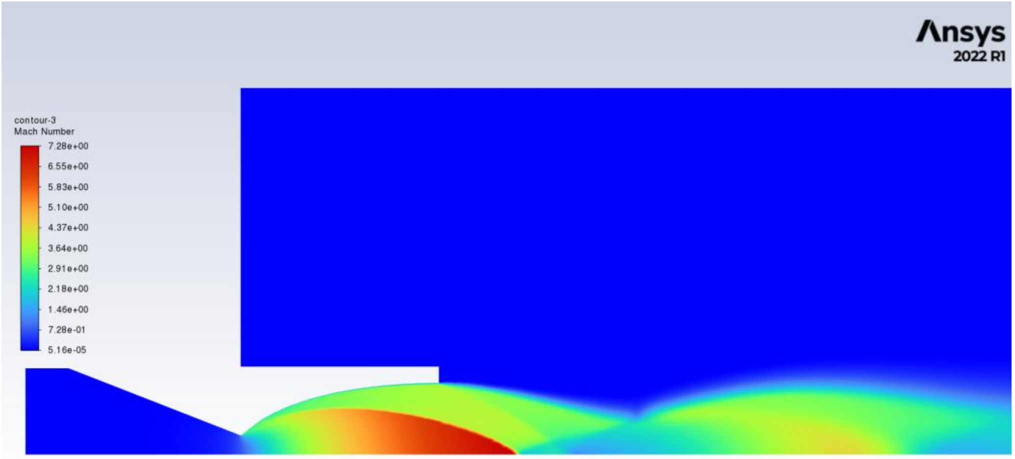

Figure 4.32 – 2.5% geometry increase Mach number contour.

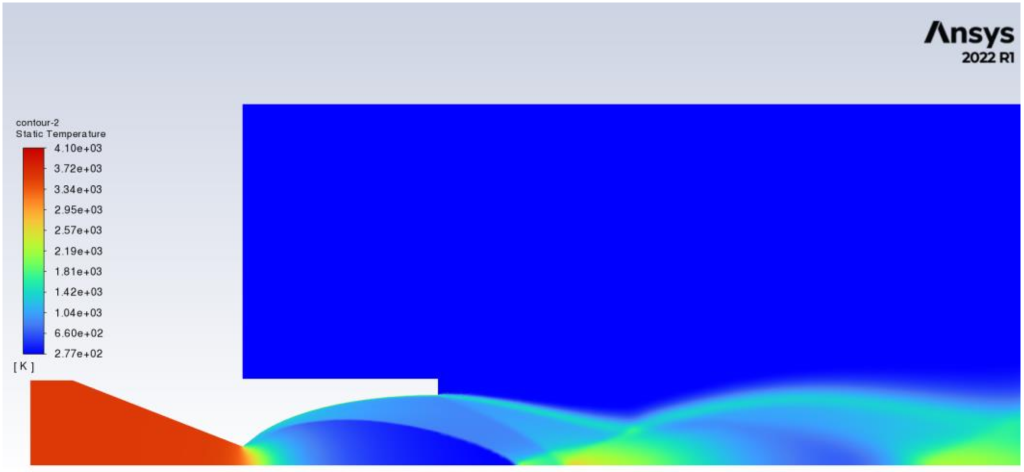

Figure 4.33 – 2.5% geometry increase static temperature contour.

Figure 4.34 – 2.5% geometry increase static pressure contour.

1% geometry increase:

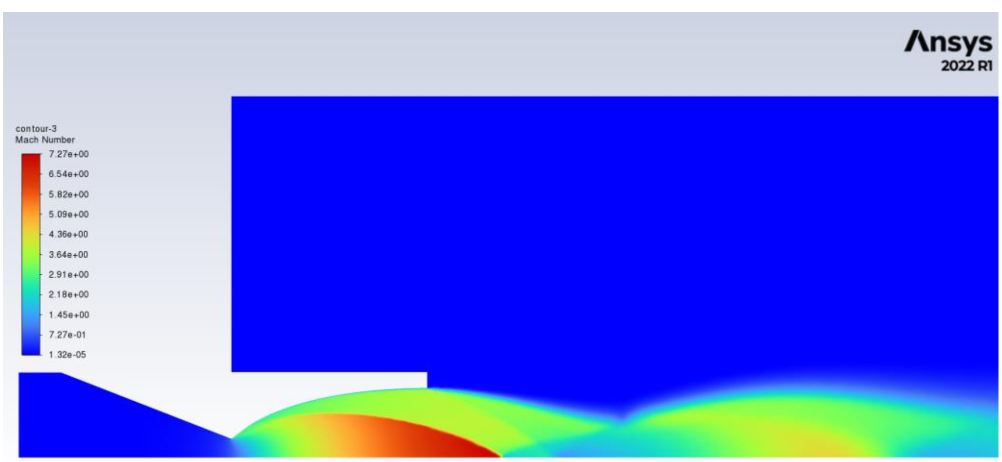

Figure 4.35 – 1% geometry increase Mach number contour.

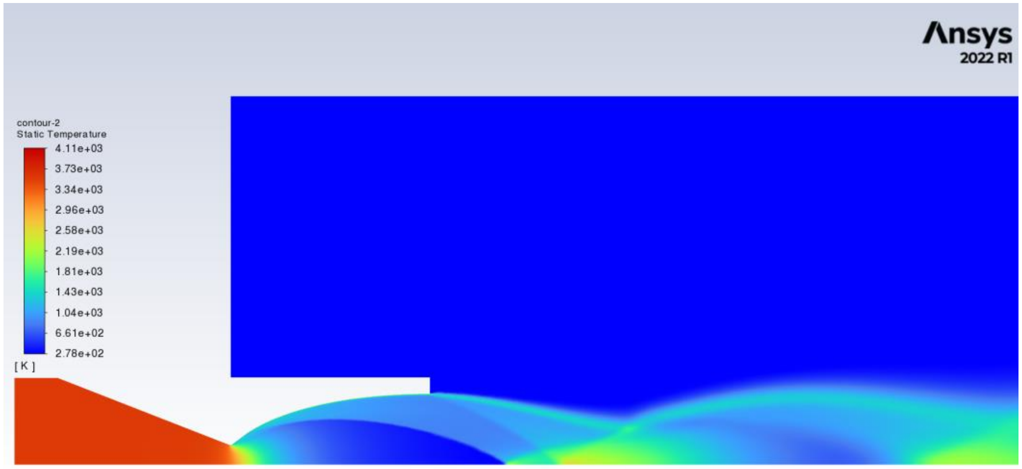

Figure 4.36 – 1% geometry increase static temperature contour.

Figure 4.37 – 1% geometry increase static pressure contour.

To calculate the thrust in Ansys, one may first create a custom user-defined function for Equation 4.2. The surface integral of this function at the nozzle exit produces the total force generated as a result of the mass expulsion from the contour. Tabulated in Table 4.2-Table 4.4, this surface integral produced the below thrusts for all 5 studies focusing on the F-1 engine.

$$\rho v_{axial}^2 + (p - p_a) \tag{4.2}$$

Table 4.2 – CFD thrust results for 5 studies with no contraction or expansion.

Study #	Analytical Mach Number	100%
1	3.1411	5750115
2	3.21	6357069
3	3.31	6490874
4	3.406	6598937
5	3.497	6675141

Table 4.3 – CFD thrust results for 5 studies at indicated expansions.

Study #	Analytical Mach Number	110%	105%	102.50%	101%
1	3.1411	6889997	6321971	6035889	5861539
2	3.21	7627518	6978002	6671700	6487616
3	3.31	7800460	7120957	6824463	6609949
4	3.406	7923452	7252994	6921206	6731118
5	3.497	8017461	7319303	6986330	6797467

Table 4.4 – CFD thrust results for 5 studies at indicated contractions.

Study #	Analytical Mach Number	99%	97.50%	95%	90%
1	3.1411	5637769	5480034	5205385	4686939
2	3.21	6234213	6052109	5764764	5181338
3	3.31	6364207	6172490	5870011	5291490
4	3.406	6462588	6281106	5967966	5378126
5	3.497	6537402	6353171	6028318	5439768

4.8 Validation

The residual and exit thrust plots as a function of the iterations offered a convenient way to determine convergence for each simulation. A converged simulation has a higher likelihood of having meaningful results and indicates the solver has reached an answer. Although this does not by default imply the produced answer is the true solution, convergence does provide a convenient sanity check for the simulation setup. Below, one may find the plots for the residuals and calculated thrust for each simulation’s 2500 ran iterations. Again, for the sake of brevity, shown are only the first study’s plots.

The partly oscillatory behavior observed in some of the residual plots may be attributed to the physics modeled or aspects of the meshing itself. Considering that the oscillations did not remain constant as the geometry changed, there is good likelihood that the meshing may be affecting this performance.

Despite the small oscillatory behavior in the residuals, the flatlined calculation of the force indicates a good reason to assume that the solution has converged. This convergence adds validity to the results flow fields predicted by the computational fluid dynamics solution is not dependent on the iteration count. This also verifies that 2500 iterations suffice for this application and no further computational resources as the solution will not change.

Original geometry:

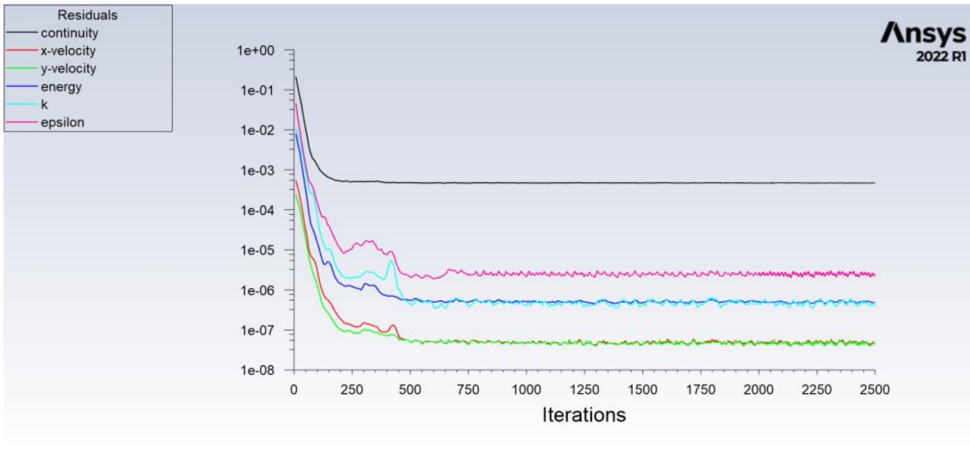

Figure 4.38 – Original geometry residuals per iteration.

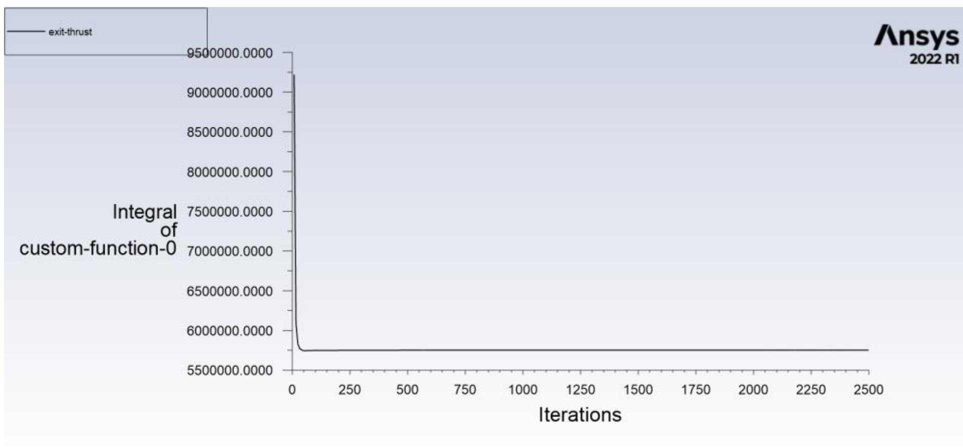

Figure 4.39 – Original geometry exit thrust calculation per iteration.

1% geometry decrease:

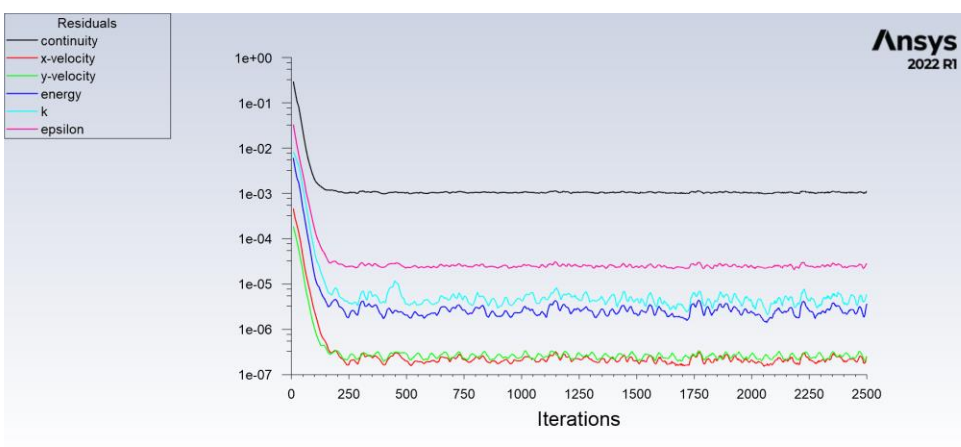

Figure 4.40 – 1% geometry decrease residuals per iteration.

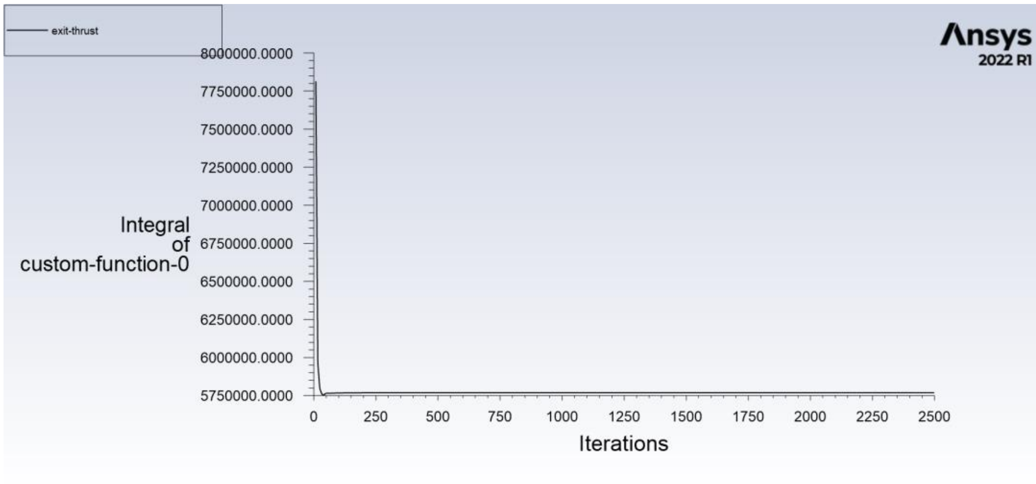

Figure 4.41 – 1% geometry decrease exit thrust calculation per iteration.

2.5% geometry decrease:

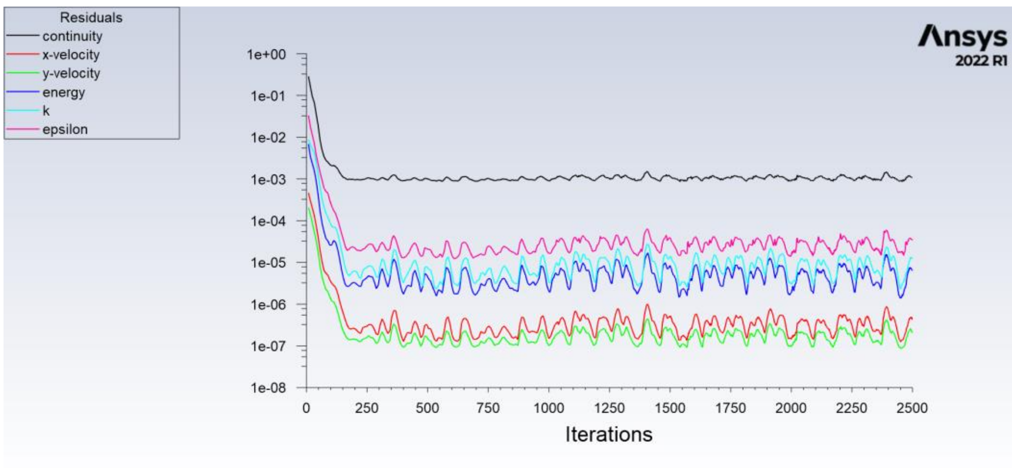

Figure 4.42 – 2.5% geometry decrease contour residuals per iteration.

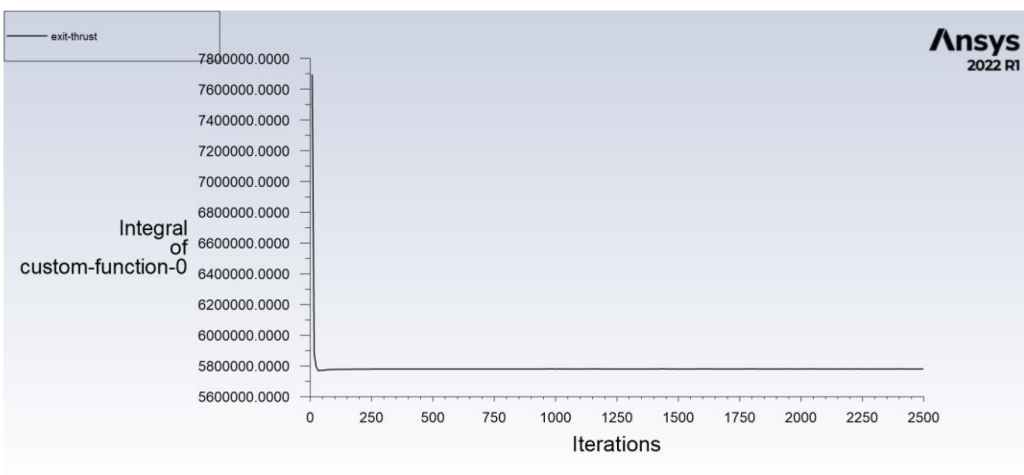

Figure 4.43 – 2.5 % geometry decrease exit thrust calculation per iteration.

5% geometry decrease:

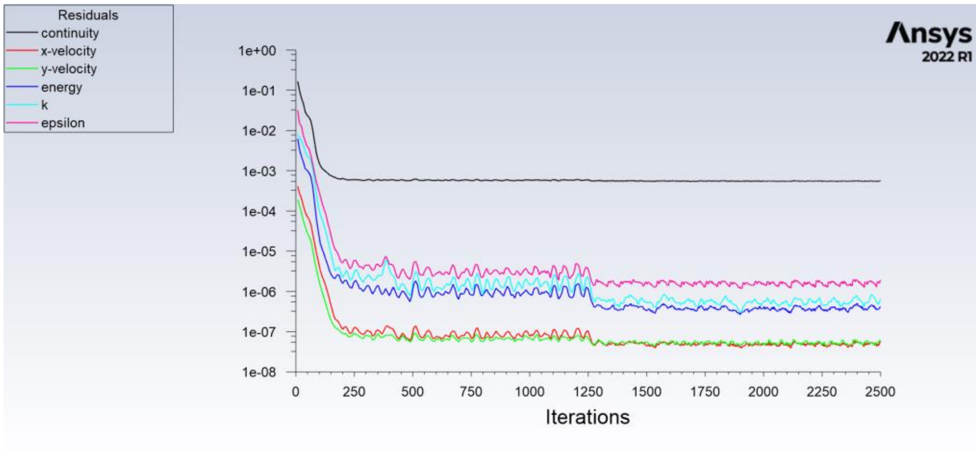

Figure 4.44 – 5% geometry decrease residuals per iteration.

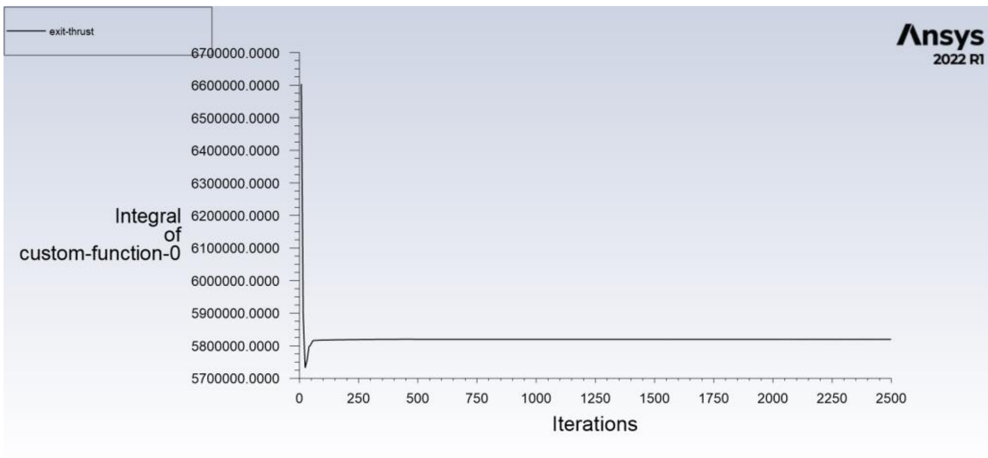

Figure 4.45 – 5% geometry decrease exit thrust calculation per iteration.

10% geometry decrease:

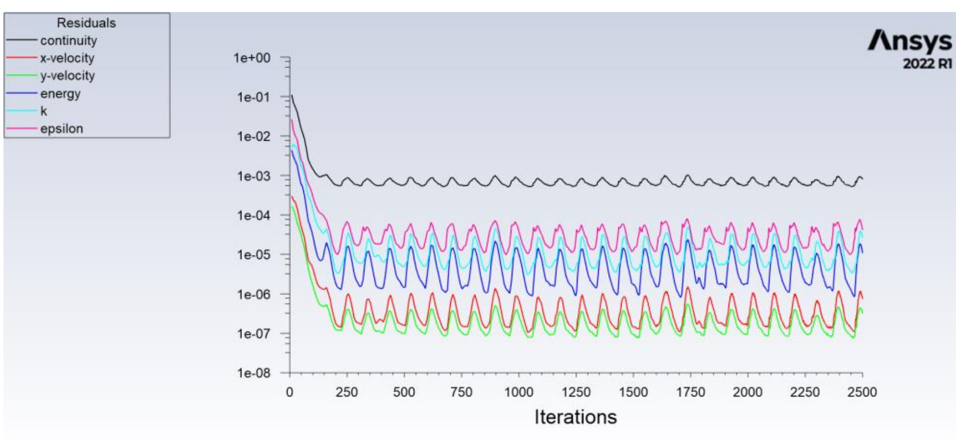

Figure 4.46 – 10% geometry decrease residuals per iteration.

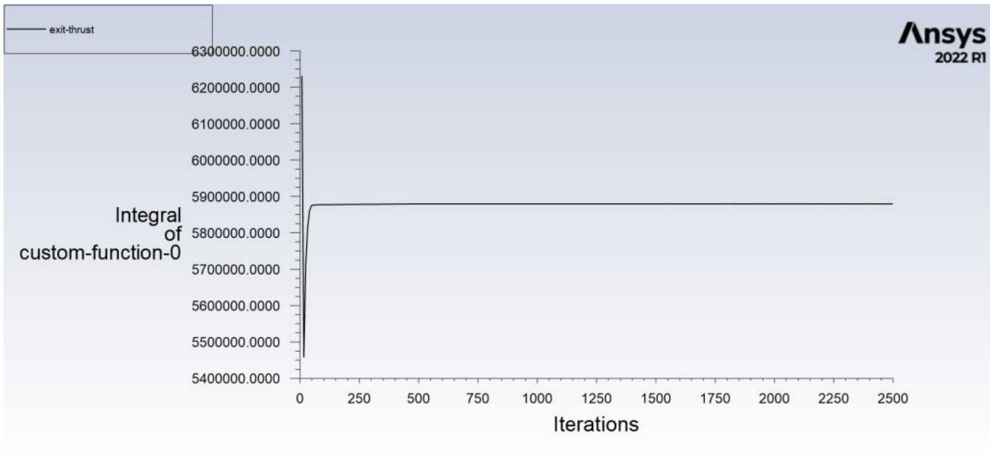

Figure 4.47 – 10% geometry decrease exit thrust calculation per iteration.

10% geometry increase:

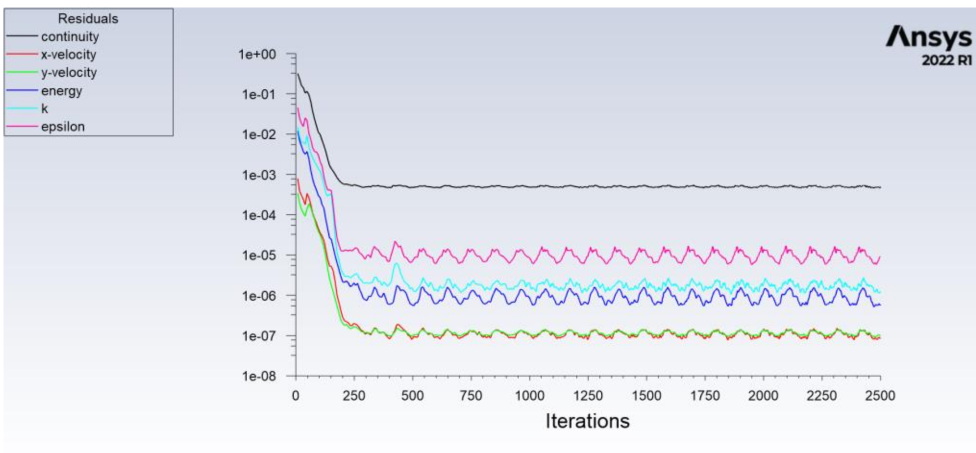

Figure 4.48 – 10% geometry increase residuals per iteration.

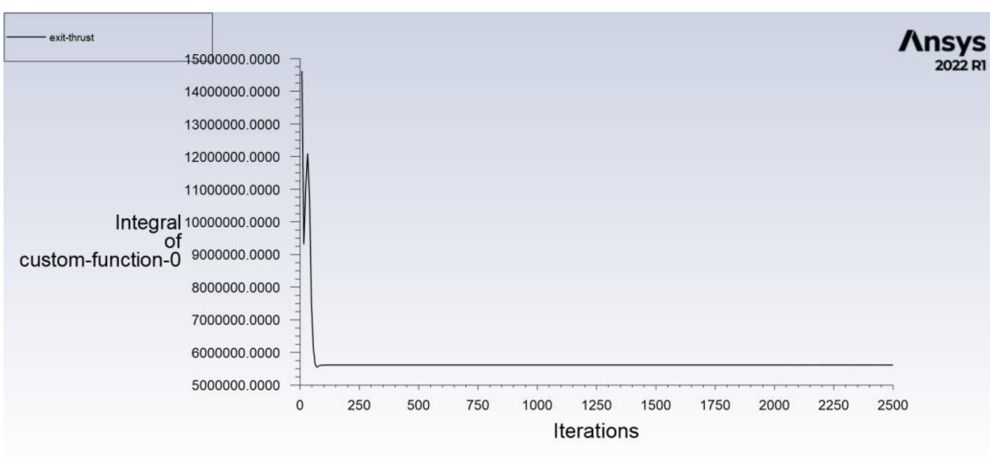

Figure 4.49 – 10% geometry increase exit thrust calculation per iteration.

5% geometry increase:

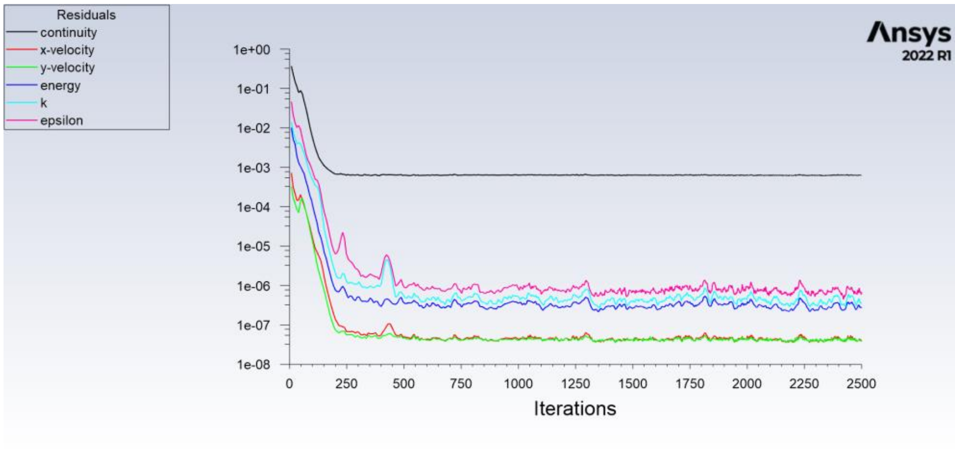

Figure 4.50 – 5% geometry increase residuals per iteration.

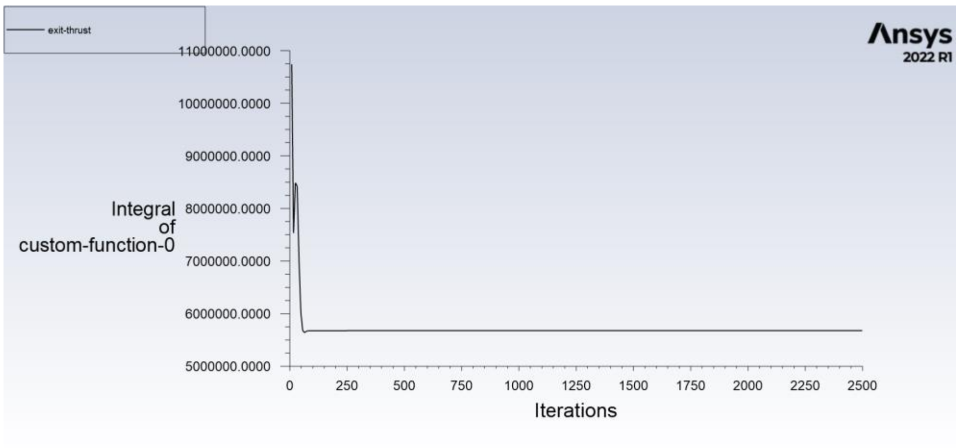

Figure 4.51 – 5% geometry increase exit thrust calculation per iteration.

2.5% geometry increase:

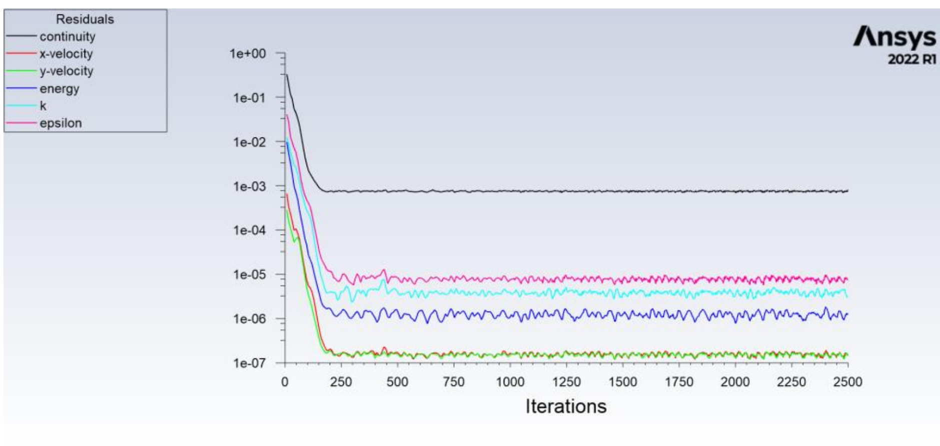

Figure 4.52 – 2.5% geometry increase residuals per iteration.

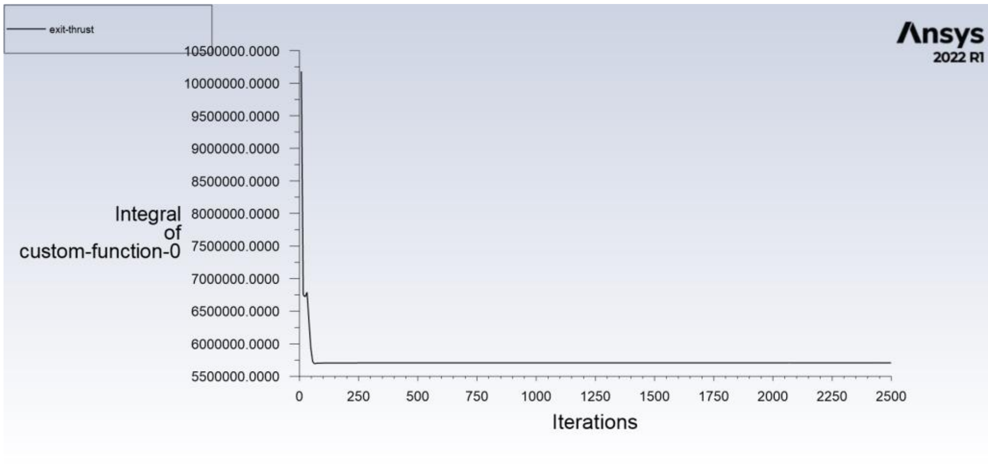

Figure 4.53 – 2.5% geometry increase exit thrust calculation per iteration.

1% geometry increase:

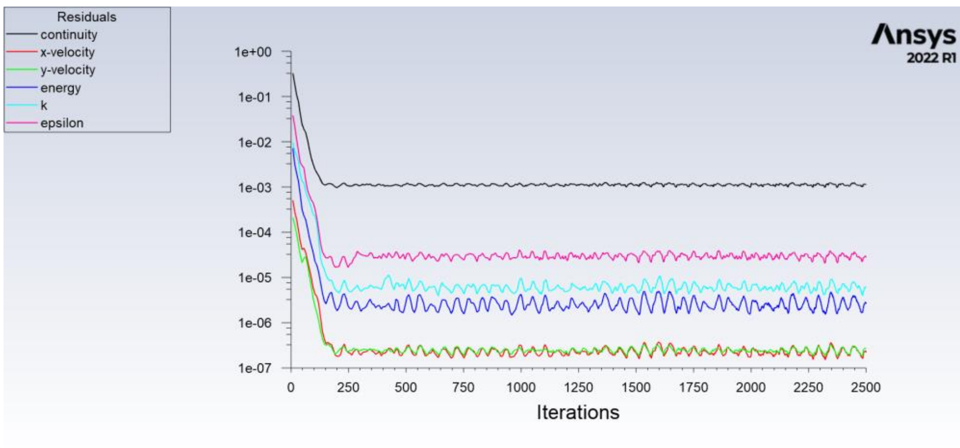

Figure 4.54 – 1% geometry increase residuals per iteration.

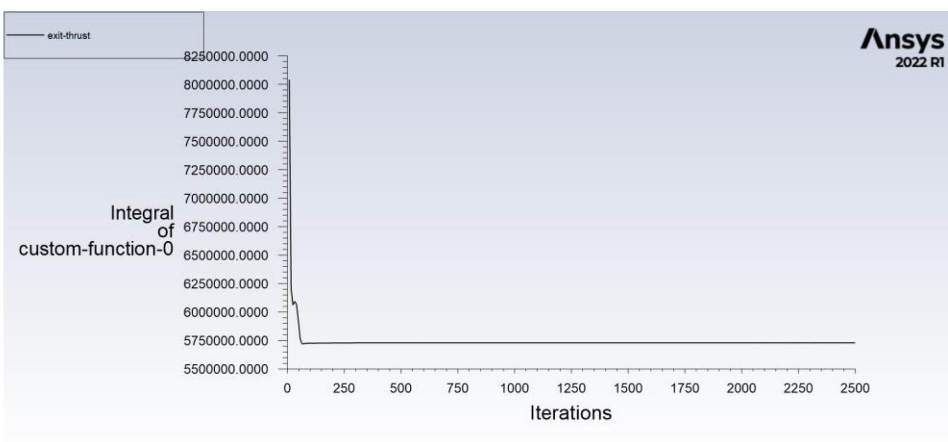

Figure 4.55 – 1% geometry increase exit thrust calculation per iteration.

4.9 Analysis and Discussion

Now before comparing experimental results from CFD to theoretical from the equations, it serves well to discuss the approach leading to this analysis. The geometry used in the CFD came from the contour produced by the method of characteristics. The method of characteristics requires the desired exit Mach number, the method's total number of characteristic points and "kick-off angle" to initiate the algorithmic scheme, and the rocket's parameters of throat radius and fuel specific heat ratio. The parameters of focus in this context are the throat radius and the exit Mach number. The throat radius may be calculated through the published area ratio and exit radius. The Mach number at the exit stems from ideally adapted conditions, when the exit pressure equals the ambient pressure. For this ideal condition, there is also a matching exit area to facilitate the exit pressure and an expected thrust to match. What the CFD analysis will enable is a comparison for how the theoretical thrust relates to reality which incorporates viscous effects. By expanding and contracting the geometry, this analysis may build a relationship tying the method of characteristics theoretical to CFD experimental thrust values at the nozzle exit.

From the surface level, the CFD results for the Saturn V F-1 engine shown in Table 4.5 - Table 4.9 show the highest calculated force corresponds with the largest area in each of the 5 cases. This not only makes intuitive sense, as the larger area allows for a larger amount of mass to flow out and thus produce a higher amount of thrust, but equation 1.1 corroborates this as the thrust generated is a function of the exit area.

The nozzle contour for this procedure is developed based on a set of conditions. These conditions have an associated thrust calculated using the equations, which may be used as a reference point for the experimental results in the CFD models. To compare theory and application, Tables 4.5 – Table 4.9 also show the theoretical thrust for each of the 5 altitudes and the CFD results as the geometry is expanded and contracted for each one. With 9 total cases for each altitude and 5 altitudes, one may compare the percent difference for the 45 cases.

Table 4.5 – CFD to theory results for Mach 3.141.

Percent of Predicted Geometry	CFD Experimental [N]	Theory Calculation [N]	Percent Difference
90	4686938.5	6606138.76	33.99
95	5205385	6606138.76	23.72
97.5	5480034	6606138.76	18.63
99	5637768.5	6606138.76	15.82
1	5750114.5	6606138.76	13.86
101	5861539	6606138.76	11.94
102.5	6035889	6606138.76	9.02
105	6321970.5	6606138.76	4.40
110	6889997	6606138.76	4.21

Table 4.6 – CFD to theory results for Mach 3.21.

Percent of Predicted Geometry	CFD Experimental [N]	Theory Calculation [N]	Percent Difference
90	5181338	6721043.07	25.87
95	5764764	6721043.07	15.32
97.5	6052109	6721043.07	10.47
99	6234213	6721043.07	7.52
1	6357069	6721043.07	5.57
101	6487615.5	6721043.07	3.53
102.5	6671699.5	6721043.07	0.74
105	6978001.5	6721043.07	3.75
110	7627517.5	6721043.07	12.64

Table 4.7 – CFD to theory results for Mach 3.31.

Percent of Predicted Geometry	CFD Experimental [N]	Theory Calculation [N]	Percent Difference
90	5291490	6836487.37	25.48
95	5870011	6836487.37	15.21
97.5	6172490	6836487.37	10.21
99	6364206.5	6836487.37	7.16
1	6490874	6836487.37	5.19
101	6609949	6836487.37	3.37
102.5	6824462.5	6836487.37	0.18
105	7120957	6836487.37	4.08
110	7800460	6836487.37	13.17

Table 4.8 – CFD to theory results for Mach 3.406.

Percent of Predicted Geometry	CFD Experimental [N]	Theory Calculation [N]	Percent Difference
90	5378126	6942924.88	25.40
95	5967965.5	6942924.88	15.10
97.5	6281106	6942924.88	10.01
99	6462588	6942924.88	7.17

1	6598937	6942924.88	5.08
101	6731118	6942924.88	3.10
102.5	6921205.5	6942924.88	0.31
105	7252993.5	6942924.88	4.37
110	7923452	6942924.88	13.19

Table 4.9 – CFD to theory results for Mach 3.497.

Percent of Predicted Geometry	CFD Experimental [N]	Theory Calculation [N]	Percent Difference
90	5439767.5	7039835.75	25.64
95	6028318	7039835.75	15.48
97.5	6353171	7039835.75	10.25
99	6537401.5	7039835.75	7.40
1	6675140.5	7039835.75	5.32
101	6797466.5	7039835.75	3.50
102.5	6986329.5	7039835.75	0.76
105	7319303	7039835.75	3.89
110	8017461	7039835.75	12.99

Now to examine the effect of the expansion coefficients (i.e., percent of the predicted geometry), Table 4.10 and Figure 4.56 highlight each study's expansion coefficient with the smallest percent difference from theoretical calculations. From these 5 studies, there is an indication that one may expand the rocket nozzle to account for viscous effects in the contours produced by the inviscid-assuming method of characteristics.

Table 4.10 – Cases with lowest percent difference

Study	Mach Number	Expansion Coefficient Case with Lowest Percent Difference
1	3.1411	1.1
2	3.21	1.025
3	3.31	1.025
4	3.406	1.025
5	3.497	1.025

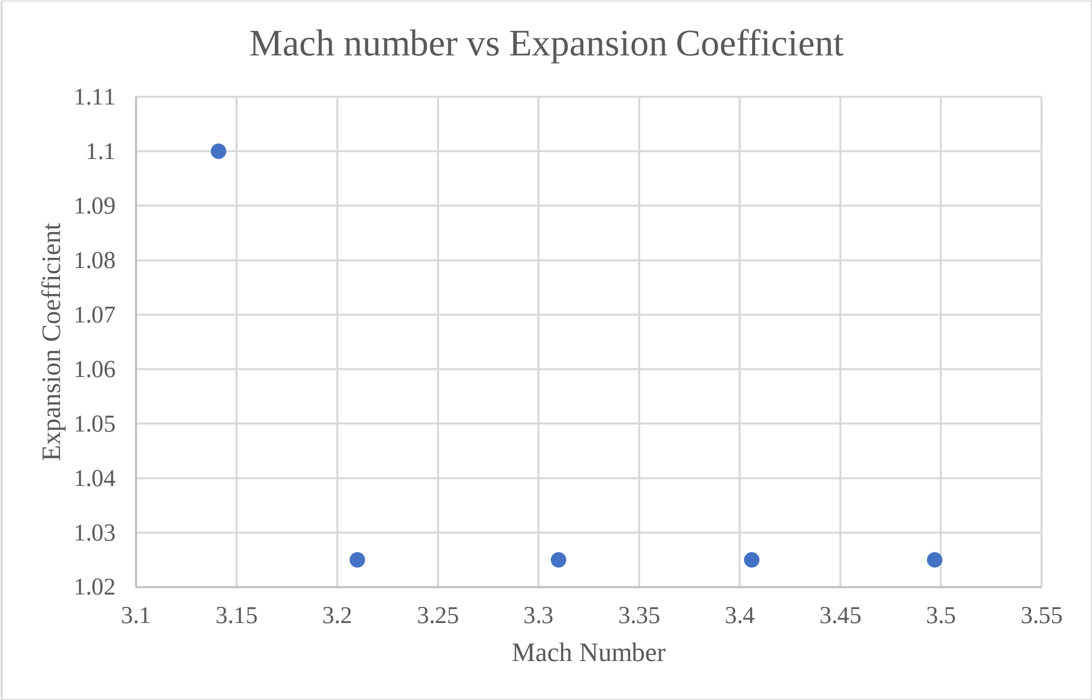

Figure 4.56 – Mach number vs expansion coefficient case with lowest percent difference.

4.10 Limitations

These cases, all which were ran in steady state as previously described, successfully converged and produced results in the realm of expectations. This report also had initially aimed to run additional ones for the same Saturn V F-1 engine, however the CFD simulations failed to produce results. The simulation for higher Mach numbers began to diverge or immediately result in a floating-point exception with extremely high thrusts as the solution by result of failure to converge.

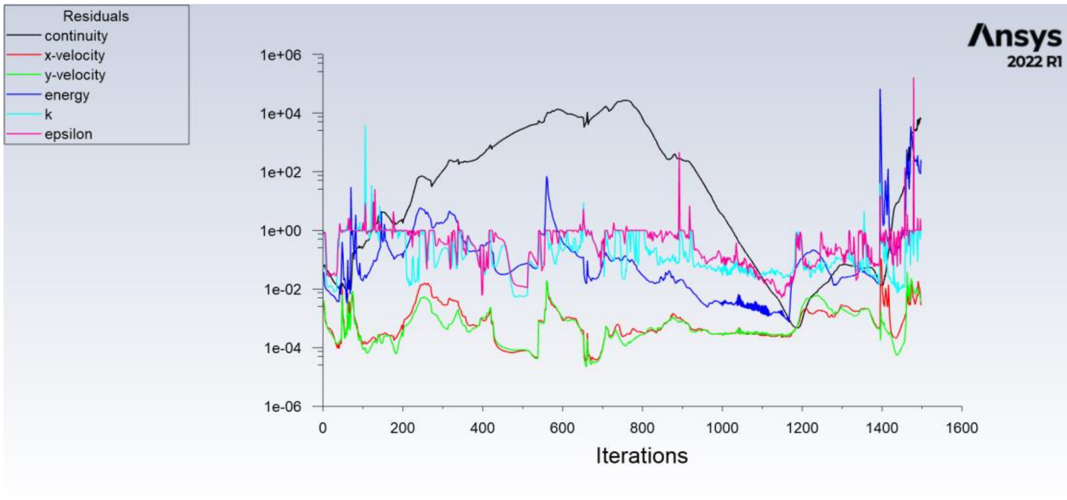

Figure 4.57 – Residuals observed for a case with expected exit Mach number of 4.001.

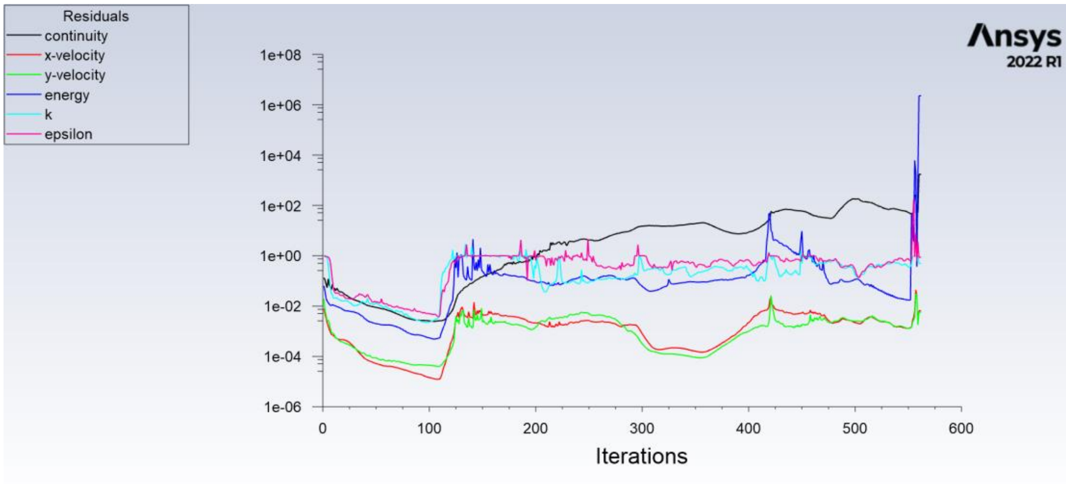

Figure 4.58 – Residuals observed for a case with expected exit Mach number of 3.849.

Figure 4.59 – Observed flow fields for a case with exit Mach number of 4.001.

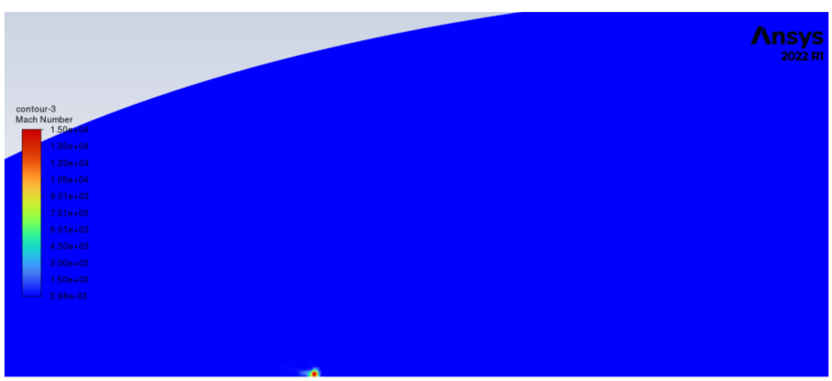

Figure 4.60 – Observed flow fields for a case with exit Mach number of 3.849.

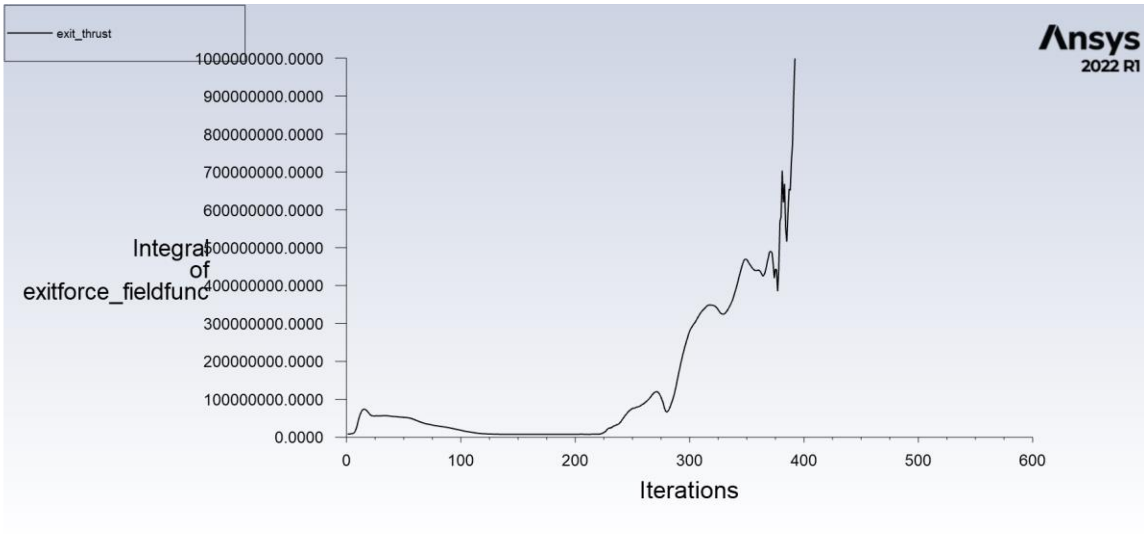

Figure 4.61 – Observed thrust calculations for a case with exit Mach number of 3.849.

The cause is in these failed simulations is typically linked with poor initialization schemes. Although all studies initialized using the conditions at the inlet, the solver appears to prove unsuccessful in reaching a solution at higher Mach numbers and larger nozzles. A small error in the solver may continue to propagate, only expanding in value and cell count with each passing iteration. Because of this limitation for the simulation's input parameters, it will prove worthwhile to perform a secondary parametric study.

This report will use the findings from this first parametric study to continue the research for what role Mach numbers and rocket settings have on the relationship proposed in this chapter. In the following chapter, this paper will continue to gather data for this relationship.

Chapter 5 Analysis of Method of Characteristics

5.1 Overview and Approach

As shown in the previous chapter, performing a CFD analysis for a rocket contour produced from the method of characteristics produces lower than expected results. The continuation of this topic leads to the question of how to relate the contours from the method of characteristics to reality. What modifications need to be made so that the experimental results match theoretical? This chapter will continue this research.

The study performed in the previous chapter revolved entirely on the Saturn V's F-1 engine. This entailed the same chamber pressure, chamber temperature, and fuel specific heat ratio. For the sake of capturing a greater extent of problem parameters, this chapter will perform a similar experiment on 4 different rocket engine nozzles with varying conditions. The focus will revolve around the desired exit Mach number, but the conditions at the chamber will be incorporated in the CFD as well as the equations.

This parametric study aims to determine whether a potential relationship between inviscid method of characteristics to viscous CFD has any dependency on the input parameters listed above. By varying the nozzle geometry alongside the varying inputs, one may observe any potential variation of the expansion coefficient.

5.2 Methodology

The J-2 engine, Merlin-1C, RS-25, and Vulcain will serve as case studies to examine for the parametric sweep of this section. The four engines all have different chamber conditions, area ratios, mixture ratios, and many more characteristics[28–31]. These differences offer an opportunity to observe the translation from theory to application and any potential relation between the two. Aside from engine characteristics, these four engines span generations of application. The J-2, used in the Saturn V missions in the 1960s, the RS-25 in the 80s, the European Space Agency's Vulcain engine in Ariane 5 series launches in the 90s to 2000s, and most recently the Merlin engines seen in SpaceX's Falcon 9.

Table 5.1 – Studied engine specifications[28–31].

Engine	Chamber Pressure [bar]	Exit Diameter [m]	Area Ratio	O:F Mixture Ratio	Oxidizer	Fuel
J-2	30	2.01	28	5.5	LOX	LH2
RS-25	206.4	2.4384	69	6	LOX	LH2
Vulcain	109	1.76	45.1	5.9	LOX	LH2
Merlin 1C	67.7065	1.43256	14.5	2.2	LOX	RP-1

For all four engines, this section will first derive the parameters used in the method of characteristics. This will involve utilizing NASA's Chemical Equilibrium with Applications tool to determine the specific heat ratio, exit pressure, exit temperature, and chamber temperature[32]. Tabulated in Table 5.1, these findings will be used later in isentropic equations from chapter 1 to calculate both ideal and non-ideal engine characteristics. This will involve rocket performance parameters like the thrust, coefficient of thrust, and I_{sp}, but also aspects like the Mach number and exit area.

Table 5.2 – NASA CEA tool results[32].

Engine	Gamma	Exit Pressure [bar]	Exit Temperature [K]	Chamber Temperature [K]
J-2	1.2468	0.09976	1417	3318
RS-25	1.2540	0.21397	1233	3599
Vulcain	1.2459	0.19772	1356	3517
Merlin 1C	1.2254	0.52014	1666	3511

With the rest of the engine characteristics computed, this report will once more use the method of characteristics algorithm to calculate an ideal contour given the throat radius and desired exit Mach number. With the contour created from the theoretical calculations, the experimental data will be next in the form of CFD. As done with the F-1 engine, this study will expand and contract the vertical dimensions by 1, 2.5, 5, and 10% for the developed contours to see which of these coefficients of expansion represents a relation between theory and application.

For the Ansys Fluent model, this report will utilize the same CFD physics settings, meshing modes, and parametrization techniques for simplicity's sake. A main difference in the Ansys Fluent model will involve applying different boundary conditions to effectively capture the different engine's chamber settings. The parametrization mode will be reused to efficiently run through each of the 9 cases for the 4 engines, producing a total of 36 CFD simulations.

With the experimental data collected and the theoretical values calculated, the next steps from there would consist of an attempt to observe a relationship between Mach number, chamber settings, and other engine specifications.

5.3 Theoretical Results

Applying the equations discussed in earlier chapters produces the results tabulated in Table 5.3 for the nonideal and ideal cases. Nonideal, of course, meaning when the exit pressure does not equal the ambient pressure and ideal when it does. As expected, when there is no back pressure at the exit, the generated thrust increases under the ideal conditions. This in turn results in an increase in specific impulse.

Table 5.3 – Calculated non-ideal (actual) conditions, $p_e \neq p_a$.

Engine	Thrust [N]	Isp [s]	Exit Area [m^2]	Exit Mach Number
J-2	294653	134.84	3.17	4.12
RS-25	2133909	245.51	4.67	4.88
Vulcain	839923	227.79	2.43	4.49
Merlin 1C	1167863	149.35	1.61	3.58

Table 5.4 – Calculated ideal conditions, p_e=p_a.

Engine	Thrust [N]	Isp [s]	Exit Area [m^2]	Exit Mach Number
J-2	496645	227.28	0.61	2.78
RS-25	2348591	270.21	1.41	3.90
Vulcain	955193	259.05	0.72	3.51
Merlin 1C	1189842	152.16	1.11	3.22

These findings may then be used in the method of characteristics. For each of the four engines, the ideal Mach number at the exit and the actual throat radius will work as inputs to produce a contour as the output in the form of a .csv file as before. Applying the 9 expansion coefficients to these vertical coordinates produces the 36 total cases for the four engines when including the original contour as well. From here, the next step is CFD.

5.4 CFD Results

For the sake of brevity, this report will highlight images only from one of the engines. In this case, the focus will revolve around the RS-25 engine and the respective expansions and contractions in geometry. Shown below are the flow fields encapsulating the speed, static temperature, and static pressure as contour plots.

90% of original contour results:

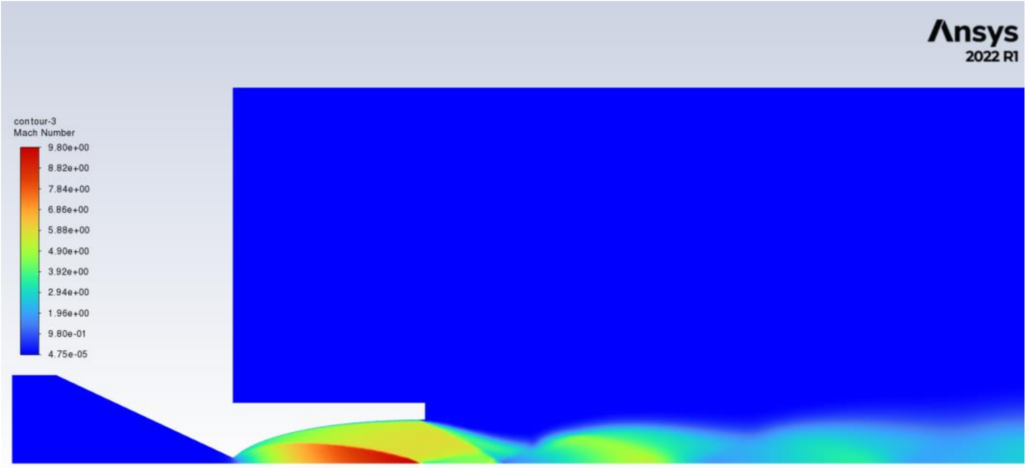

Figure 5.1 – 90% of original geometry Mach number contour.

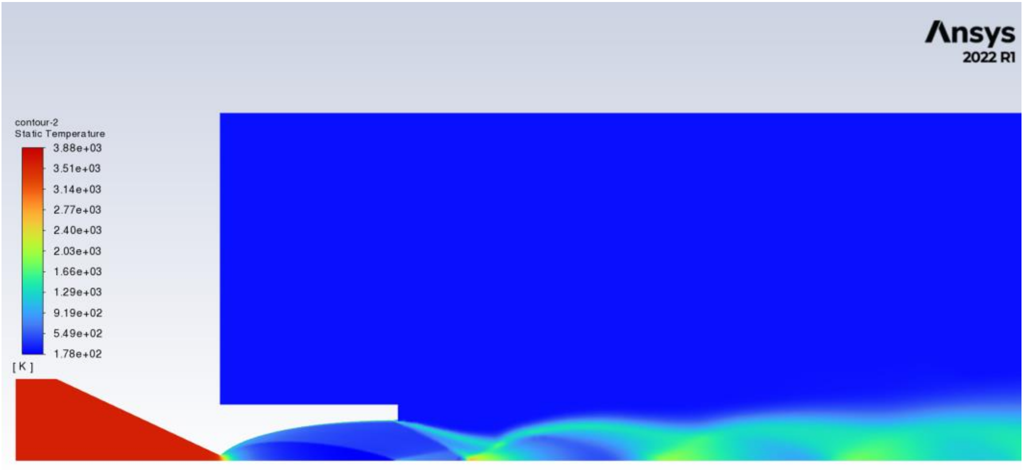

Figure 5.2 – 90% of original geometry static temperature contour.

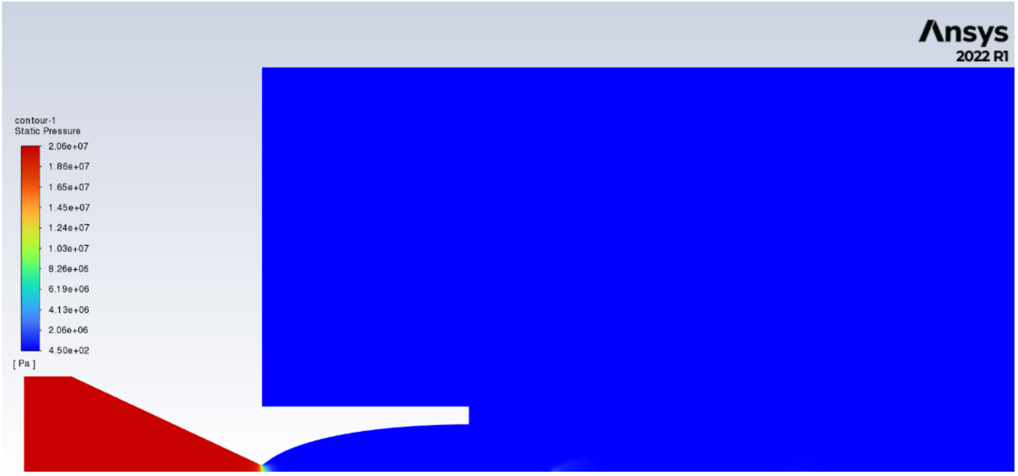

Figure 5.3 – 90% of original geometry static pressure contour.

95% of original contour results:

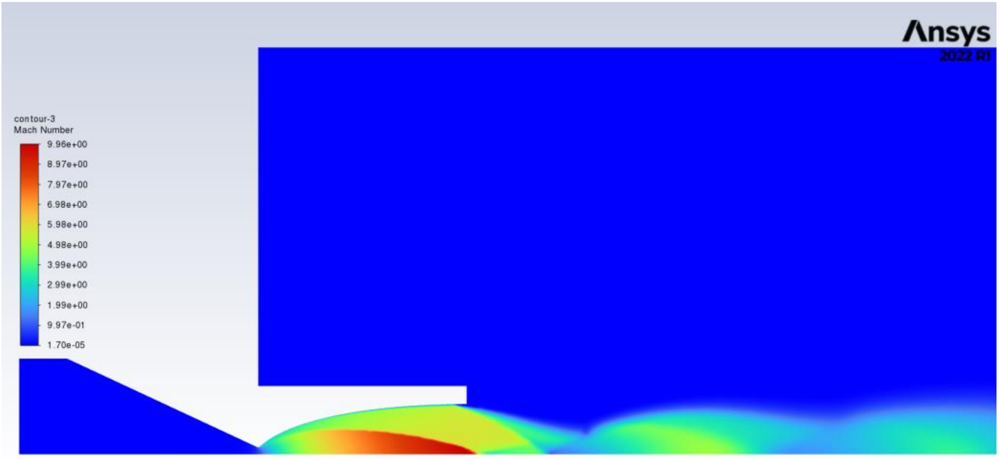

Figure 5.4 – 95% of original geometry Mach number contour.

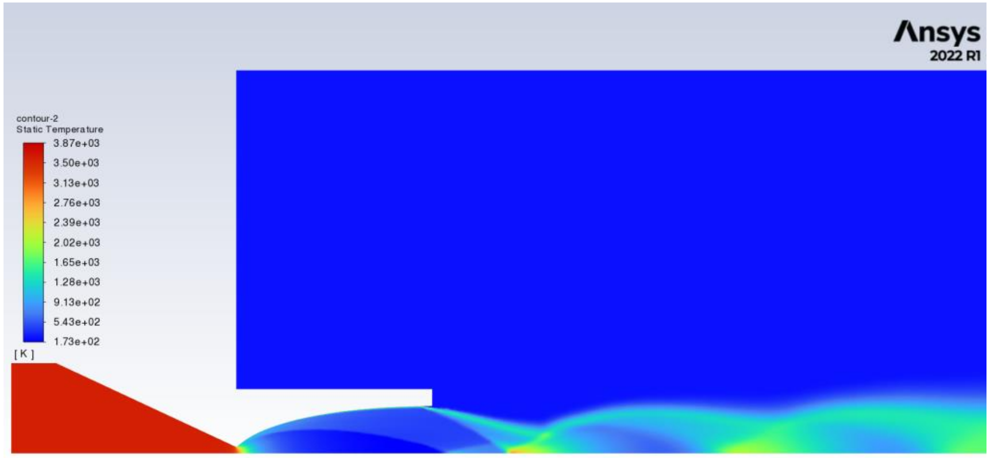

Figure 5.5 – 95% of original geometry static temperature contour.

Figure 5.6 – 95% of original geometry static pressure contour.

97.5% of original contour results:

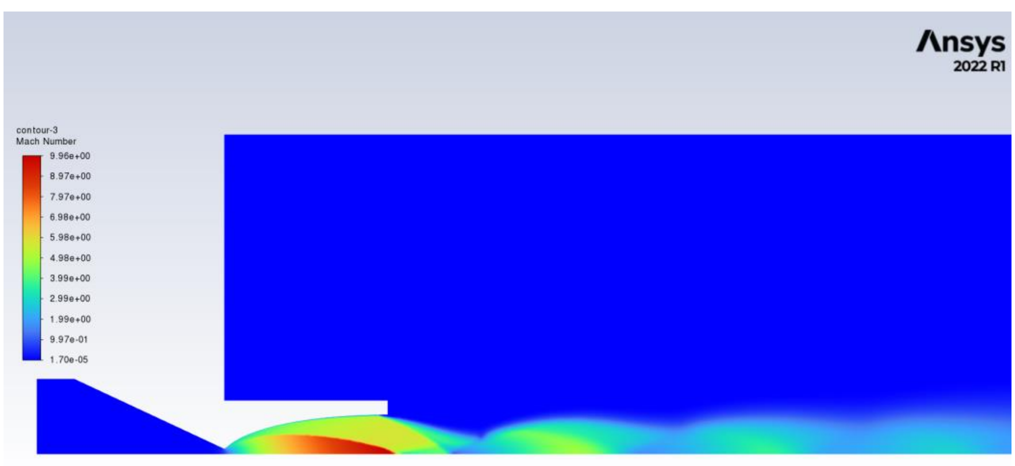

Figure 5.7 – 92.5% of original geometry Mach number contour.

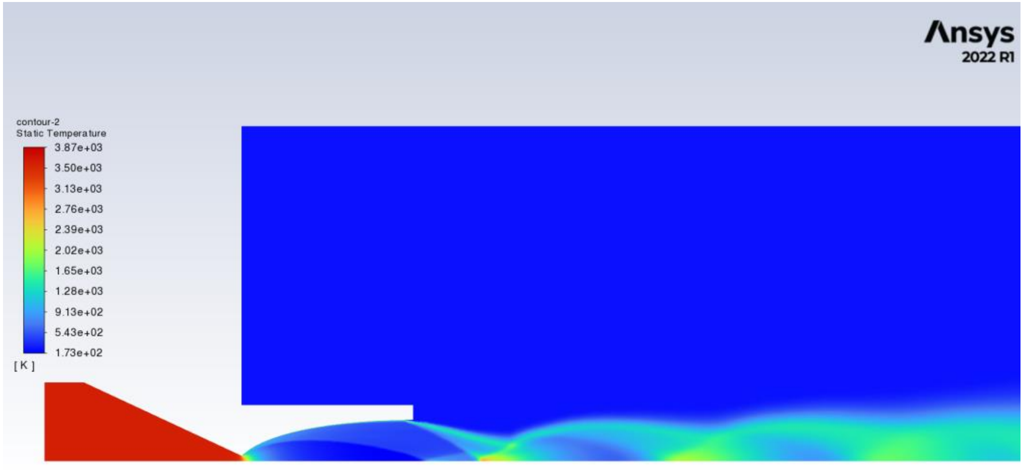

Figure 5.8 – 97.5% of original geometry static temperature contour.

Figure 5.9 – 97.5% of original geometry static pressure contour.

99% of original contour results:

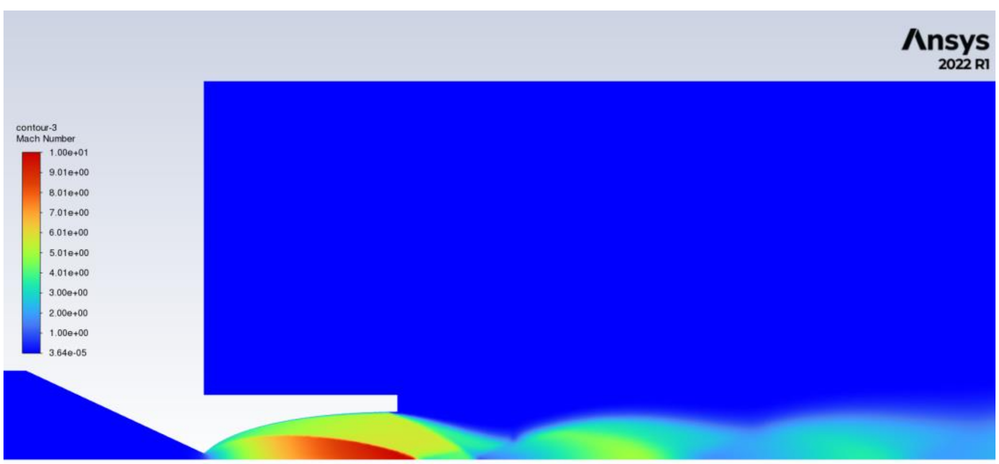

Figure 5.10 – 99% of original geometry Mach number contour.

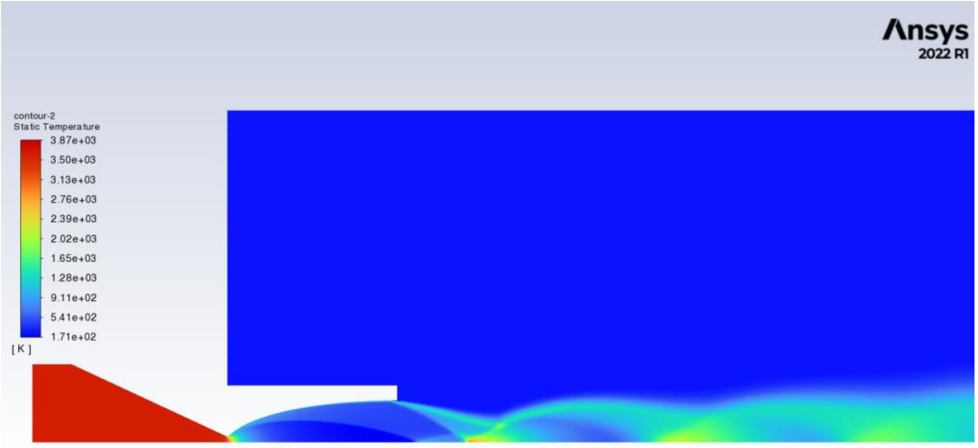

Figure 5.11 – 99% of original geometry static temperature contour.

Figure 5.12 – 99% of original geometry static pressure contour.

100% of original contour results:

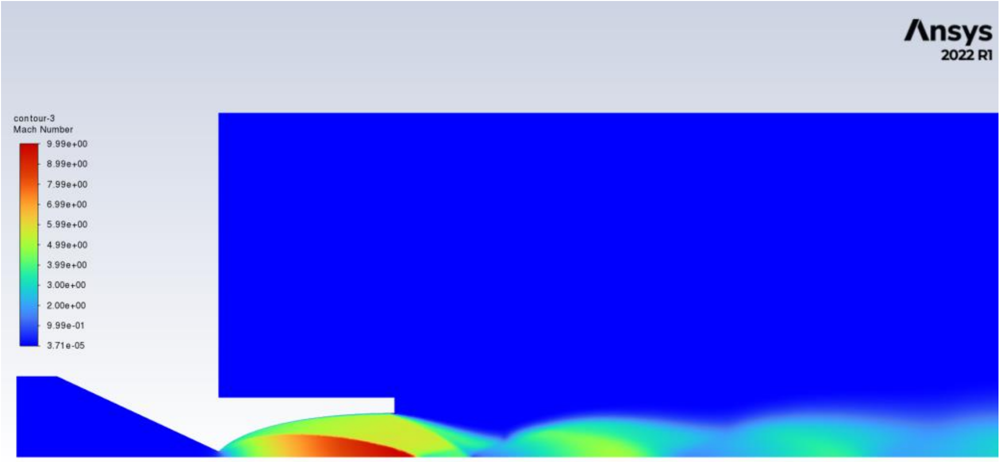

Figure 5.13 – 100% of original geometry Mach number contour.

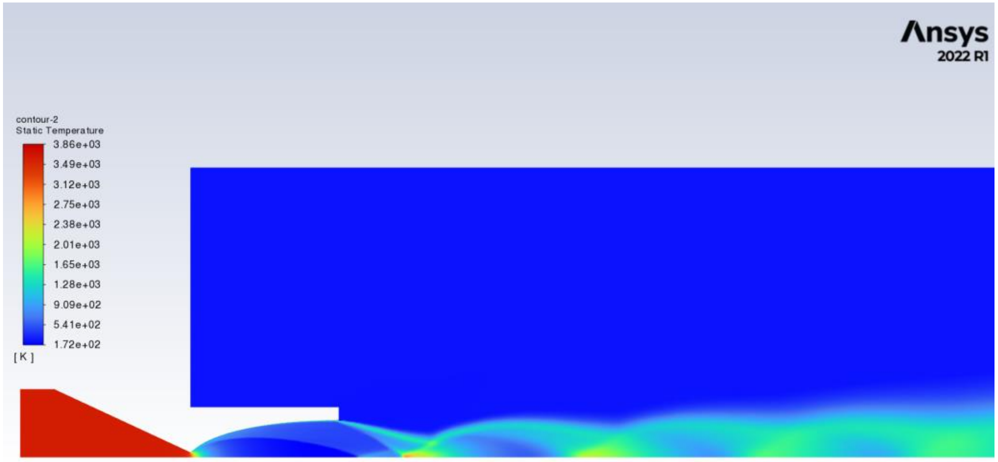

Figure 5.14 – 100% of original geometry static temperature contour.

Figure 5.15 – 100% of original geometry static pressure contour.

101% of original contour results:

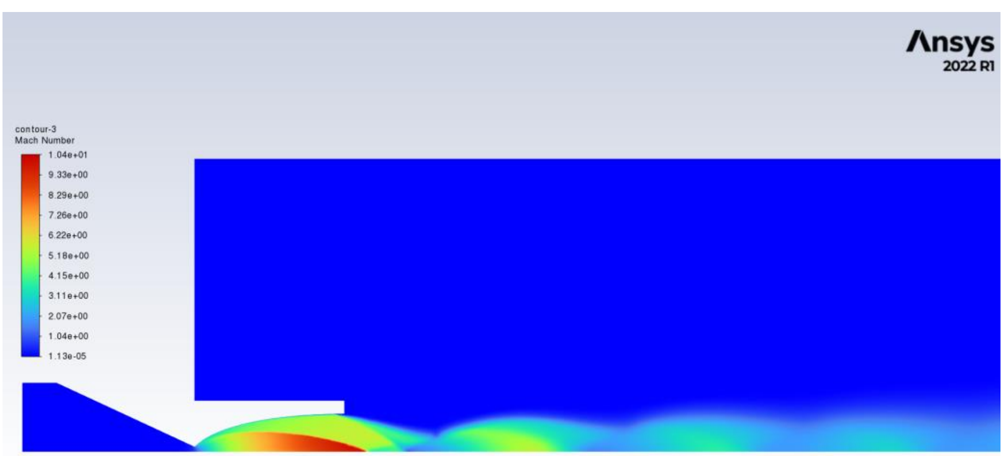

Figure 5.16 – 101% of original geometry Mach number contour.

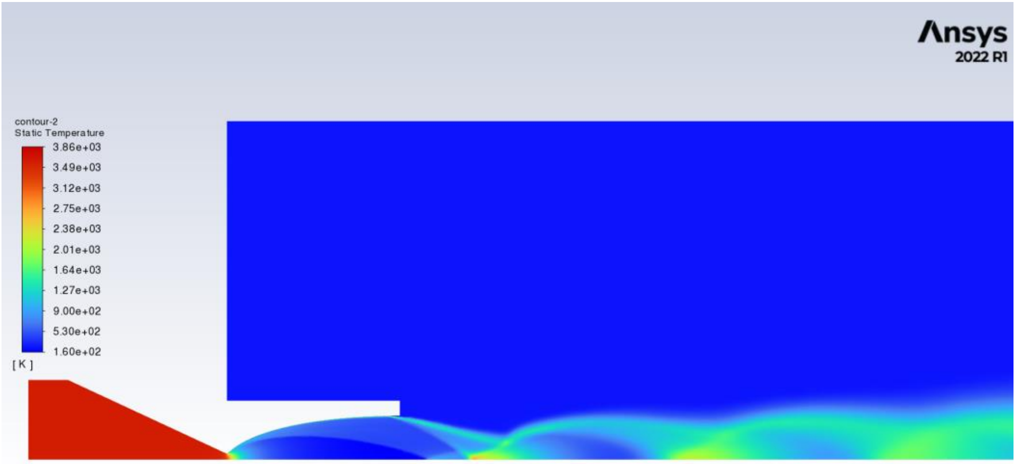

Figure 5.17 – 101% of original geometry static temperature contour.

Figure 5.18 – 101% of original geometry static pressure contour.

102.5% of original contour results:

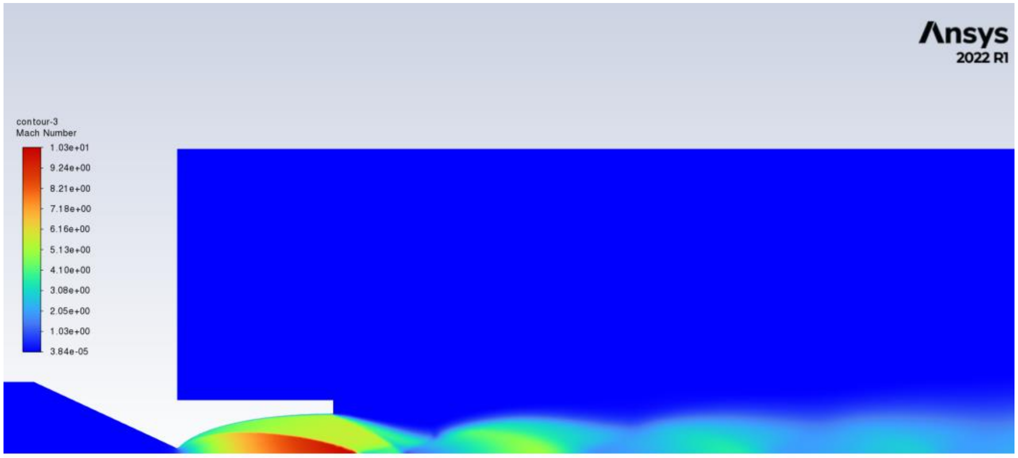

Figure 5.19 – 102.5% of original geometry Mach number contour.

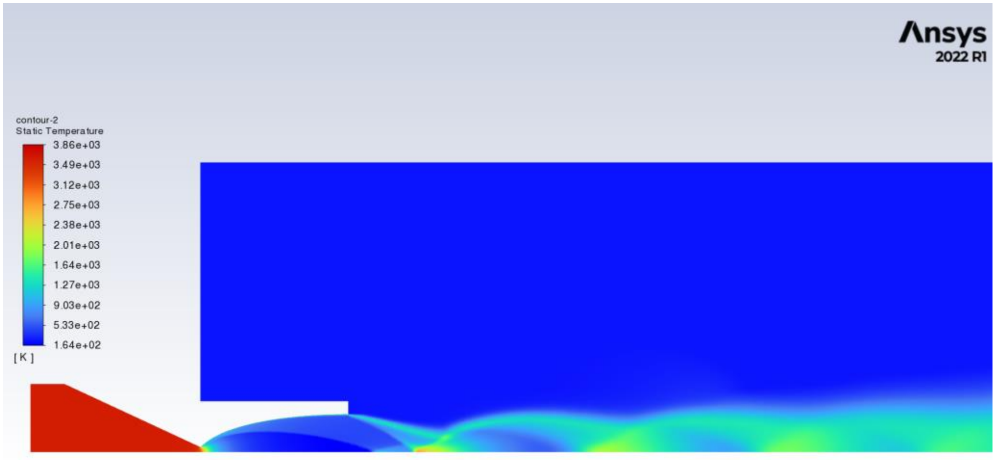

Figure 5.20 – 102.5% of original geometry static temperature contour.

Figure 5.21 – 102.5% of original geometry static pressure contour.

105% of original contour results:

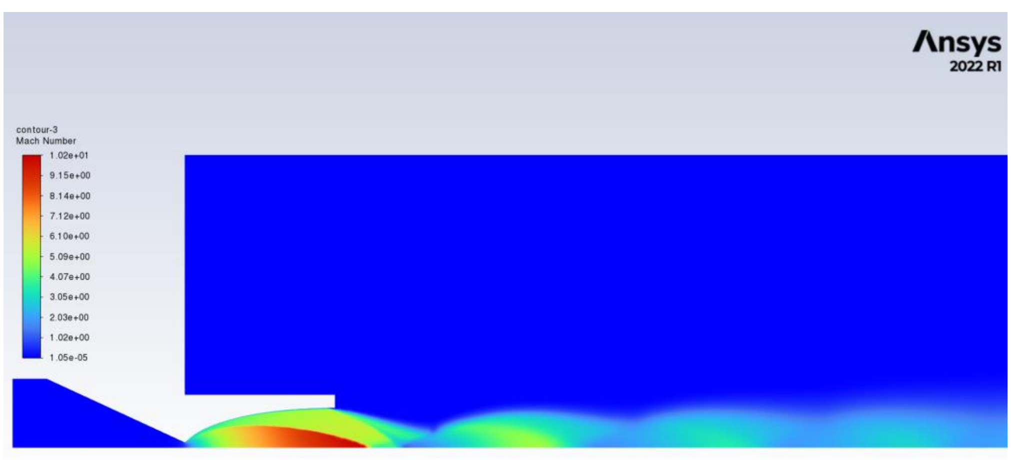

Figure 5.22 – 105% of original geometry Mach number contour.

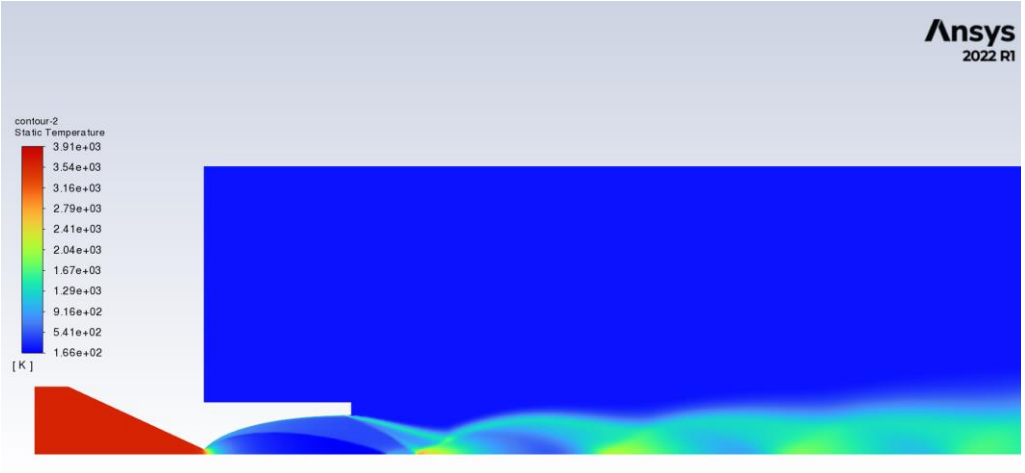

Figure 5.23 – 105% of original geometry static temperature contour.

Figure 5.24 – 105% of original geometry static pressure contour.

110% of original contour results:

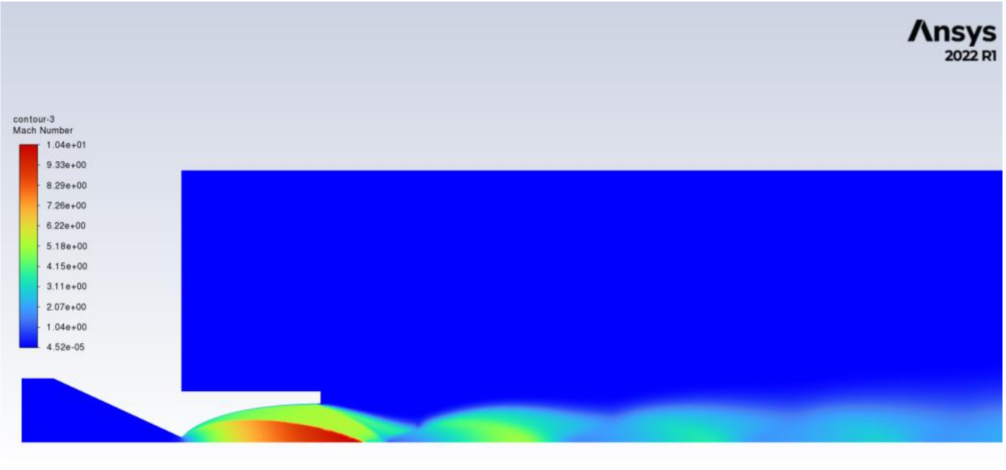

Figure 5.25 – 110% of original geometry Mach number contour.

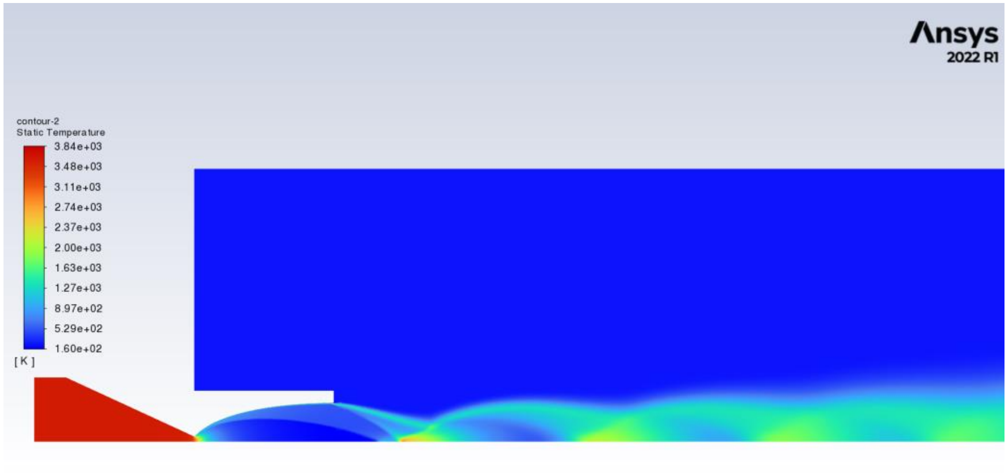

Figure 5.26 – 110% of original geometry static temperature contour.

Figure 5.27 – 110% of original geometry static pressure contour.

The final force calculated using the same equation in the Saturn V case study, the CFD produced the experimental values this report will use to compare to the theoretical.

Table 5.5 – CFD thrust results for 4 engines with no expansion or contractions.

Engine	Analytical Mach Number	100%
J-2	2.78	466004
Merlin	3.22	1090648
Vulcain	3.51	906499
RS-25	3.90	2249902

Table 5.6 – CFD thrust results for 4 engines with indicated expansions.

Engine	Analytical Mach Number	110%	105%	102.5%	101%
J-2	2.78	561055	513513	491768	476011
Merlin	3.22	1306130	1199176	1142984	1113916
Vulcain	3.51	1084750	993758	944143	925011
RS-25	3.90	2662712	2405944	2313309	2241853

Table 5.7 – CFD thrust results for 4 engines with indicated contractions.

Engine	Analytical Mach Number	99%	97.5%	95%	90%
J-2	2.78	459791	445634	421685	384511
Merlin	3.22	1069483	1038106	987953	890069
Vulcain	3.51	885678	860691	822367	734928
RS-25	3.90	2168172	2076451	1969644	1787794

5.5 CFD Validation

Validation of the results from the simulations may take shape as it did in the previous case study: the residual and force calculation plots over the full iteration count. Both the residual and calculation plots per iteration showed oscillatory behavior, cycling over the course of the iteration count. This behavior also occurred in the previous chapter for the F-1 engine. The root cause was not researched in this report but may be related to any number of factors – the numerical scheme selected, the solver settings in Ansys, the meshing, or perhaps this may even be an expected physical phenomenon. However, considering this behavior occurred in all the engines studied but with different amplitudes, it may be rooted in the physics but amplified by the meshing type.

Given that the calculations converged to a single value, experienced what appears to be a numerical error, then corrected this error, this report will assert the calculations may be trusted. To avoid leaning towards error, the force values at the valleys of these calculation plots will be selected in the analysis.

90% of original contour results:

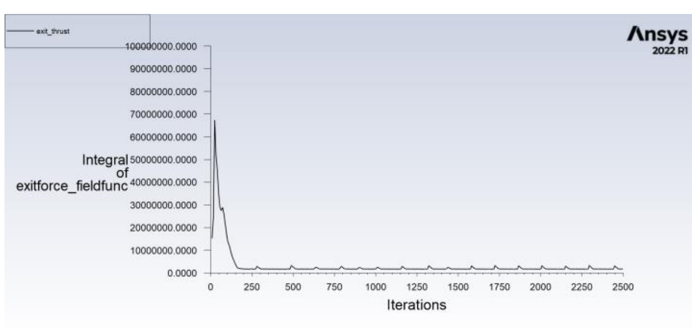

Figure 5.28 – 90% of original geometry force calculation per iteration.

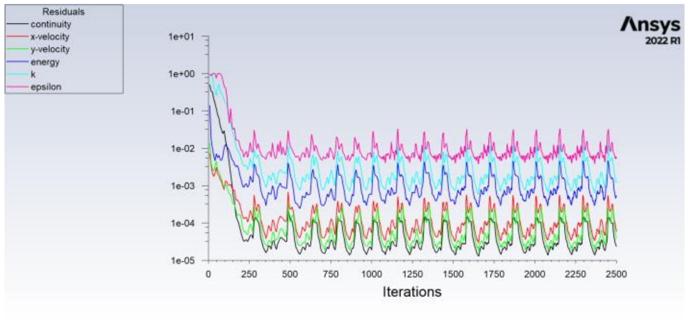

Figure 5.29 – 90% of original geometry residuals per iteration.

110% of original contour results:

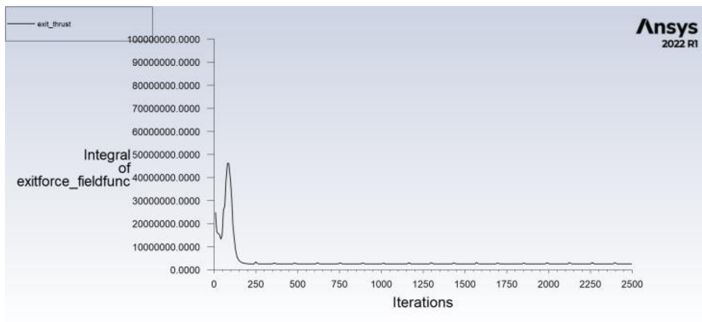

Figure 5.30 – 110% of original geometry force calculation per iteration.

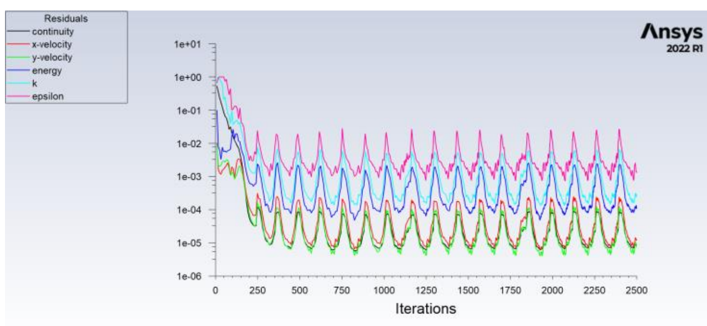

Figure 5.31 – 110% of original geometry residuals per iteration.

5.6 Analysis and Discussion

The highest observed Mach number had very little variation. For the RS-25 in this example, nearly all were observed around Mach 10 at some point along the center line. The variation comes at what point on the centerline inside of the inner most shock wave. The location appears as a function of the exit diameter. The smaller the exit diameter, the shock wave occurs converges to the center line closer to the throat. With the highest expansion ratio, the shock waves and expansion fans lead the flow to have the highest Mach number downstream with the inner most shock wave occurring just a little outside of the nozzle. The effect of the expansion coefficient on these shock waves is greatly apparent when plotting the Mach number at each point throughout the exit diameter for the lowest expansion coefficient and the highest expansion coefficient.

Evident from both the plots and Mach number contours shown in the result section, the shock wave does not occur near the exit for the small expansion ratio but can be seen throughout for the large expansion ratio.

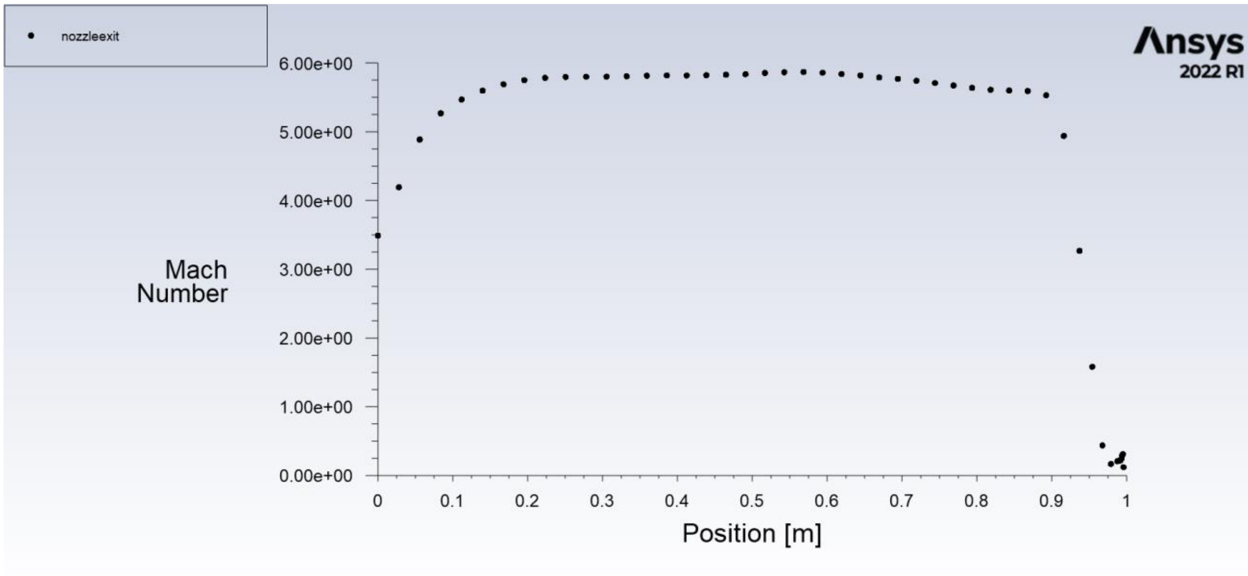

Figure 5.32 – 90% of original geometry – Mach number vs position at the exit diameter.

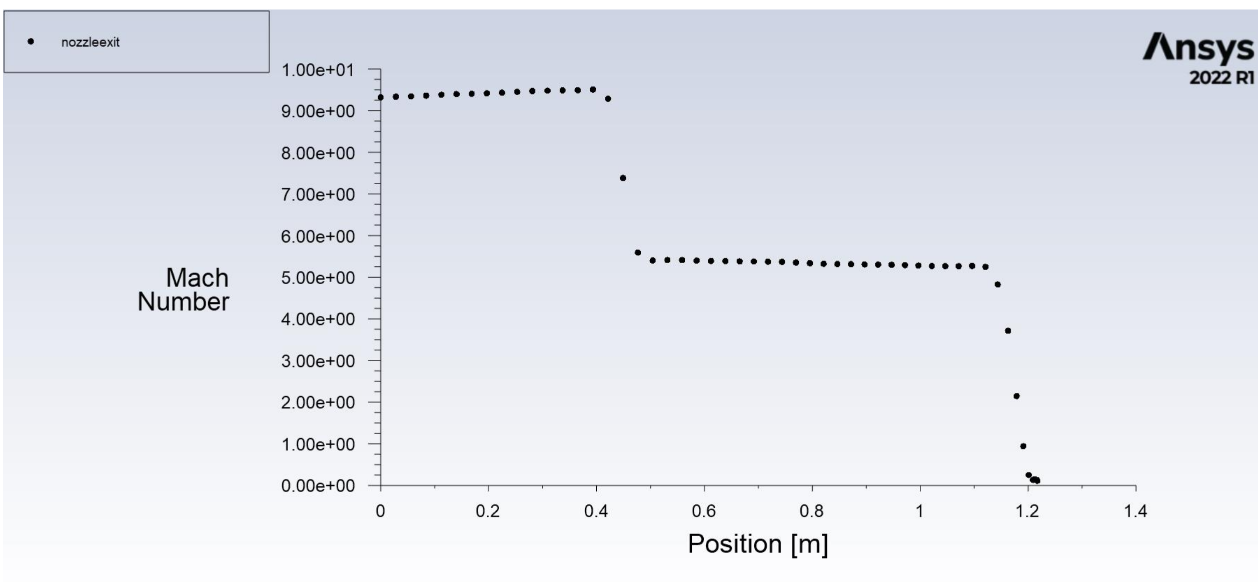

Figure 5.33 – 110% of original geometry – Mach number vs position at the exit diameter.

These same shock waves are observed in the static temperature flow fields contours as well. The chamber temperature holds until the throat, with the heat dissipating as a result of the high velocity. This same temperature reoccurs in decreasing magnitude at the center line as the shock waves converge.

The static pressure in all of the cases remained near the chamber pressure up until the throat, as seen in the RS-25 sampled images. The pressure remains high in the converging section but releases at the diverging section as the velocity ramps up. By the exit, the pressure contours indicate the exit pressure is equal to the ambient pressure.

The force results from this study encompassing the four engines follow a pattern like the results for the F-1 engine studied previously. Seen below, the highest forces for each engine's parametric study are associated with the largest expansion. This once again matches the expectations as the thrust equation is a function of the exit area. The percent difference between the theoretical calculation and CFD result for each of the expansion coefficients indicates which simulation's solution best correlates to theory.

Table 5.8 – CFD to Theory Results for J-2 Engine.

Percent of Predicted Geometry	CFD Experimental [N]	Calculated Theoretical [N]	Percent Difference
0.9	384511	496653	25.45
0.95	421685	496652	16.33
0.975	445634	496651	10.83
0.99	459791	496650	7.71
1	466004	496649	6.37
1.01	476011	496648	4.24
1.025	491768	496647	0.99
1.05	513513	496646	3.34
1.1	561055	496645	12.18

Table 5.9 – CFD to Theory Results for Merline 1C Engine.

Percent of Predicted Geometry	CFD Experimental [N]	Calculated Theoretical [N]	Percent Difference
0.9	890069	1189842	28.83
0.95	987953	1189842	18.54
0.975	1038106	1189842	13.62
0.99	1069483	1189842	10.65
1	1090648	1189842	8.70
1.01	1113916	1189842	6.59
1.025	1142984	1189842	4.02
1.05	1199176	1189842	0.78
1.1	1306130	1189842	9.32

Table 5.10 – CFD to Theory Results for Vulcain Engine.

Percent of Predicted Geometry	CFD Experimental [N]	Calculated Theoretical [N]	Percent Difference
0.9	734928	955193	26.06
0.95	822367	955193	14.94
0.975	860691	955193	10.41
0.99	885678	955193	7.55
1	906499	955193	5.23
1.01	925011	955193	3.21
1.025	944143	955193	1.16
1.05	993758	955193	3.96
1.1	1084750	955193	12.70

Table 5.11 – CFD to Theory Results for RS-25 Engine.

Percent of Predicted Geometry	CFD Experimental [N]	Calculated Theoretical [N]	Percent Difference
0.9	1787794	2348591	27.12
0.95	1969644	2348591	17.55
0.975	2076451	2348591	12.30
0.99	2168172	2348591	7.99
1	2249902	2348591	4.29
1.01	2241853	2348591	4.65
1.025	2313309	2348591	1.51
1.05	2405944	2348591	2.41
1.1	2662712	2348591	12.54

For three out of the four engines studied, the expansion coefficient which produces a nozzle contour generating a thrust closest to theory is 1.025. The Merlin 1C is the only engine with a different expansion coefficient and it is at 1.05. In any case, the original nozzle contour developed to generate the theoretical force continuously underperformed and produced an experimental thrust below expectations. The expansion coefficient then, acted as a *correction factor* to account for viscous effects and produced a nozzle which matched theory.

Table 5.12 – Cases with lowest percent difference.

Studied Engine	Analytical Mach Number	Expansion Coefficient Case with Lowest Percent Difference
J-2	2.78076	1.025
Merlin 1C	3.21584	1.05
Vulcain	3.51281	1.025
RS-25	3.90374	1.025

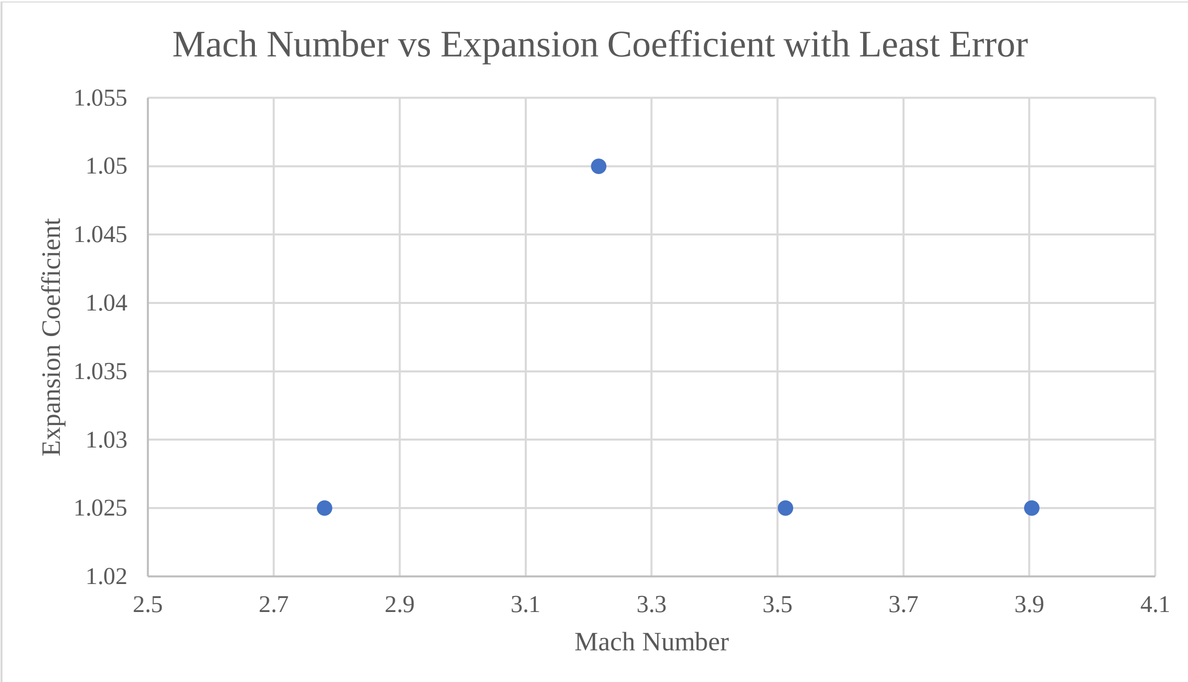

Figure 5.34 – Mach number vs expansion coefficient matching theoretical results.

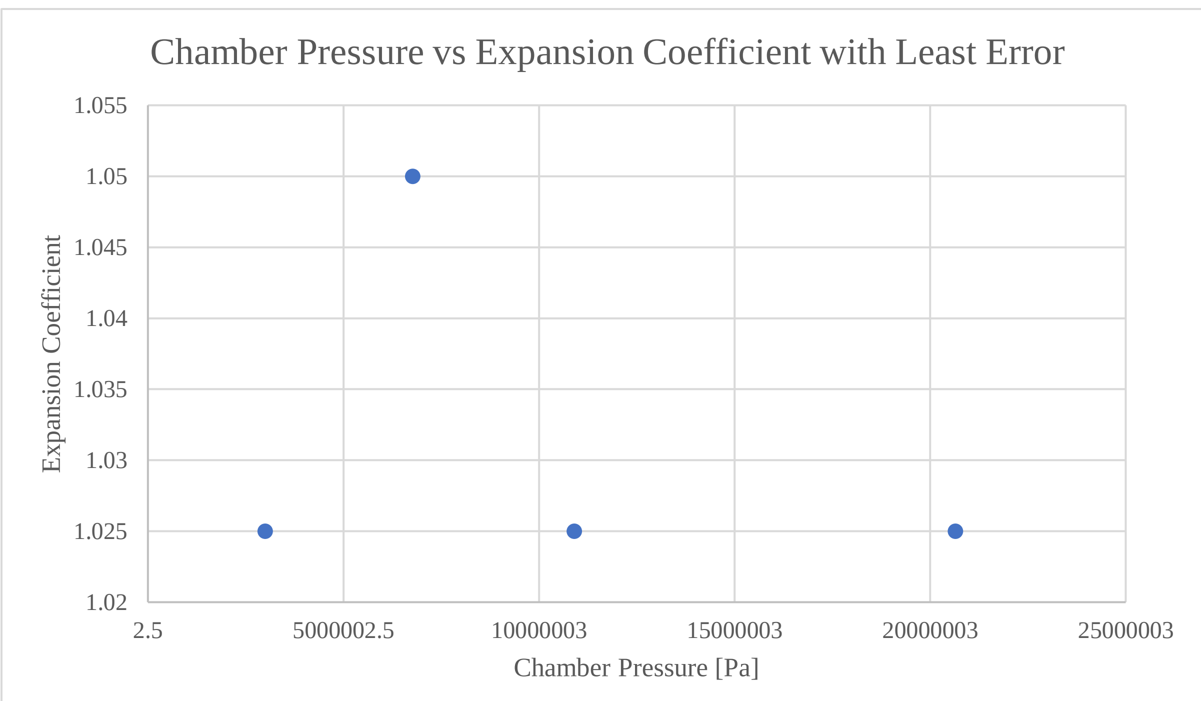

Figure 5.35 – Chamber pressure vs expansion coefficient matching theoretical results.

5.7 Conclusion

The aim of this chapter was to determine if any additional input parameters may affect the expansion coefficient's impact. Chamber pressure, chamber temperature, varying mixture ratios, and many other parameters seemed to have little to no effect. When using the method of characteristics to develop a nozzle contour, it appeared in each case to underperform and produce thrust values significantly less than predicted by theory. This theory has underlying assumptions about the fluid flow, namely related to viscous effects or in this case, the lack of. Inviscid assumptions entail a difference between reality and theory and thus an unknown that numerical methods can only attempt to estimate a solution for. This provides an opportunity to uncover some, if any, relationship for this difference.

The difficulty to effectively capture viscous effects in the governing equations ultimately leads to the requirement of a correction factor. This study performed a parametric evaluation to determine methods to account for viscous effects in the results from method of characteristics. Assuming inviscid flow, the nozzle contour from the method of characteristics on its own generated less force than theoretical results had quantified in experimental CFD studies.

By modifying this contour with expansion coefficients, the experimental results may shift either further away from or closer to theoretical calculations. These expansion coefficients can then serve as a correction factor to account for the viscous effects that the governing equations do not consider. Through the findings outlined in this chapter, this report concludes that the expansion coefficient to produce CFD results with the least difference from theoretical calculations is 1.025. Regardless of chamber settings, desired exit Mach number, or mixture ratios multiplying all of the nozzle contour vertical wall coordinates produced by the method of characteristics with this expansion coefficient yielded experimental results closest to theoretical calculations.

Chapter 6 Closing Discussions

6.1 Conclusion

The static geometry and chamber settings of most rocket nozzles ultimately entails a constant exit pressure. The generated thrust of the nozzle is dependent on many factors, but the exit pressure is one of them. The governing equations for the rocket thrust equation indicate that to maximize thrust, the exit pressure should equal the surrounding ambient pressure. Then to maximize the generated thrust, one can look at the controlling variables for the exit pressure. In this study, this report monitored the exit area's effect on exit pressure and thus the total thrust produced to optimize the nozzle's performance.

This report used Apollo 10's F-1 engine in the Saturn V launch to determine the effect of ideal conditions throughout the ascent. Because of the normally constant geometry, the nozzle contour's exit pressure typically matches the ambient pressure at a certain altitude. This works well to maximize the thrust at a given altitude but results in an underperforming engine at all other altitudes. Using the F-1 engine as a case study, this report assumed ideal conditions for the entirety of the ascent and compared the results with calculations for normal conditions. The metrics used to study the nozzle demonstrated a significant increase in performance in terms of the generated thrust. This increase in performance indicates the benefits of implementing such a system based on theory alone. To take it a step further, one may look to produce experimental studies via computational fluid dynamics to validate theoretical calculations.

For the nozzle geometry generation, the method of characteristics offers a numerical algorithm to produce a contour suited for specified flow conditions. This report generated nozzle contours at different altitudes of the Apollo 10 ascent for points of comparison between theory and experiment. The method of characteristics produced a contour set to develop the flow such that it met the Mach number under ideal conditions. CFD results uncovered an underperforming nozzle, leading to a parametric study which expanded and contracted the vertical coordinates by an expansion coefficient. In nearly all cases, the parametric study demonstrated that an expansion coefficient of 1.025 produced a nozzle contour that experimentally generated the same thrust as theoretical predictions.

An additional parametric study performed a similar evaluation for the method of characteristics using multiple other rocket engines. Each with its own chamber settings and specifications, theoretical application provided the idealized conditions which were used to produce the nozzle contour for CFD application. This parametric study also demonstrated that an expansion coefficient of 1.025 served as an effective correction factor for the method of characteristics to match theoretical calculations. This relationship between the method of characteristics and experimental findings appeared unrelated to the Mach number and chamber settings for all of the engines studied.

Based on the evaluation and parametric studies performed, this paper concludes that integrating a constantly adapted nozzle to maximize rocket engine performance offers beneficial results. To implement such a system using the method of characteristics, one may utilize a correction factor of 1.025 for geometry produced.

6.2 Future Work

The future work for this evaluation lies primarily in the limitations. The experimental findings came from numerical schemes and estimations, not actual hardware development which produced observed phenomena. The CFD-based estimations offered good insight into what reality *may* look like, but certainly not a guarantee. Applying the findings of this report to the real world will provide paramount understanding of what to expect from the expansion coefficients uncovered – the only problem being time and cost, as is true with many things. In lieu of actual hardware development and integration, computational simulations provided a cheaper alternative.

The larger the dataset, the closer one may reach the truth. Performing additional simulation work may offer expansion coefficients with smaller margins of error from theory or perhaps show a dependency for the coefficients not uncovered in this paper. This report did not find a dependency for the corrective expansion coefficient on either the Mach number or chamber pressure settings but that is not to say it does not exist.

Future work encompasses a greater extent of parameters in the parametric studies for the method of characteristics and an eventual application. With the application of this method, one may collect real-world data to compare theory, simulation, and observed phenomena.

References

[1] Mattingly, J. D., “Elements of Propulsion: Gas Turbines and Rockets,” American Institute of Aeronautics and Astronautics, Blacksburg, 2006.

[2] Anderson, J. D., “Modern Compressible Flow With Historical Perspective,” McGraw-Hill Education, New York, 2021.

[3] “Aerospaceweb.Org | Ask Us - Nozzle Overexpansion & Underexpansion.” Retrieved 21 June 2023. https://aerospaceweb.org/question/propulsion/q0220.shtml

[4] Ruf, J. H., and Jones, D., “George C. Marshall Space Flight Center Research and Technology Report 2014,” January 2015. https://doi.org/10.2514/6.2014-3956

[5] Van Nguyen, T., Hagemann, G., Immich, H., and Dumnov, G. E., “Advanced Rocket Nozzles,” *Journal of Propulsion and Power*, Vol. 14, No. 5, 1998, pp. 620–633. https://www.researchgate.net/publication/224796963

[6] Michel, U., “The Benefits of Variable Area Fan Nozzles on Turbofan Engines,” American Institute of Aeronautics and Astronautics (AIAA), Berlin, January 2011. https://doi.org/10.2514/6.2011-226

[7] Khare, S., and Saha, U. K., “Rocket Nozzles: 75 Years of Research and Development,” *Sadhana - Academy Proceedings in Engineering Sciences*, Vol. 46, No. 2, 2021, pp. 1–22. https://doi.org/10.1007/S12046-021-01584-6/FIGURES/22

[8] Horn, M., and Fisher, S., “Dual-Bell Altitude Compensating Nozzles,” 1994.

[9] Génin, C., Schneider, D., and Ralf, S., “Future Space-Transport-System Components under High Thermal and Mechanical Loads,” Garching, 2020.

[10] Wang, C.-H., Liu, Y., and Qin, L.-Z., “Aerospike Nozzle Contour Design and Its Performance Validation,” *Acta Astronautica*, Vol. 64, 2009, pp. 1264–1275. https://doi.org/10.1016/j.actaastro.2008.01.045

[11] Taylor, N., Steelant, J., and Bond, R., “Experimental Comparison of Dual Bell and Expansion Deflection Nozzles,” 2011. https://doi.org/10.2514/6.2011-5688

[12] Wang, Y., Lin, Y., Eri, Q., and Kong, B., “Flow and Thrust Characteristics of an Expansion–Deflection Dual-Bell Nozzle,” *Aerospace Science and Technology*, Vol. 123, No. 5, 2022. https://doi.org/10.1016/J.AST.2022.107464

[13] Jraisheh, A., Chutia, J., Benidar, A., and Kulkarni, V., “Altitude Compensating Ringed Nozzle,” *Acta Astronautica*, Vol. 210, 2023, pp. 45–55. https://doi.org/10.1016/J.ACTAASTRO.2023.05.003

[14] Fallon, B., “Variable-Throat Rocket Nozzle,” University of Nevada, Las Vegas, 2019. Retrieved 21 June 2023. https://brandonfallon.com/variable-throat-rocket-nozzle/

[15] Kumar Modak, P., Sharma Marhatta, A., Raj Jaiswal, H., Wangchuk, L., Yadav, A., and Singh Chand, D., "Designing and Performance Optimization of Dual Bell Nozzle," EasyChair Preprint, Bramhall, June 2023.

[16] Natta, P., Ranjith Kumar, V., and Hanumantha Rao, Y. V., "Flow Analysis of Rocket Nozzle Using Computational Fluid Dynamics (Cfd)," *International Journal of Engineering Research and Applications (IJERA)*, Vol. 2, No. 5, 2012, pp. 1226–1235. www.ijera.com

[17] Nagarajan, V., "Numerical Simulation of Entrainment and Recirculating Flow at the Base of a Truncated Aerospike Nozzle with Supplementary Base Flow," Master of Science Thesis. Arizona State University, 2017.

[18] Rao, G. V. R., "Handbook of Astronautical Engineering," McGraw-Hill Book Company, New York, 1961.

[19] Rao, G. V. R., "Recent Developments in Rocket Nozzle Configurations," *American Rocket Society*, Vol. 31, No. 11, 2012, pp. 1488–1494. https://doi.org/10.2514/8.5837

[20] Singh, A., and Shukla, N., "Rocket Engine Nozzle Optimization," *International Journal of Innovative Research in Science Engineering and Technology*, Vol. 9, No. 2, 2020, pp. 13634–13649. https://doi.org/10.15680/IJIRSET.2020.0902041

[21] Mishra, N. K., Prasad, S., and Padania, A., "Modeling and Simulation of Rocket Nozzle," *International Journal of Advanced Engineering and Global Technology*, Vol. 2, No. 09, 2014, pp. 988–995. www.ijaegt.com

[22] Samantra, A. K., Santhosh, K. S., Rashid, K., and Jayashree, A., "Study of Expansion Ratio on Dual Bell Nozzle of LOX-RP1 Engine for Replacing the Existing Bell Nozzle to Dual Bell Nozzle," *IOP Conference Series: Materials Science and Engineering*, Vol. 912, No. 4, 2020. https://doi.org/10.1088/1757-899X/912/4/042039

[23] "F-1 Engine Fact Sheet," Saturn V News Reference, 2005. Retrieved 21 June 2023. https://web.archive.org/web/20051221114403/http://history.msfc.nasa.gov/saturn_apollo/documents/F-1_Engine.pdf

[24] NASA, "J-2 Engine Fact Sheet," *Saturn V News Reference*, 1968, pp. 6.1-6.7. Retrieved 28 June 2023

[25] "Saturn V Flight Manual, SA 504," National Aeronautics and Space Administration, 1968. Retrieved 21 June 2023

[26] "Atmospheric Pressure vs. Elevation above Sea Level," 2003. Retrieved 22 June 2023. https://www.engineeringtoolbox.com/air-altitude-pressure-d_462.html

[27] Krausse, S. C., "Apollo/Saturn V Postflight Trajectory AS-505," July 1969.

[28] "Vulcain Rocket Engine - Thrust Chamber," EADS Astrium, 2012. Retrieved 21 November 2023.

https://web.archive.org/web/20120225051943/http://cs.astrium.eads.net/sp/launcher-propulsion/rocket-engines/vulcain-rocket-engine.html

[29] "RS-25 Engine | Aerojet Rocketdyne," Aerojet Rocketdyne, 2014. Retrieved 21 November 2023. https://web.archive.org/web/20140703043723/https://www.rocket.com/rs-25-engine

[30] Wade, M., "J-2." Retrieved 21 November 2023. https://web.archive.org/web/20160719175425/http://www.astronautix.com/j/j-2.html

[31] Dinardi, A., Capozzoli, P., and Shotwell, G., "LOW-COST LAUNCH OPPORTUNITIES PROVIDED BY THE FALCON FAMILY OF LAUNCH VEHICLES," Taipei, 2008.

[32] Gordon, S., and McBride, B. J., "Computer Program for Calculation of Complex Chemical Equilibrium Compositions and Applications,."

Appendix A MATLAB Script for Saturn V Case Study and Ideal Condition Analysis

Problem Set Up

load and prepare data

```
clc; clear all
T = readtable('SaturnV_ascent.csv');
time = table2array(T(:,1)); %ascent time [s]
altitude = table2array(T(:,2)); %ascent altitude [m]

s_ic = 65617; %S-IC ends, S-II begins at 162s
s_ii = 187430; %S-II ends, S-IVB begings at 553 s

launch_data = zeros(length(time), 7);
results_nonIdeal = zeros(length(time), 7);
results_Ideal = zeros(length(time), 7);

launch_data(:,1) = time;
launch_data(:,2) = altitude;

% ambient pressure at altitude [Pa]
for i = 1:length(altitude)

    if altitude(i) < 44330
        launch_data(i,3) = 101325*(1-2.25577*10^-5*launch_data(i,2))^5.25588;
    else
        launch_data(i,3) = 0;
    end

end
```

```
Warning: Column headers from the file were modified to make them valid MATLAB
identifiers before creating variable names for the table. The original column
headers are saved in the VariableDescriptions property.
Set 'VariableNamingRule' to 'preserve' to use the original column headers as
table variable names.
```

F-1 Specifications

```
F1_gamma = 1.1503;
F1_area_Ratio = 16;
F1_area_Exit = 0.25*pi*(3.5306)^2; %[m^2]
F1_radius_Exit = sqrt(F1_area_Exit/3.14); %[m]
F1_area_Throat = F1_area_Exit/F1_area_Ratio; %[m^2]
F1_radius_Throat = sqrt(F1_area_Throat/3.14); %[m]
F1_MixtureRatio = 2.27;
F1_pc = 6.653*10^6;    %[Pa]
```

```
F1_pe = 52535;  %       %[Pa]
F1_Tc = 3572;          %[K]

F1_Mw_O = 32;
F1_Mw_RP1 = 175;
F1_Mw = molecularWeight(F1_MixtureRatio, F1_Mw_O, F1_Mw_RP1);

F1_G = V_func(F1_gamma);
```

J-2 Specifications

```
J2_gamma = 1.1455;
J2_area_Ratio = 27.5;
J2_area_Exit = 0.25*pi*(1.9558)^2; %[m^2]
J2_area_Throat = J2_area_Exit/J2_area_Ratio; %[m^2]
J2_MixtureRatio = 5.5;
J2_pc = 5.261*10^6;    %[Pa]
J2_pe = 21570; %      %[Pa]
J2_Tc = 3450;          %[K]

J2_Mw_O = 32;
J2_Mw_LH2 = 2.016;
J2_Mw = molecularWeight(J2_MixtureRatio, J2_Mw_O, J2_Mw_LH2);

J2_G = V_func(J2_gamma);
```

Calculations

```
clear i;

for i = 1:length(launch_data)


    pa = launch_data(i, 3);
    current_alt = launch_data(i, 2);


    if current_alt < s_ic %% 5x F-1 Active

        F1_ve = ve_func(F1_gamma,F1_Mw, F1_Tc, F1_pe, F1_pc);
        results_nonIdeal(i, 1) = F1_ve;

        F1_mdot = mdot_func(F1_pc, F1_area_Throat, F1_G, F1_Tc, F1_Mw);
        results_nonIdeal(i, 5) = F1_mdot;
        results_Ideal(i, 5) = F1_mdot;

        F1_Ft = Ft_func(F1_mdot, F1_ve, F1_pe, pa, F1_area_Exit);
        results_nonIdeal(i, 2) = F1_Ft;
```

```
    F1_Cf = Cf_func(F1_Ft, F1_pc, F1_area_Exit);
    results_nonIdeal(i, 3) = F1_Cf;

    F1_Isp = Isp_func(F1_Ft, F1_mdot);
    results_nonIdeal(i,4) = F1_Isp;

    F1_Me = M_isentropic(F1_pc, F1_pe, F1_gamma);
    results_nonIdeal(i, 7) = F1_Me;

    F1_AE_ideal = Ae_IDEAL_func(F1_G, pa, F1_pc, F1_gamma, F1_area_Throat);
    results_Ideal(i,6) = F1_AE_ideal;

    F1_ve_ideal = ve_func(F1_gamma,F1_Mw, F1_Tc, pa, F1_pc);
    results_Ideal(i,1) = F1_ve_ideal;

    F1_Ft_ideal = F1_ve_ideal*F1_mdot;
    results_Ideal(i,2) = F1_Ft_ideal;

    F1_Cf_ideal = Cf_func(F1_Ft_ideal, F1_pc, F1_area_Throat);
    results_Ideal(i,3) = F1_Cf_ideal;

    F1_Isp_ideal = Isp_func(F1_Ft_ideal, F1_mdot);
    results_Ideal(i,4) = F1_Isp_ideal;

    F1_Me = M_isentropic(F1_pc, pa, F1_gamma);
    results_Ideal(i, 7) = F1_Me;

elseif current_alt < s_ii %% 5x J-2 Active


    J2_ve = ve_func(J2_gamma,J2_Mw, J2_Tc, J2_pe, J2_pc);
    results_nonIdeal(i, 1) = J2_ve;

    J2_mdot = mdot_func(J2_pc, J2_area_Throat, J2_G, J2_Tc, J2_Mw);
    results_nonIdeal(i, 5) = J2_mdot;
    results_Ideal(i, 5) = J2_mdot;

    J2_Ft = Ft_func(J2_mdot, J2_ve, J2_pe, pa, J2_area_Exit);
    results_nonIdeal(i, 2) = J2_Ft;

    J2_Cf = Cf_func(J2_Ft, J2_pc, J2_area_Exit);
    results_nonIdeal(i, 3) = J2_Cf;

    J2_Isp = Isp_func(J2_Ft, J2_mdot);
    results_nonIdeal(i,4) = J2_Isp;

    J2_AE_ideal = Ae_IDEAL_func(J2_G, pa, J2_pc, J2_gamma, J2_area_Throat);
    results_Ideal(i,6) = J2_AE_ideal;

    J2_ve_ideal = ve_func(J2_gamma,J2_Mw, J2_Tc, pa, J2_pc);
    results_Ideal(i,1) = J2_ve_ideal;

    J2_Ft_ideal = J2_ve_ideal*J2_mdot;
```

```
        results_Ideal(i,2) = J2_Ft_ideal;

        J2_Cf_ideal = Cf_func(J2_Ft_ideal, J2_pc, J2_area_Throat);
        results_Ideal(i,3) = J2_Cf_ideal;

        J2_Isp_ideal = Isp_func(J2_Ft_ideal, J2_mdot);
        results_Ideal(i,4) = J2_Isp_ideal;

    else %% 1x J-2 Active

        J2_ve = ve_func(J2_gamma,J2_Mw, J2_Tc, J2_pe, J2_pc);
        results_nonIdeal(i, 1) = J2_ve;

        J2_mdot = mdot_func(J2_pc, J2_area_Throat, J2_G, J2_Tc, J2_Mw);
        results_nonIdeal(i, 5) = J2_mdot;
        results_Ideal(i, 5) = J2_mdot;

        J2_Ft = Ft_func(J2_mdot, J2_ve, J2_pe, pa, J2_area_Exit);
        results_nonIdeal(i, 2) = J2_Ft;

        J2_Cf = Cf_func(J2_Ft, J2_pc, J2_area_Exit);
        results_nonIdeal(i, 3) = J2_Cf;

        J2_Isp = Isp_func(J2_Ft, J2_mdot);
        results_nonIdeal(i,4) = J2_Isp;

        J2_AE_ideal = Ae_IDEAL_func(J2_G, pa, J2_pc, J2_gamma, J2_area_Throat);
        results_Ideal(i,6) = J2_AE_ideal;

        J2_ve_ideal = ve_func(J2_gamma,J2_Mw, J2_Tc, pa, J2_pc);
        results_Ideal(i,1) = J2_ve_ideal;

        J2_Ft_ideal = J2_ve_ideal*J2_mdot;
        results_Ideal(i,2) = J2_Ft_ideal;

        J2_Cf_ideal = Cf_func(J2_Ft_ideal, J2_pc, J2_area_Throat);
        results_Ideal(i,3) = J2_Cf_ideal;

        J2_Isp_ideal = Isp_func(J2_Ft_ideal, J2_mdot);
        results_Ideal(i,4) = J2_Isp_ideal;

    end

end

t = launch_data(:,1);
graph_func(launch_data, results_nonIdeal, results_Ideal, "Non-Ideal", "Ideal");

filePath = "C:\Users\Kevin Aghassi Lelham\Desktop\295A\Excel\MATLAB Productions\";
launchName = "launchData.csv";
nonIdealName = "ascentNonIdeal1.csv";
idealName = "ascentIdeal1.csv";
saveLaunch = append(filePath, launchName);
```

```
saveNonIdeal = append(filePath, nonIdealName);
saveIdeal = append(filePath, idealName);

writematrix(launch_data, saveLaunch)
writematrix(results_nonIdeal, saveNonIdeal)
writematrix(results_Ideal, saveIdeal)

figure
plot(time, altitude, 'LineWidth', 2);
title('Saturn V Ascent - Altitude vs Time', 'FontSize', 20);
grid on
xlabel('Time [s]', 'FontSize', 14);
ylabel('Altutde [m]', 'FontSize', 14);
xlim([-15, 9000]);
set(gca,'FontName','Times')
```

Functions Used

```
function Ae = Ae_IDEAL_func(Gamma, pe, pc, gamma, Astar)

Ae = Astar*Gamma/sqrt((2*gamma*(gamma-1)^(-1)*(pe/pc)^(2/gamma)*(1-(pe/pc)^((gamma-1)/2))));

end

function Ft = Ft_func(mdot, ve, pe, pa, Ae)

Ft = mdot*ve + (pe-pa)*Ae;

end

function [M] = M_isentropic(p0, p, g)

LHS = p/p0;
tol = 0.0001;

Mg = 1.00001;
i = 0;

while i < 2000000 && Mg < 15

    RHS = (1+0.5*(g-1)*Mg^2)^(-g/(g-1));

    re = abs(LHS-RHS);

    if re < tol
        break
    end

    i = i+1;
    Mg = Mg + 0.00001;
```

```
end

M = Mg;

end


function Cf = Cf_func(Ft, pc, Astar)

Cf = Ft/(pc*Astar);

end

function graph_func(launch_data, results1, results2, type1, type2)

t = launch_data(:,1);
altitude = launch_data(:,2);

exit_v_1 = results1(:,1);
thrust_1 = results1(:,2);
Cf_1 = results1(:,3);
Isp_1 = results1(:,4);

exit_v_2 = results2(:,1);
thrust_2 = results2(:,2);
Cf_2 = results2(:,3);
Isp_2 = results2(:,4);

figure
subplot(2, 2, 1)
sgtitle("Saturn V Ascent Characteristics with Altitude", 'FontSize', 20);
plot(altitude, exit_v_1, 'LineWidth', 2);
hold on
grid on
plot(altitude, exit_v_2, 'LineWidth', 2);
legend(type1, type2, 'FontSize', 12);
xlabel('Altitude [m]', 'FontSize', 14);
ylabel('v_e [m/s]', 'FontSize', 14);
title('Exit Velocity vs Altitude', 'FontSize', 16);
set(gca,'FontName','Times')

subplot(2, 2, 2)
plot(altitude, Isp_1, 'LineWidth', 2);
hold on
grid on
plot(altitude, Isp_2, 'LineWidth', 2);
legend(type1, type2, 'FontSize', 12);
xlabel('Altitude [m]', 'FontSize', 14);
ylabel('I_{sp} [s]', 'FontSize', 14);
title('Specific Impulse vs Altitude', 'FontSize', 16);
set(gca,'FontName','Times')

subplot(2, 2, 3)
```

```
plot(altitude, thrust_1, 'LineWidth', 2);
hold on
grid on
plot(altitude, thrust_2, 'LineWidth', 2);
legend(type1, type2, 'FontSize', 12);
xlabel('Altitude [m]', 'FontSize', 14);
ylabel('F [N]', 'FontSize', 14);
title('Thrust vs Altitude', 'FontSize', 16);
set(gca,'FontName','Times')

subplot(2, 2, 4)
plot(altitude, Cf_1, 'LineWidth', 2);
grid on
hold on
plot(altitude, Cf_2, 'LineWidth', 2);
legend(type1, type2, 'FontSize', 12);
xlabel('Altitude [m]', 'FontSize', 14);
ylabel('C_F', 'FontSize', 14);
title('Coefficient of Thrust vs Altitude', 'FontSize', 16);
set(gca,'FontName','Times')

figure
sgtitle("Saturn V Ascent Characteristics with Time", 'FontSize', 20);
subplot(2, 2, 1)
plot(t, exit_v_1, 'LineWidth', 2);
hold on
grid on
plot(t, exit_v_2, 'LineWidth', 2);
legend(type1, type2, 'FontSize', 12);
xlabel('Time [s]', 'FontSize', 14);
ylabel('v_e [m/s]', 'FontSize', 14);
title('Exit Velocity vs Time', 'FontSize', 16);
xlim([t(1) t(end)])
set(gca,'FontName','Times')

subplot(2, 2, 2)
plot(t, Isp_1, 'LineWidth', 2);
hold on
grid on
plot(t, Isp_2, 'LineWidth', 2);
legend(type1, type2, 'FontSize', 12);
xlabel('Time [s]', 'FontSize', 14);
ylabel('I_{sp} [s]', 'FontSize', 14);
title('Specific Impulse vs Time', 'FontSize', 16);
xlim([t(1) t(end)])
set(gca,'FontName','Times')

subplot(2, 2, 3)
plot(t, thrust_1, 'LineWidth', 2);
hold on
grid on
plot(t, thrust_2, 'LineWidth', 2);
legend(type1, type2, 'FontSize', 12);
```

```
xlabel('Time [s]', 'FontSize', 14);
ylabel('F [N]', 'FontSize', 14);
title('Thrust vs Time', 'FontSize', 16);
xlim([t(1) t(end)])
set(gca,'FontName','Times')

subplot(2, 2, 4)
plot(t, Cf_1, 'LineWidth', 2);
hold on
grid on
plot(t, Cf_2, 'LineWidth', 2);
legend(type1, type2, 'FontSize', 12);
xlabel('Time [s]', 'FontSize', 14);
ylabel('C_F', 'FontSize', 14);
title('Coefficient of Thrust vs Time', 'FontSize', 16);
xlim([t(1) t(end)])
set(gca,'FontName','Times')

figure
plot(altitude, Isp_1, 'LineWidth', 2);
hold on
grid on
plot(altitude, Isp_2, 'LineWidth', 2);
legend(type1, type2, 'FontSize', 12);
xlabel('Altitude [m]', 'FontSize', 14);
ylabel('I_{sp} [s]', 'FontSize', 14);
title('Specific Impulse vs Altitude', 'FontSize', 16);
set(gca,'FontName','Times')
xlim([0 50000])

end

function Isp = Isp_func(Ft, mdot)

g0 = 9.81;

Isp = Ft/(g0*mdot);

end

function mdot = mdot_func(pc, Astar, Gamma, Tc, Mw)

Ra = 8314;
mdot = pc*Astar*Gamma/(sqrt(Ra*Tc/Mw));

end

function Mw = molecularWeight(mix_R, mass_O, mass_F)

Mw = (1*mass_F + mix_R * mass_O)/(1+mix_R);

end
```

```
function G = V_func(g)

    G = sqrt(g*((1+g)/2)^((1+g)/(1-g)));

end

function ve = ve_func(gamma, Mw, Tc, pe, pc)

Ra = 8314;
ve = sqrt(2*gamma*Ra*Tc*(gamma-1)^(-1)*Mw^(-1)*(1-(pe/pc)^((gamma-1)/gamma)));

end
```

Published with MATLAB® R2021a

Appendix B MATLAB Script for Method of Characteristics Algorithm

```
% Kevin Aghassi Lelham, M.S. Aerospace Engineering SJSU, AE295A SU23, Method of Characterstics
Main
```

Nozzle Parameters

```
clc; clear all
engine = "RL-10"; % update engine specs as needed
g = 1.2869;
Me = 2.89866;
nue = M2nuFunc(g, Me);
thetaMax = 180*nue/(pi*2);
rt = 0.07370839; % throat radius, m
```

Method of Characteristics Setup

```
n = 60;                  % total characteristic lines
p = n + n*(n+1)/2;      % total points
d_theta = 0.465;

b = "Y";

wArray = zeros(length(n), 1);         % points on the wall
cArray = zeros(length(n), 1);         % points on center line

T = string(zeros(p+1,0));
wArray(1) = 1+n;
cArray(1) = 1;
mArray = [];

T(wArray(1)) = "W";
T(cArray(1)) = "C";

for i=2:n

    wArray(i) = wArray(i-1)+1+n-(i-1);
    cArray(i) = wArray(i-1) + 1;

    T(cArray(i)) = "C";
    T(wArray(i)) = "W";

end

clear i;
f = 1;
```

```
for i = 1:p

    if ismissing(T(i))
        T(i) = "M";
        mArray(f, 1) = i;
        f = f+1;
    end

end
clear i, clear f;

wArray = [1, wArray];
T = ["W", T]';

theta = zeros(p+1, 1);
nu = zeros(p+1, 1);
M = zeros(p+1, 1);
mu = zeros(p+1, 1);
Kn = zeros(p+1, 1);
Kp = zeros(p+1, 1);

X = zeros(p+1, 1);
Y = zeros(p+1, 1);
```

Implement M.o.C. Algorithm

```
nu(1) = 0;
theta(1) = thetaMax;
M(1) = nu2MFunc(g, nu(1), "Degrees");
mu(1) = 180*muFunc(M(1))/pi;
Kn(1) = theta(1) - nu(1);
Kp(1) = theta(1) + nu(1);
X(1) = 0;
Y(1) = rt;

j = 1;
for i = 2:p+1

    if T(i) == "C" % Center line points

        if i == 2

            nu(2) = 0.375;
            theta(2) = 0.375;
            Kn(i) = theta(i) + nu(i);
            Kp(i) = theta(i) - nu(i);

            if b == "Y"

                X(i) = -rt/tand(270+d_theta);
```

```
                Y(i) = 0;

            end

        else

            Kn(i) = Kn(cArray(j)+2);
            Kp(i) = -Kn(i);
            theta(i) = 0;
            nu(i) = 0.5*(Kn(i) - Kp(i));

            j = j+1;

            if b == "Y"

                X(i) = -Y(cArray(j-1)+2)/tand(mu(cArray(j-1)+2) + theta(cArray(j-1)+2)) +
X(cArray(j-1)+2);
                Y(i) = 0;

            end

        end

        M(i) = nu2MFunc(g, nu(i), "Degrees");
        mu(i) = 180*muFunc(M(i))/pi;

    elseif T(i) == "M" % Middle points

        if j < 2

            theta(i) = theta(2) + (i-2)*d_theta;
            nu(i) = theta(i);

            Kn(i) = theta(i) + nu(i);
            Kp(i) = theta(i) - nu(i);

               if b == "Y"

                [X(i), Y(i)] = eqSolver_Func(tand(theta(i-1) + mu(i-1)), tand(270 + d_theta*(i-
1)), X(i-1), X(1), Y(i-1), Y(1));

            end

        else

            Kn(i) = Kn(i-(n-j+2));
            Kp(i) = Kp(cArray(j)+1);


            theta(i) = 0.5*(Kn(i) + Kp(i));
            nu(i) = 0.5*(Kn(i) - Kp(i));

            if b == "Y"
```

```
                [X(i), Y(i)] = eqSolver_Func(tand(theta(i-1) + mu(i-1)), tand(theta(i-n+j-2) -
mu(i-n+j-2)), X(i-1), X(i-n+j-2), Y(i-1), Y(i-n+j-2));

            end

        end

        M(i) = nu2MFunc(g, nu(i), "Degrees");
        mu(i) = 180*muFunc(M(i))/pi;

    else  % Wall points

        theta(i) = theta(i-1);
        nu(i) = nu(i-1);
        M(i) = M(i-1);
        mu(i) = mu(i-1);
        Kn(i) = theta(i) + nu(i);
        Kp(i) = theta(i) - nu(i);

        if b == "Y"

            if j < 2

                [X(i), Y(i)] = eqSolver_Func(tand(theta(i-1) + mu(i-1)), tand(theta(1)), X(i-1),
X(1), Y(i-1), Y(1));

            else

                [X(i), Y(i)] = eqSolver_Func(tand(theta(i-1) + mu(i-1)),
tand(theta(wArray(j)+1)), X(i-1), X(wArray(j)+1), Y(i-1), Y(wArray(j)+1));

            end

        end

    end

end
clear i, clear j;
```

Condense Data

```
theta(end) = 0;
nu(end) = M2nuFunc(g, Me);
M(end) = Me;
mu(end) = 180*muFunc(M(end))/pi;

R = [Kn, Kp, theta, nu, M, mu];
if b == "Y"
    f = 1;
```

```
    xCord = zeros(n+1, 1);
    yCord = zeros(n+1, 1);
    zCord = zeros(n+1, 1);
    for i = 1:p+1

        if T(i) == "W"
            xCord(f) = X(i);
            yCord(f) = Y(i);
            zCord(f) = 0;
            f = f+1;
        end

    end
    clear i, clear f;
end


figure
plot(xCord, yCord)
title("Nozzle Contour")
xlabel("X Coords [m]")
ylabel("Y Coords [m]")
grid on
```

Save to Text

```
filePath = "C:\Users\Kevin Aghassi Lelham\Desktop\295A\Excel\MATLAB Productions\";
fileName = "cordTable_" + engine + "_" + Me + ".csv";
saveName = append(filePath, fileName);
if b == "Y"
    xCord = sort(xCord);
    yCord = sort(yCord);
    writematrix([xCord, yCord, zCord],saveName);
end
```

Functions Used

```
function [X, Y] = eqSolver_Func(m1, m2, x1, x2, y1, y2)

syms x y z

eqn1 = y - m1*(x-x1) == y1;
eqn2 = y - m2*(x-x2) == y2;

sol = solve([eqn1, eqn2], [x, y]);

X = sol.x;
```

```
Y = sol.y;

end

function [nu] = M2nuFunc(g, M)

A = sqrt((g+1)/(g-1));
B = atan(sqrt(((g-1)/(g+1))*(M^2-1)));
C = atan(sqrt((M^2-1)));

nu = A*B-C;

end

function [mu] = muFunc(M)

mu = asin(1/M);

end

function [M] = nu2MFunc(g, nu_True, DoR)

i = 0;
if DoR == "Degrees"
    nu_True = nu_True * pi/180;
end

M_Guess = 1.000;
tol = 0.0001;

    while M_Guess < 15 && i < 200000

        nu_Guess = M2nuFunc(g, M_Guess);

        re = abs(nu_True - nu_Guess);

        if re < tol
            break
        end

        M_Guess = M_Guess+0.0001;

        i = 1+i;
    end
    M = M_Guess;
end
```

Published with MATLAB® R2021a